ALIGNMENT EFFECTS IN ELECTRON CAPTURE FROM D_2^+ MOLECULAR IONS BY DOUBLY CHARGED PROJECTILES

by

INGRID REISER

Diplom, Universität Kaiserslautern, 1995

A DISSERTATION

submitted in partial fulfillment of the

requirements for the degree

DOCTOR OF PHILOSOPHY

Department of Physics

College of Arts and Sciences

KANSAS STATE UNIVERSITY

Manhattan, Kansas

2002

Approved by:

Major Professor

C. L. Cocke

ABSTRACT

An ion - molecule collision experiment resembles a double-slit experiment on an atomic scale. In Young's double-slit experiment, light is sent through two narrow slits, separated by some distance, and interference fringes are observed on a screen behind. Varying the separation between the slits changes the interference pattern. A molecular target is similar. The two atomic centers correspond to the double slits. The vector separation of the slit is varied by rotating the molecule. In the work presented here, we are looking for alignment effects when a doubly charged projectile captures a single electron from a molecular (D_2^+) ion. The advantage of using a true one-electron target is that single electron capture is unambigous. No two-electron transition is required, which would be the case if one used molecular hydrogen with two binding electrons.

The experiment is done in the following way: Two ion beams intersect each other at 90°. The alignment of the molecular ion is determined after the collision, when the electron has been captured by the projectile. Left without bond, the molecular fragments recoil along the internuclear axis of the destroyed molecule. Measuring the fragments' relative velocity after the collision thus reveals the direction of the internuclear axis at the time of the collision. The three-dimensional velocity vector of each fragment is obtained through measuring the particle's position in two dimensions. The particle's flight time gives the third dimension. This is done for each fragment using a multi-hit detector which can detect two fragments that impact almost simultaneously. The results show a strong dependence of the capture probability on the alignment of the internuclear axis of the molecule with respect to the ion beam. Electron capture is favored when the molecular ion is aligned perpendicular to the projectile beam direction. The experimental results show the same trend as theoretical predictions for the alignment effect, which are obtained from a model calculation for charge transfer in ion-molecule collisions. The model includes interference from the two atomic centers of the molecular ion through a phase factor similar to the one used in optics. Not all of the features predicted by theory are observed in the experiment.

ACKNOWLEDGEMENTS

I am grateful to my advisor, Prof. Lew Cocke, for his piloting me through the reefs and depths I encountered while working on this project. His sharp physical mind is simply amazing and makes him a true role model for us physics students.

I wish to thank the director of the J. R. MacDonald Laboratory, Prof. Patrick Richard, for giving me the opportunity to carry out research in his laboratory. Thanks to the chairperson of my PhD committee, Prof. S. Starrett, and to the committee members, Prof. V. Ortiz, Prof. I. Ben-Itzhak and Prof. C. D. Lin for their interest and involvement in my work. In particular I enjoyed the discussions I've had with CD, learning about his collision model and other aspects of collision theory.

The Gießen ion-ion group lead by Prof. E. Salzborn has been of tremendous help. Thanks to Frank Melchert for the many discussions and his freundliche und offene Aufnahme into the ion-ion community. Thanks to Harald Bräuning for inviting me to participate in the total cross section measurements, and for his kick-starting of the KSU experiment by helping me find the first coincidence peak.

This work would not have been possible without the help of the technical staff of the JRM, in particular Paul Gibson, Charles Fehrenbach, and Bob Geering in the workshop. The technical advice of Martin Stockli in the initial phase is acknowledged.

Imad Ali was a great help with the delay-line detector. Chris Verzani and Dag Hathiramani were helpful by giving a hand whenever needed. Special thanks to Kevin Carnes, the most user-friendly VAX sysadmin ever, answering the dumbest computer questions with everlasting patience - thanks also to Vince Needham, for his help in overcoming the numerous Win/PC hurdles.

The foundations to this work were laid by Chun-Yen Chen, from who I inherited the apparatus and who taught me the basics of an ion-ion collision experiment. I want to thank her for the many helpful discussions we've had, and for her constant support and encouragement during all stages of the project.

Last but not least this work would not have succeeded without the constant support and backing by Emil Sidky, and the most welcome, stress relieving distractions by our Sohn Nikolaj.

TABLE OF CONTENTS

List of Figures **iv**

List of Tables **x**

1 Introduction **1**

1.1 Motivation 1

1.2 Survey: Alignment Effects in Capture and Ionization from Diatomic Molecules 3

1.2.1 Alignment Dependence in the Theoretical Models 3

1.2.2 Alignment Dependence Observed in Collision Experiments . . 5

1.3 Outline of this work 9

1.4 Reactions 9

1.5 Coordinate Frames 11

1.5.1 Laboratory and Center-of-Mass Frames 11

1.5.2 Molecular Frame 13

1.5.3 Laboratory Energies and Scattering Angles of the Molecular Fragments 14

1.5.4 Laboratory Frame and Laboratory Overview 16

1.6 Properties of the H_2^+ Molecular Ion 18

2 Theoretical Model **21**

2.1 The D_2^+ Molecular Wave function in the LCAO Approximation 21

2.2 Theoretical Model: Electron Capture in Collisions between Ions and Molecules 24

2.3 Model Calculation Results; Comparison to Experiment for Total Cross Sections 28

2.3.1 Model Predictions for the Molecular Alignment Dependence . 33

3 Experimental Approach **37**

3.1 Apparatus 37

3.1.1 Projectile Beam 39

3.1.2 Target Beam 40

3.1.3 Interaction Region 41

3.1.4 Beam Cleaner 43

3.2 Particle Detection 48
3.2.1 Multi-Hit Detector 49
3.2.2 Beam Viewer 52
3.3 Electronics Scheme and Data Acquisition 54
3.3.1 Coincidence Scheme 54
3.3.2 Data Acquisition 56
3.3.3 Second Hit Resorting Algorithm 56
3.4 Event Rates 58
3.4.1 Ion-Ion Collisions 59
3.4.2 Rest Gas Collisions 60
3.4.3 Coincidence Rates 62

4 Ion Trajectory Simulations 66
4.1 Fragment Imaging 66
4.2 Imaging of a Coulomb-sphere through Magnetic and Electric Analyzers 68

5 Data Analysis 70
5.1 Introduction 70
5.2 Background Subtraction 71
5.2.1 The Raw Position and Time-of-Flight Spectra 73
5.3 The Coulomb-Sphere in the Detector Frame 75
5.4 Mapping Properties and Lens Distortions 80
5.4.1 Deflector Offset 81
5.5 Calibration Factors 83
5.5.1 Time Calibration 83
5.5.2 Position Calibration 84
5.6 Reconstruction Scheme 85
5.6.1 Axis Corrections 85
5.6.2 Image Distortions 87
5.6.3 Calibration into Momentum 88
5.6.4 Summary of the Algorithm 88
5.6.5 Quality of the Reconstruction Algorithm 89
5.7 Transformation into CM Coordinates 91
5.8 Energy distribution of the Fragments 92

6 Results and Discussion 94
6.1 The Raw Coulomb-spheres 94
6.2 The Corrected Coulomb-sphere in the Laboratory Frame 97
6.3 The Angular Distributions 98

6.4 A Note on Total Cross Sections 103

7 Conclusion **105**

Bibliography **107**

A Total Cross Section Measurement **113**

B Two Dimensional Linear Least Squares Fitting **119**

C Position maps **121**

D Distortions of a Coulomb-sphere by Magnetic and Electric Fields **129**

D.1 Magnetic Analyzer 130

D.2 Electrostatic Analyzer 135

E Data Analysis Software **138**

LIST OF FIGURES

1.1 Differential cross section for electron capture in 1MeV p^+-H_2 collisions. The molecular axis is at a fixed angle, here perpendicular to the projectile beam. From N.C. Deb et al, Phys. Rev. A **38**, 3769 (1988) . . 4

1.2 Electron capture cross section as a function of angle between the projectile velocity and molecular axis in 16 MeV O^{8+}-D_2 collisions. Symbols: Experimental data, solid line: interference model prediction. The dotted line is a $1+c_1\cos(c_2\cos\theta)$ fit to the data. S. Cheng et al, Phys. Rev. A **47**, 3923 (1993) 6

1.3 Alignment dependence for multiionization of N_2 by 200 keV He^+ ions. The histograms are experimental data, the dotted line is the $\sin(\theta)$ distribution. The dashed lines are the results of a theoretical calculation [26]. From U. Werner et al, Phys. Rev. Lett. **79**, 1662 (1997) 7

1.4 Experimental-to-theoretical cross section ratios for electron emission in 60 MeV/u Kr^{34+} colliding with H_2 at electron emission angles of 20° and 30°. The dashed lines show a ratio of 1. The oscillatory structure is due to coherent electron emission from the two atomic centers of the H_2 molecule. From N. Stolterfoht et al, Phys. Rev. Lett. **87**, 23201 (2001) 8

1.5 The velocity diagram of the ion - molecular ion collision, after the molecular ion breaks up. The diagram is not to scale. The alignment angle θ is the angle between relative velocity v_{rel} and internuclear axis of the molecular ion. 12

1.6 The molecular frame. The velocity of the molecular ion's center-of-mass travels at the molecular ion beam velocity $\mathbf{v}_{beam}$, the molecular fragment's velocity with respect to the center-of-mass is $\mathbf{v}_{CS}$. $\mathbf{v}_1$ and $\mathbf{v}_2$ are laboratory velocities. 14

1.7 Laboratory energy and laboratory scattering angle of one fragment emerging from a Coulomb explosion of a molecular ion, as a function of the angle between molecular axis and molecular ion beam direction. The beam energy is 3.1 keV, the Coulomb-energy is 6 eV per fragment. 15

1.8 The laboratory coordinate system. The molecular ion beam travels along the z^{lab}-axis and the projectile beam travels along the x^{lab} - axis. The detector surface normal is at 15° horizontal, 20° vertical to the z^{lab}-axis. 16
1.9 Potential curves of the ground states of H_2 and H_2^{2+}, as well as the three lowest H_2^+ states. From [28]. 18
1.10 Energy distribution of ionized H^+-H^+ and D^+-D^+ molecular fragments calculated by M.H. Prior [31], as described in the text. 20

2.1 The deuterium molecular ion. 21
2.2 Effective charge $Z^\star$ and ground state energy E_{1s} of the $D_2^+(1s\sigma g)$ state as a function of internuclear separation R calculated from the LCAO model with variable $Z^\star$. Bottom graph: Solid line: result from LCAO with constant Z=1. Dashed line: result from variable $Z^\star$ LCAO. Dash-dotted line: exact calculation. From [33]. 23
2.3 Geometry for an ion-molecule collision. 24
2.4 The impact parameter plane in an ion-molecule collision. The projectile is moving out of the plane. 26
2.5 Impact parameter dependence of the probabilities P(b) of the atomic collision systems X^{2+}+H($Z^\star = 1.25$) $\rightarrow X^+ + H^+$, where X=(He,Ar,N), at collision velocities (a) $v_{coll} = 0.2$ a.u.; (b) $v_{coll} = 1.0$ a.u. 29
2.6 Absolute total cross sections for electron capture in ion - molecular ion collisions, as a function of collision velocity. The insets are polar plots of alignment-dependent cross sections, where θ is the angle between molecular axis and projectile velocity. The bottom graph is a plot the phase factor Φ_0 as a function of collision velocity. Arrows indicate where alignment-dependent cross section data was obtained. 32
2.7 Alignment dependence of the electron capture cross section for $He^{2+} + H_2^+$, $Ar^{2+} + H_2^+$ and $N^{2+} + H_2^+$ collisions. 33
2.8 Illustration of the alignment effect caused by the changing overlap of the geometrical cross section areas of the two molecular centers. (a) Schematic projection of the scattering amplitudes of each center onto the plane perpendicular to the projectile velocity. (b) Scattering amplitude used in this illustration. (c) Area of overlap of two disks $A(R_{perp})$ as a function of disk separation R_{perp}/b_0. b_0 is the disk radius. 35

3.1 The KSU ion-ion collision apparatus. 38

3.2 The gate at the intersection region, as seen by the molecular ion coming from the PS ion source. The gate is mounted on a vertical translation stage. 42
3.3 Top view of the beam cleaner. The ECR beam is coming in from the bottom, the PS beam from the left. The two arms are identical. . . . 44
3.4 Principle of a beam cleaner. The ion beam is travelling from left to right. It is initially doubly charged, but singly charged ions are created continously through electron capture from restgas in the shaded areas. In the top figure, no charge capture occurs while the beam is travelling through the field regions. In the bottom figure, charge capture occurs along the entire beam path. In the apparatus, the beam intersection is located between the two field regions. The detector would be to the right of the cleaner. 45
3.5 Background reduction through use of the beam cleaner in He^{+} - He^{2+} collisions. 47
3.6 Side- and top view of a delay-line detector with microchannel plates. In our setup, the diameter of the microchannel plates is 50 mm. . . . 48
3.7 Filterbox used to pick up the timing signal from the MCPs. The voltage rating of the capacitors needs to be in accordance with the voltage applied at the HV input. 49
3.8 Snapshots of a signal propagating in a delay line. Time moves downward. $\mathbf{t=t_0}$**:** the pulse is induced in the line. $\mathbf{t=t_1}$**:** the signal reaches the end of the closer right end of the delay line. $\mathbf{t=t_2}$**:** the signal reaches the further, left end of the delay line. 50
3.9 Electronics scheme used to display the image acquired with a delay-line detector on an oscilloscope in XY-mode. DA: Differential Amplifier; FA: Fast Timing Amplifier; CF: Constant Fraction Discriminator; D: Delay. 53
3.10 Triple-coincidence scheme. DA: Differential Amplifier; FA: Fast Timing Amplifier; CF: Constant Fraction Discriminator; CATSA: Charge And Time Sensitive Amplifier; SA: Spectral Amplifier; D: Delay; S: Stretcher; D&G: Gate and Delay Generator. A timing diagram for the shaded area is shown in fig. 3.11. 54
3.11 Self-coincidence timing scheme. 55

3.12 Algorithm used to recover second hit position signals, shown here for position signals on the two ends of the x-signal line. The first index specifies the hit number (1 through 16), the second index specifies the signal line end (1 or 2). A parameter, not shown in this flow diagram, specifies the depth of the search (or how many times the loops are repeated). 58
3.13 Coincidence spectra in N^{2+}+D_2^+ collisions. The histograms have been taken at 0.5ns/ch. The running time was 321465 s. Beam currents were $I_{D_2^+} = 35nA$, $I_{N^{2+}} = 54nA$. 65

4.1 Velocity mapping in geometrical optics (a) and in a SIMION ion trajectory simulation (b). 67

5.1 Coincidence spectra in N^{2+}-D_2^+-collisions. The three gates which are used in the background subtraction are: I, trues plus randoms; II, randoms; III, trues only. 72
5.2 D_2^+ - N^{2+} experimental data: The position spectra of the first and second hit. Background is subtracted. 73
5.3 D_2^+ - N^{2+} experimental data: The Coulomb-sphere as observed on the detector. (a): Projection onto the (x^{det}, y^{det}) plane. (b): Projection onto the (x^{det}, TOF) plane. (c): Projection onto the (y^{det}, TOF) plane. TOF is the time-of-flight direction. 74
5.4 Simulated slices (from SIMION) of a Coulomb-sphere at different times: left: as emerging from the collision in the $(\vec{v})_{cs}^{lab}$ frame; right: as viewed in detector coordinates $(\vec{x}, t)^{det}$, after passing the lenses and analyzers. In both cases, the molecular ion beam direction is into the page. . . 75
5.5 Simulation result: Projections of molecular fragments impacting on a two-dimensional detector surface. The fragments emerge from the collision distributed on rings. Triangles: $v_{cs,x} = 0$; Squares: $v_{cs,y} = 0$; Circles: $v_{cs,z} = 0$. 77
5.6 Detector image, obtained by deflecting a 1.55 keV D^+ beam in the collision region in a regular checkerboard pattern. (a) Raw image. (b) Image corrected for lens aberrations and converted into units of deflector voltage. 80
5.7 Ions deflected by the same amount, but originating from different locations along the beam axis. The images are created by ions whose origin is located *at* (solid circles), *before* (up triangles), or *after* (down triangles) the collision region center. The images are brought to overlap using a scaling factor of 0.88 (open circles). 82

5.8 The reconstruction procedure: Summary of the equations. Step-by-step results for both data and simulation. 90
5.9 Projections of the Coulomb-sphere in N^{2+}+D_2^+ collisions, corrected, calibrated and transformed into the collision system's center-of-mass frame. 91
5.10 Energy distribution of a D^+ fragment produced in a collision between N^{2+} and D_2^+. 93

6.1 The raw Coulomb sphere in the detector frame. Top: $Ar^{2+} + D_2^+$, v_{coll}=0.2 a.u.; second: $N^{2+} + D_2^+$, v_{coll}=0.2 a.u.; third: $He^{2+} + D_2^+$, v_{coll}=0.4 a.u.; bottom: $He^{2+} + D_2^+$, v_{coll}=0.5 a.u. 96
6.2 Slices of the Coulomb-sphere centered on the $(v_{cs,x}^{lab}, v_{cs,z}^{lab})$ plane. The directions of the ion beams in the lab frame are shown in black. The relative velocity direction and the direction perpendicular to the relative velocity are shown in red. The latter ones are different for each collision system. 97
6.3 Electron capture as a function of alignment angle. Bottom axis: Alignment with respect to the projectile velocity. Top axis: Alignment with respect to the relative velocity. Bottom graph: Angular distribution of the background collisions. 99
6.4 The laboratory- and center-of-mass angles 100
6.5 Result of symmetrizing the alignment curves for electron capture of Fig. 6.3 about θ_{cm}=90° for each collision system. The dotted lines are data from different θ_{lab} contributing to the same θ_{cm}. In those regions, the geometrical average is taken. 101
6.6 Electron capture as a function of molecular alignment with respect to the relative collision velocity. Left: Experimental data (the line is a smooth of the data points). The data has been symmetrized about $\theta_{cm} = 90°$ for every collision system. Right: Predictions of the interference model in sec. 2.2. 102

C.1 Detector image of the voltage grids used to calibrate the Ar^{2+} runs. 122
C.2 Detector image of the voltage grids used to calibrate the N^{2+} runs. . 123
C.3 Detector image of the voltage grids used to calibrate the He^{2+} runs. 124

D.1 Ion trajectories from a SIMION simulation of a magnetic sector field. The magnetic field lines point out of the page. 131

D.2 Time-evolution of the angles between beam direction and the internal velocities ($v_{cs,x}$, $v_{cs,z}$) of a Coulomb-sphere traveling through a magnetic field. The symbols are results from the SIMION simulation, the lines are the results of the analytical calculation. The sphere enters the magnetic field at t = 0 and exits at t=0.27 μs. 134
D.3 Ion trajectories from a SIMION simulation of 20° cylindrical electrostatic analyzer 136
D.4 Time-evolution of the molecular axes directions of a Coulomb-Sphere after passing a cylindrical electrostatic analyzer. 137

LIST OF TABLES

1.1 Q-values for electron capture in collisions between H_2^+ (E_{ion} = 29.9 eV) with He^{2+}, Ar^{2+} and N^{2+}. 11

1.2 Kinematic quantities of various projectile ions colliding at right angles with a 3.1 keV D_2^+ ion beam (v=3.86(5) m/s). 13

1.3 Properties of the H_2^+ molecular Ion [32]. R_0: equilibrium distance, D_0: dissociation energy, ν_0: fundamental vibrational frequency, E_{ion}: ionization potential. 20

3.1 EDL DLA800 differential amplifier in- and output connections. Input #1 is connected to ground. In brackets are the detector output connections. 52

3.2 Operating voltages of the MCP-DL detector for keV ion detection. . 53

3.3 Comparison of event rates with and without using the resorting algorithm. The event rates are normalized to the rate when no time-sum conditions are applied. TΣ H1 and TΣ H2 are the time-sum condition (Eq. 3.4) for both x and y of the first and second hit respectively. . . 57

3.4 Total cross section (taken from sec. 2.3), relative collision velocity and capture rate for electron capture in collisions between 3.1 keV D_2^+ with He^{2+}, Ar^{2+} and N^{2+}. E_{proj} is the energy of the atomic beam inside the interaction region. The beam currents are 20 nA for the molecular beam and 50 nA for the atomic beam. The form factor is 2 mm. Detector efficiencies are not included in the theoretical rates. The true rate as observed in the experiment is shown as well. 60

3.5 Measured rates in collisions of D_2^+ with He^{2+}, Ar^{2+} and N^{2+}. X^+ is the associated charge changed projectile. The current of the molecular beam is 20 nA. The projectile beam currents are 50 nA. The last row summarizes the rates calculated in section 3.4.2. The same BG capture cross section is assumed for all projectiles. The last column shows the theoretical rates from table 3.4, multiplied by the total detector efficiency of 7%. 64

3.6 Summary of the statistics of the four data sets: real-to-random ratio, total number of counts used in the analysis and total running time for each collision system. 64

C.1 Ar detector calibration 125
C.2 N detector calibration 126
C.3 He detector calibration 127
C.4 Coefficients from the 2d linear least squares fit. 128

D.1 Angles (in degrees) between beam- and internal velocities of a Coulomb-Sphere traveling through a magnetic field, at 1μs and 10μs after entering a magnetic field (it takes 0.27μs to traverse the field region). The last column shows the angles if the Coulomb sphere had not traveled through a field region. 134

Chapter 1

Introduction

1.1 Motivation

Single electron capture in ion-atom collisions is well understood. For electron capture from atomic hydrogen by protons, available data is reliable to within 25% for collision energies between few meV and several MeV [1]. Replacing the atomic target with a molecule breaks the cylindrical symmetry of the collision system. The alignment of the internuclear axis of the molecule introduces an additional degree of freedom. The question arises of how the molecular axis alignment affects the capture process.

One way to determine the molecular axis alignment in the collision is to measure the relative velocity of the molecular fragments, which recoil along the internuclear axis (providing the axial recoil approximation [2] is satisfied). This method works only if the final state of the molecule is dissociative. Removing an electron from a neutral molecule results in a bound molecular state for most processes. In addition, a neutral target molecule consists of at least two electrons. The role of electron correlation in the single-electron capture process is still not fully understood [3, 4].

The study of electron capture from a D_2^+ molecular ion by a doubly charged projectile allows one to investigate multi-center effects of single electron capture, while at the same time avoiding the multi-electronic character that comes into play in ion-

molecule experiments with neutral target molecules. On the other hand, this requires that one does an ion-ion collision experiment, with its inherent difficulties [5], since now both the projectile and the target are charged particles. The electron capture process leads to a D_2^{2+} unbound molecular ion. The internuclear axis alignment during the collision can be established through measuring the relative velocity between the two molecular fragments. This allows us to investigate whether electron capture is favored for particular alignment angles.

Several theories address electron capture from molecular targets. *Ab-initio* calculations are computationally intensive. Therefore, a simple-minded interference model [6] has been applied to our collision system. This model interprets scattering from a molecular target similar to a Young's double-slit experiment in optics.

So far only few experiments have been carried out in which the alignment of the molecular axis in a collision with a heavy ion projectile is determined (for a survey see section 1.2.2). In all those experiments, molecular gas targets were used. In our experiment, the molecular target is a molecular ion beam, where the target molecular ions travel at a speed comparable to that of the projectiles. Therefore the experimental technique used here differs significantly from the traditional gas-target experiments. The only other ion-ion collision experiments with molecular ion beams have been carried out in a merged-beams setup, determining total cross sections for mutual neutralization [7] and for associative ionization [8] in collisions of positively charged molecular ions with negative ions. Prior to this work, no theoretical or experimental total cross section data for the collision systems studied here (see section 1.4) were reported in the literature, to our knowledge. A collaborative effort with the Gießen ion-ion group resulted in total cross section measurements pertinent to this work [9].

1.2 Survey: Alignment Effects in Capture and Ionization from Diatomic Molecules

In the following, theories which have modeled capture from molecules by heavy ion impact are discussed, and some experiments in which the influence of the alignment of the molecular target was investigated. The focus here is on interference of scattering off the two molecular centers, which varies as the alignment of the molecule changes. One experiment indicates that alignment dependence may be caused by effects other than interference [10]. On the other hand, interference may survive even if the molecular alignment is averaged over [11].

1.2.1 Alignment Dependence in the Theoretical Models

Interference in collisions between ions and a molecular target was first pointed out by Tuan and Gerjuoy in 1960 [12]. While investigating charge transfer in collisions between protons and molecular hydrogen in the first Born approximation, they found interference of the two capture amplitudes from the two atomic centers to play a role for collision energies below 1 MeV. The phase responsible for the interference is $(\vec{\alpha} \cdot \vec{\rho})$, where $\vec{\alpha}$ is the momentum transfer to the projectile in the collision and $\vec{\rho}$ is the internuclear axis. Tuan and Gerjuoy pointed out the interference but did not investigate it further. The interference was the subject of a later work by McGuire and co-workers in 1988 [13]. Following Tuan and Gerjuoy's approach, they calculated differential cross sections as a function of the alignment of the internuclear axis. By keeping the molecular target at a fixed orientation, they observed the equivalent of interference fringes in the differential cross section (Fig. 1.1), which vanish when integrating over all molecular orientations.

Shingal and Lin [6] developed a simple model for electron capture from a molecule

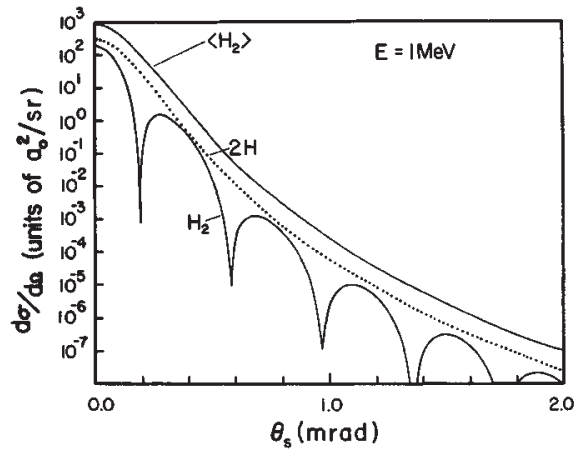

Figure 1.1: *Differential cross section for electron capture in 1MeV p^+-H_2 collisions. The molecular axis is at a fixed angle, here perpendicular to the projectile beam. From N.C. Deb et al, Phys. Rev. A* **38**, *3769 (1988)*

by an ion, from which they calculated total capture cross sections in H^+-H_2 and He^{2+}-H_2 collisions, as a function of internuclear axis alignment. It employs atomic scattering amplitudes which are added coherently to obtain the molecular scattering amplitudes. The atomic scattering amplitudes are obtained through a close-coupling approach [14], which is reliable down to velocity matching.

McGuire's and Rivarola's groups have a similar model for the high-velocity limit [15] in which total cross sections as a function of target alignment are calculated and compared to the experiment by Cheng and coworkers [16]. The experiment will be discussed shortly.

Kimura and coworkers developed an ab-initio theory for charge capture from neutral molecules, which is a close-coupling calculation using molecular basis functions, valid in the low- to intermediate velocity range. Initially, cross sections for capture from H_2 by different projectiles were calculated (H^+-H_2 collisions [17], Ar^+-H_2 collisions [18]). In both cases, the cross section varied when changing the alignment of the internuclear axis. Within this theory, no separate term emerges to which the

observed alignment dependence can be attributed. Recently this theory has been applied to collisions between protons and more complex molecules such as CH_4 [19] and C_2H_2 [20] and the relatively simple target CO molecule [21]. In these studies, the cross sections are calculated for different collision configurations, e.g. varying the symmetry axes of the molecules with respect to the projectile direction. The calculation is compared to experimental data. The molecules were randomly oriented in the experiments. Structures appear in the measured differential cross sections, in agreement with theory. Within this formalism, no separate term emerges which can be held responsible for any alignment or interference effects.

1.2.2 Alignment Dependence Observed in Collision Experiments

In the experiments discussed here, the molecular axis alignment in the collision is determined by measuring the relative velocity between the two fragments. In the recoil approximation [2], the two fragments recoil along the internuclear axis upon breakup of the molecule. For this approximation to be valid, a large amount of kinetic energy has to be released in the breakup of the molecule. Determining the alignment of the molecule through measuring the relative velocity vector of the two fragments also means that the alignment of a molecule can only be determined for reactions that lead to a dissociative final state of the molecule.

Alignment effects in Electron Capture

The alignment of the molecular axis was determined for single electron capture from D_2 by fast bare oxygen by Cheng and coworkers [16]. The collision energy was between 2 and 16 MeV. Fig. 1.2 shows their data for single electron capture followed by transfer ionization or excitation, which leads to the breakup of the molecule, of D_2 by 16 MeV O^{8+}. Alignment effects were found in the entire energy range. The alignment effects

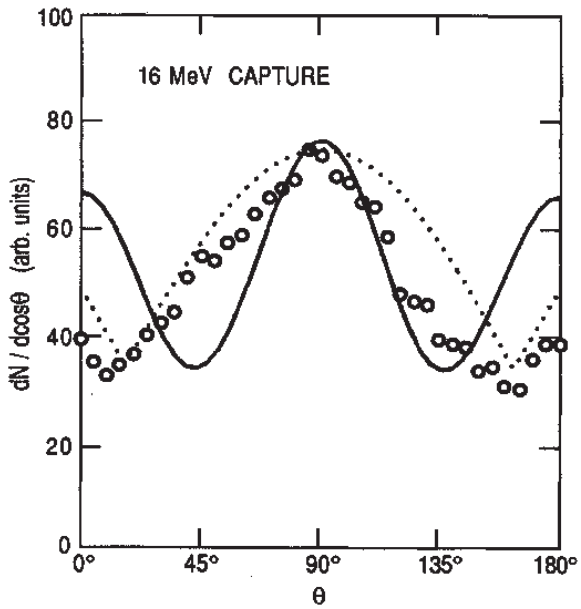

Figure 1.2: *Electron capture cross section as a function of angle between the projectile velocity and molecular axis in 16 MeV O^{8+}-D_2 collisions. Symbols: Experimental data, solid line: interference model prediction. The dotted line is a $1+c_1 cos(c_2 cos\theta)$ fit to the data. S. Cheng et al, Phys. Rev. A* **47**, *3923 (1993)*

could be explained in terms of the interference model by McGuire's group [15, 22]. On the other hand, double ionization of D_2 by fast O^{8+} showed no alignment dependence, in agreement with experiments by Edwards, Woods and coworkers [23] who measured the molecular axis alignment for double ionization of H_2 in p^+ - H_2 and e^- - H_2 and collisions.

Alignment Effects in Ionization

Alignment effects in multiionization of N_2 were observed by the group of H.O. Lutz [10, 24]. The data in Fig. 1.3 shows their results for He^{2+} impact onto N_2 at energies of 100-300 keV. If there were no alignment dependence, $\frac{dN}{d\theta} \propto \sin(\theta)$, which is what is observed for the N^+-N^+ and $(N_2)^{3+}$ breakup channels. For the higher ionization states, $(N_2)^{4+}$ and $(N_2)^{5+}$ however, the experimental distribution deviates significantly from $\sin(\theta)$, favoring electron removal from molecules aligned along the projectile beam.

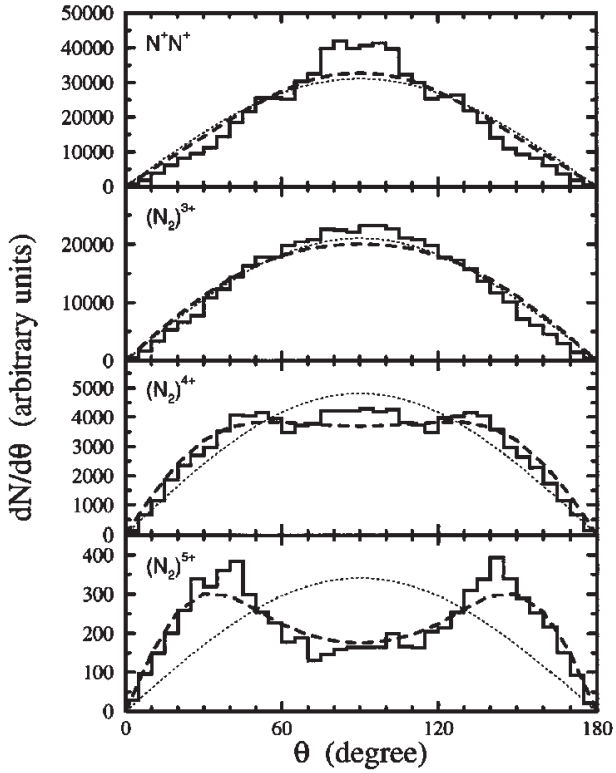

Figure 1.3: *Alignment dependence for multiionization of N_2 by 200 keV He^+ ions. The histograms are experimental data, the dotted line is the sin(θ) distribution. The dashed lines are the results of a theoretical calculation [26]. From U. Werner et al, Phys. Rev. Lett.* **79**, *1662 (1997)*

This is in qualitative agreement with the prediction of a purely geometrical model by Wohrer and Watson [25], and in quantitative agreement with a statistical model by Kabachnik et al. [26]. Both models do not include any interference from the two scattering centers.

In a very recent experiment, interference in electron emission from a molecular target was observed, while the molecular alignment was random. The experiment was done by Stohlterfoht and collaborators in 2001, at GANIL [11], colliding Kr^{34+} ions with a H_2 target. In the experiment, the absolute cross section of the emitted electrons as a function of electron energy was determined and compared to calculated

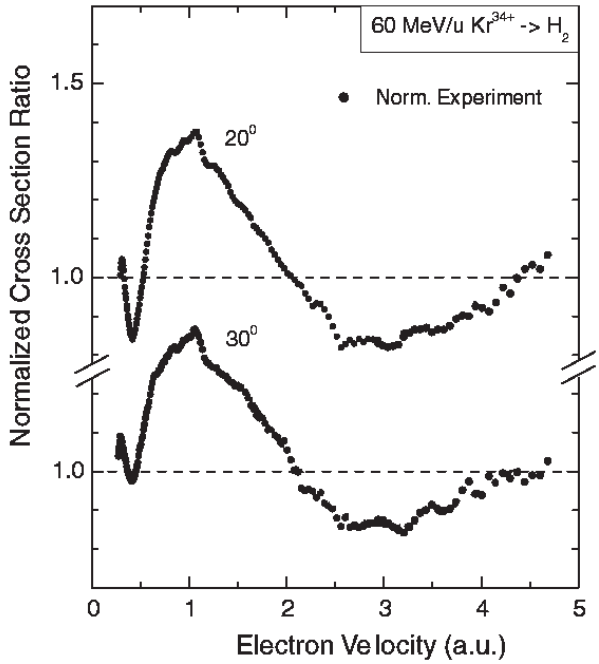

Figure 1.4: *Experimental-to-theoretical cross section ratios for electron emission in 60 MeV/u Kr^{34+} colliding with H_2 at electron emission angles of 20° and 30°. The dashed lines show a ratio of 1. The oscillatory structure is due to coherent electron emission from the two atomic centers of the H_2 molecule. From N. Stolterfoht et al, Phys. Rev. Lett.* **87**, *23201 (2001)*

absolute cross sections. The theoretical total cross sections were calculated assuming independent H atoms. Even though the experiment averages over all molecular orientations, the interference effect was predicted to survive in the electron energy spectra. Indeed, interference structures were observed in the experimental-to-theoretical total cross section ratio, as a function of electron energy. The oscillations were predicted to show a sin(kd) dependence, with k the momentum of the electron, and d the internuclear separation of the molecule, d=1.42 a.u. for H_2, which is what was observed (Fig. 1.4). The theoretical total cross sections were calculated assuming independent H atoms.

1.3 Outline of this work

This thesis is organized as follows. In sec. 1.4, the collision systems studied throughout this work are introduced. The laboratory and center-of-mass frames are defined in sec. 1.5. Sec. 1.6 discusses some relevant properties of the H_2^+ and D_2^+ target molecule used in these experiments. In chapter 2, a theoretical model for electron capture in ion-molecule collisions is presented. Within the model, the target molecular ions are described within the linear combination of atomic orbitals (LCAO) method which is subject of sec. 2.1. Total cross section results of the model calculation are presented in sec 2.3 and compared to total cross section measurements done in collaboration with the ion-ion group at Gießen. The model predictions for alignment dependence are shown in sec. 2.3.1. Chapter 3 discusses the ion-ion collision apparatus. Rate calculations to show the feasibility of the proposed experiments are done in sec. 3.4. The imaging properties of this apparatus are investigated through a SIMION ion trajectory simulation in chapter 4. The data analysis is described in chapter 5, and finally the experimental results are presented in chapter 6 and compared to predictions of the theoretical model. The work is concluded in chapter 7.

1.4 Reactions

The collision systems studied throughout this work involve electron capture from a D_2^+ molecular ion, by various projectiles:

$$\mathrm{Ar}^{2+} + \mathrm{D}_2^+ \rightarrow \mathrm{Ar}^+ + 2\mathrm{D}^+ \quad v_{coll} = 0.19 a.u. \tag{1.1}$$

$$\mathrm{N}^{2+} + \mathrm{D}_2^+ \rightarrow \mathrm{N}^+ + 2\mathrm{D}^+ \quad v_{coll} = 0.23 a.u. \tag{1.2}$$

$$\mathrm{He}^{2+} + \mathrm{D}_2^+ \rightarrow \mathrm{He}^+ + 2\mathrm{D}^+ \quad v_{coll} = 0.4 a.u., 0.5 a.u. \tag{1.3}$$

Note that the collision velocity was varied for the He^{2+} projectile. At these velocities, the collision time is less than 10 a.u., which corresponds to $t_{coll} \simeq 10^{-16}$ s. The time it takes the molecular target to perform one cycle of vibration or rotation is much longer ($t_{vib} \simeq 10^{-14}$ s, $t_{rot} \simeq 10^{-12}$ s), such that the molecular target can be considered frozen during the collision.

Once the electron is captured from the molecular ion, the two positively charged atomic centers are left without bond. Repelling each other, the two ions recoil along the internuclear axis. The Coulomb repulsion potential energy is converted into kinetic energy. Since this amounts to a relatively large amount of kinetic energy given to each fragment, this process is referred to as *Coulomb-explosion*.

The four collision systems differ in several ways. The Q-values of each collision system are tabulated in table 1.1. Q here is the electronic energy change in the capture, positive for exoergic capture. The $Ar^+(3p)$ and $N^+(2p)$ ionization potentials are very similar to the D_2^+ ionization potential, such that these two reactions can be considered quasi-resonant. The cross section for such a reaction increases with decreasing collision velocity, up to the Coulomb-limit where the collision energy is too small to overcome the repulsive force between the two charged collision partners. On the other hand, the $He^+(n = 2)$ ionization potential is much smaller, such that the reaction Q-value is very large and negative. In this case, the reaction is very non-resonant [27]. The cross section exhibits a maximum near v=1 a.u. and drops to zero as the collision velocity decreases. The probability for capture into $He^+(n = 1)$ is less likely, because of the even larger Q-value of -24.5 eV for this channel.

projectile ion	final state	Q-value [eV]
He^{2+}	He^{+}(n=2)	-16.3
Ar^{2+}	Ar^{+}(3p)	-2.3
N^{2+}	N^{+}(2p)	-0.3

Table 1.1: *Q-values for electron capture in collisions between H_2^+ (E_{ion} = 29.9 eV) with He^{2+}, Ar^{2+} and N^{2+}.*

1.5 Coordinate Frames

The measured data from any collision experiment depends on the particular configuration of the apparatus. A configuration independent representation of measured data is to express quantities in the center-of-mass frame, which depends on the relative motion of the two collision partners only. In this experiment, an additional difficulty arises from the use of a molecular target moving in the lab frame, with additional internal motion. The goal of this experiment is to investigate whether electron capture from the molecular ion is favored for a particular alignment of the molecular axis with respect to the relative collision velocity. In the following, the laboratory and center-of-mass frames of the collision system are defined, as well as a molecular frame in which the molecule's center-of-mass is at rest. The laboratory scattering angle and laboratory energies of the molecular fragments are calculated. In the laboratory overview, the detection system and its relation to the laboratory frame are explained.

1.5.1 Laboratory and Center-of-Mass Frames

The velocity diagram for the ion - molecular ion collision studied here is shown in Fig. 1.5. The projectile and molecular ion laboratory velocities are denoted by $\mathbf{v}_{proj}$ and $\mathbf{v}_{targ}$ respectively. The relative velocity between the two is shown as $\mathbf{v}_{rel}$. γ is the angle between target-and relative velocity. $\mathbf{v}_1$ and $\mathbf{v}_2$ are the laboratory velocities

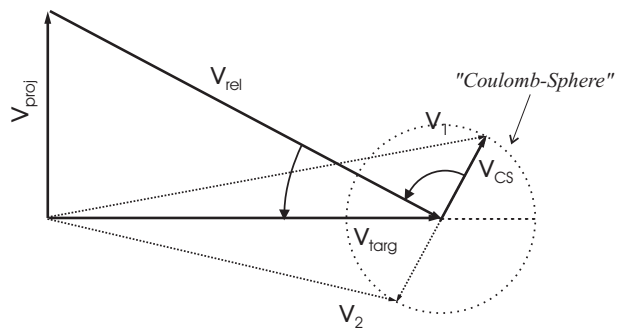

Figure 1.5: *The velocity diagram of the ion - molecular ion collision, after the molecular ion breaks up. The diagram is not to scale. The alignment angle θ is the angle between relative velocity v_{rel} and internuclear axis of the molecular ion.*

of the two molecular fragments, their relative velocity is $2\mathbf{v}_{CS}$, θ is the angle between the molecular axis and the relative velocity of the colliding beams $\mathbf{v}_{rel}$.

In the laboratory frame, the projectile and target ion beam intersect each other at right angles and define the laboratory frame through $\mathbf{v}_x^{lab} \parallel \mathbf{v}_{proj}$ and $\mathbf{v}_z^{lab} \parallel \mathbf{v}_{targ}$. The relative velocity lies in the $(\mathbf{v}_x^{lab}, \mathbf{v}_z^{lab})$-plane

$$\mathbf{v}_{rel} = \mathbf{v}_{targ} - \mathbf{v}_{proj} \tag{1.4}$$

and the angle γ between relative velocity and target (molecular) ion beam velocity is given by

$$\tan(\gamma) = \frac{v_{proj}}{v_{targ}} \ . \tag{1.5}$$

The CM-frame of the projectile-target collision system is defined such that $\mathbf{v}_z^{cm}$ points along the direction of the relative velocity, $\mathbf{v}_{rel}$, and $\mathbf{v}_y^{lab}$ and $\mathbf{v}_y^{cm}$ coincide. The transformation from the laboratory coordinate system into the CM-coordinate system then amounts to a clockwise rotation about the common $\mathbf{v}_y$-axis by γ.

The relative velocities in the collision systems studied are different, not only in magnitude, but also in direction, since both collision partners are moving. Anisotropies are expected to be symmetric about the relative velocity. Table 1.2 summarizes the

laboratory- and relative velocities, as well as the angle γ, for a 3.1 keV D_2^+ molecular ion beam colliding with the various projectile ions used in the experiment.

projectile ion	collision energy [keV]	collision velocity [10^5 m/s]	relative velocity [10^5 m/s]	[a.u.]	γ [deg]
Ar^{2+}	5.2	1.58	4.17	0.19	22
N^{2+}	7.2	3.14	4.98	0.23	39
He^{2+}	14.2	8.25	9.11	0.42	65
He^{2+}	23.2	10.5	11.19	0.51	70

Table 1.2: *Kinematic quantities of various projectile ions colliding at right angles with a 3.1 keV D_2^+ ion beam (v=3.86(5) m/s).*

1.5.2 Molecular Frame

As a result of the electron capture, the molecular ion breaks into two charged fragments. In the laboratory frame, the center-of-mass of the resulting Coulomb-sphere travels along the molecular ion beam at $\mathbf{v}_{targ}$. A momentum transfer to the target in the collision would cause the direction of the center-of-mass of the molecular fragments to deviate from the beam direction $\mathbf{v}_{targ}$. This effect is estimated to introduce a deviation of less than 0.1° at most and is therefore neglected.

In the molecular frame, the center-of-mass of the Coulomb-sphere ion is at rest. Given the velocities of the molecular fragments $\mathbf{v}_1$ and $\mathbf{v}_2$, the fragment's velocity with respect to the molecule's center-of-mass, $\mathbf{v}_{CS}$, is obtained through

$$\mathbf{v}_{CS} = \frac{\mathbf{v}_1 - \mathbf{v}_2}{2} \ . \tag{1.6}$$

Fig. 1.6 shows the Coulomb-sphere traveling along the target (molecular) ion beam. In the molecular frame, the angle between beam direction and $\mathbf{v}_{CS}$ assumes any angle between 0° to 360°. In the following, Eq. (1.6) is reversed to obtain the laboratory energy and scattering angle for each fragment.

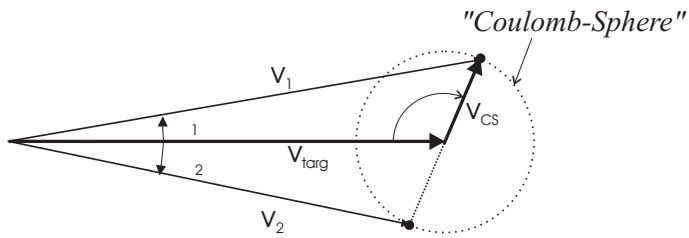

Figure 1.6: *The molecular frame. The velocity of the molecular ion's center-of-mass travels at the molecular ion beam velocity* $\mathbf{v}_{beam}$*, the molecular fragment's velocity with respect to the center-of-mass is* $\mathbf{v}_{CS}$*.* $\mathbf{v}_1$ *and* $\mathbf{v}_2$ *are laboratory velocities.*

1.5.3 Laboratory Energies and Scattering Angles of the Molecular Fragments

While exploring the feasibility of the proposed experiment, one needs to know the kinematic quantities, such as fragment energy and scattering angle, in the particular laboratory frame in which the experiment is being carried out. This conversion is done by adding the molecular ion beam velocity to the fragment velocity in the molecular frame, $\mathbf{v}_{CS}$.

$$\mathbf{v}_{1(2)}^{lab} = \mathbf{v}_{targ} \pm \mathbf{v}_{CS} \tag{1.7}$$

$\mathbf{v}_1$ and $\mathbf{v}_2$ are the velocities of the two fragments in the laboratory frame. The laboratory energy of each fragment is then

$$E_{1(2)}^{lab} = E_{targ}/2 + E_{CS} \pm 2\cos(\alpha)\sqrt{E_{targ}E_{CS}/2} \tag{1.8}$$

where α is the angle between molecular axis and beam direction, and E_{targ} is the energy of the target ion beam. The laboratory scattering angles ψ_1 and ψ_2 are obtained through

$$\tan(\psi_{1(2)}) = \pm\frac{v_{CS}\sin(\alpha)}{v_{targ} \pm v_{CS}\cos(\alpha)} \tag{1.9}$$

$$\approx \pm\frac{v_{CS}\sin(\alpha)}{v_{targ}} \tag{1.10}$$

This approximation is justified, because with E_{targ}=3.1 keV and E_{CS}=6 eV for each fragment, $v_{CS} \ll v_{targ}$. Fig. 1.7 shows one fragment's laboratory energy, and its laboratory scattering angle, as function of the alignment angle α.

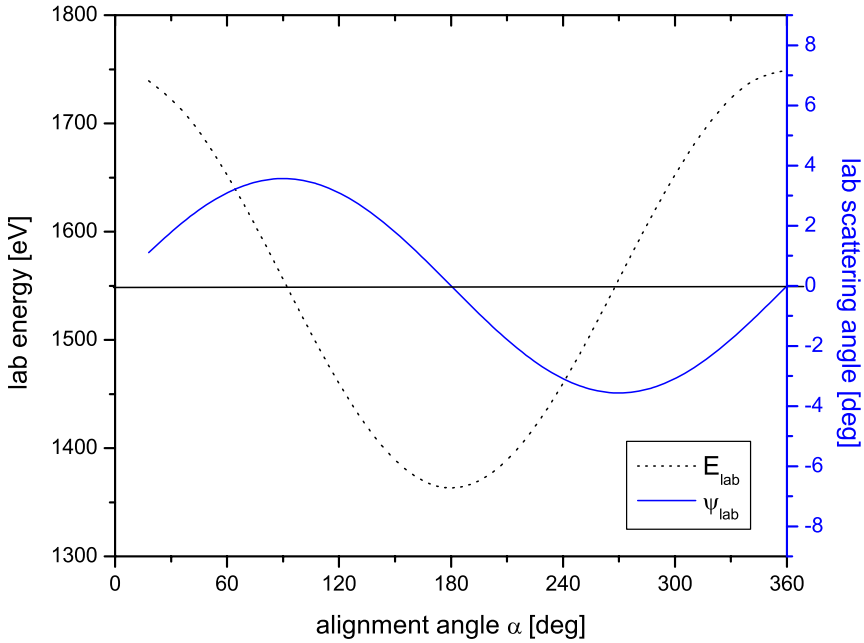

Figure 1.7: *Laboratory energy and laboratory scattering angle of one fragment emerging from a Coulomb explosion of a molecular ion, as a function of the angle between molecular axis and molecular ion beam direction. The beam energy is 3.1 keV, the Coulomb-energy is 6 eV per fragment.*

The maximum laboratory scattering angle is close to 4°. If left to expand freely, the Coulomb-sphere has reached a radius of 5 cm at a distance of 72 cm from the beam intersection, which is roughly the radius of the beam pipes in the apparatus. In order to project the Coulomb-sphere onto the detector 2 m downstream from the Coulomb explosion, an arrangement of ion-optical lenses is used (see section 4.1).

The kinetic energy of a fragment emitted forward along the molecular beam is 400 eV larger than the kinetic energy of a fragment emitted backwards. Because of this difference, the faster fragment arrives on the detector up to 150 ns before the

slower fragment.

1.5.4 Laboratory Frame and Laboratory Overview

The laboratory coordinate system is shown in Fig. 1.8. The $\mathbf{x}^{lab}$ axis points along the direction of the atomic ion beam. The $\mathbf{z}^{lab}$ axis points in the direction of the molecular ion beam. The $\mathbf{y}^{lab}$ axis is perpendicular to the plane defined by the two ion beams.

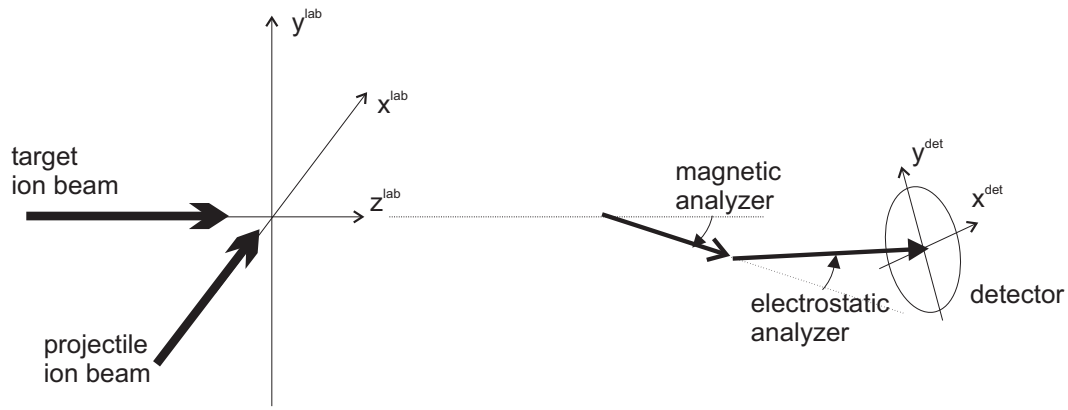

Figure 1.8: *The laboratory coordinate system. The molecular ion beam travels along the z^{lab}-axis and the projectile beam travels along the x^{lab} - axis. The detector surface normal is at 15° horizontal, 20° vertical to the z^{lab}-axis.*

After exiting the collision region, the molecular fragments pass through a magnetic analyzer, followed by an electrostatic analyzer, before reaching the detector. The magnetic analyzer deflects the product ions by 15° in the horizontal (z^{lab},x^{lab}) plane, and the electrostatic analyzer deflects those ions by another 20° (z^{lab},y^{lab}) plane. The detector surface is normal to the mean ion beam direction.

The deflection properties of the magnetic and electrostatic analyzers depend on the relative orientation of velocity and field vectors. Thus, the transformation from the detector space $(\vec{x}, t)^{det}$ into the laboratory frame $\vec{v}^{lab}$ is not a pure rotation. The effect of the analyzers onto a moving Coulomb sphere is studied in more detail in

appendix D on page 129. The reconstruction of the Coulomb-sphere as it emerged from the collision, from the data measured in the detector frame, is done in section 5.6 on page 85.

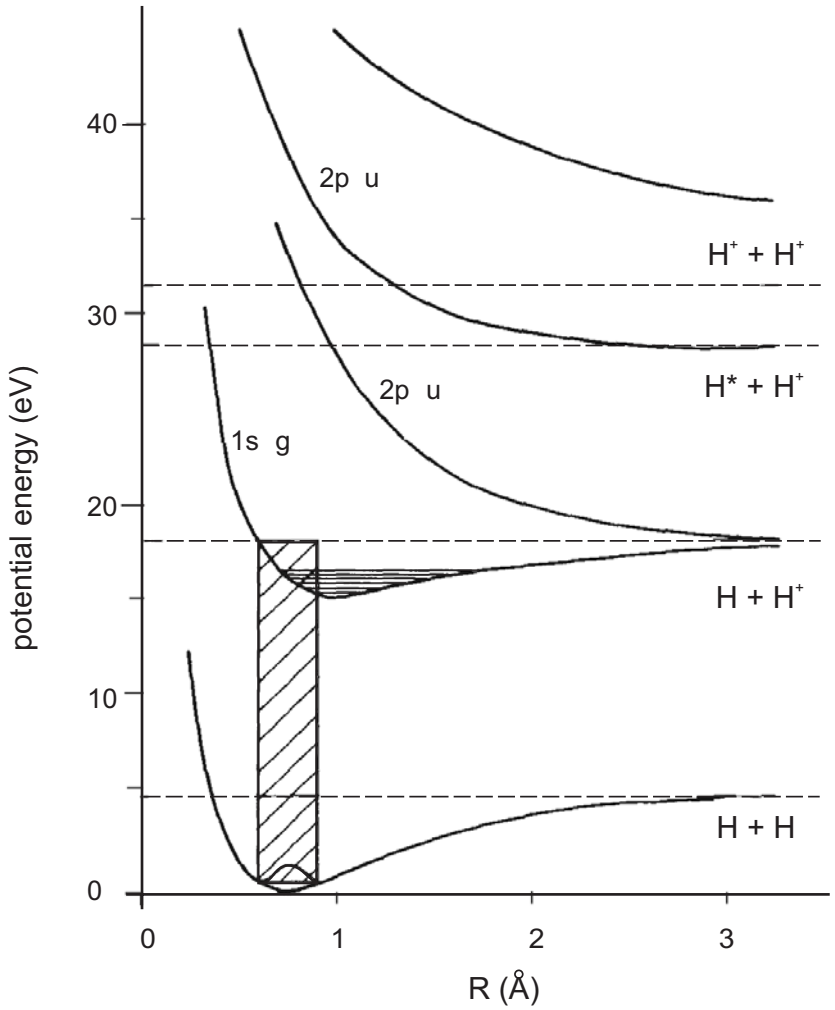

Figure 1.9: *Potential curves of the ground states of H_2 and H_2^{2+}, as well as the three lowest H_2^+ states. From [28].*

1.6 Properties of the H_2^+ Molecular Ion

The target in this experiment is H_2^+, a molecular ion which is created in a discharge ion source through electron bombardment of H_2 molecules. In this regime of high-energy electron-impact ionization, the Franck-Condon principle is valid and thus H_2^+ ions are created through a vertical electronic transition from the H_2 ground state.

Because the minima of the two potential curves do not occur at the same inter-

nuclear separation, the vertical transition results in vibrationally excited $H_2^+(1s\sigma g)$ molecular ions. For a pure Franck-Condon transition, the vibrational state distribution of the H_2^+ ions peaks at $\nu = 2$ [29]. The potential curves for the H_2 ground state and the three lowest states of the H_2^+ molecular ion are shown in Fig. 1.9, as well as for the fully ionized H_2^{2+}. The Franck-Condon region is marked in the figure.

For experimental reasons, in particular in the differential cross section measurements, D_2^+ molecular ions are used as a target instead of H_2^+. The potential curves of H_2^+ and D_2^+ are equal, excluding finite mass effects, since they depend on the nuclear charge, not on the nuclear mass [30]. In the harmonic oscillator approximation, the fundamental vibrational frequency scales with the square root of the reduced mass of the vibrating system. Thus, the vibrational states are spaced more closely for the D_2^+ molecular ions, and the Franck-Condon factor is largest for the $D_2(\nu = 0) \rightarrow D_2^+(\nu' = 3)$ transition [29].

During the collision with a doubly-charged projectile, the electron is captured from the target molecular ion. Since the collision is fast compared to the vibrational and rotational motion of the molecular ion, the electron capture results in a vertical transition from $H_2^+(1s\sigma g)$ ($D_2^+(1s\sigma g)$) to the H^+-H^+ (D^+-D^+) Coulomb-curve. The energy distribution of the ionized H^+-H^+ and D^+-D^+ fragments, shown in Fig. 1.10, reflects the vibrational state population of the parent H_2^+ (D_2^+) molecular ion. This energy distribution was calculated by M.H. Prior [31] from a vertical projection of the H_2^+ (D_2^+) wave-packet onto the two-ion Coulomb-curve. The distribution is an incoherent sum of the energy distributions calculated by reflecting vibrational states of D_2^+ onto the D_2^{2+} potential curve. The relative populations were given by the Franck-Condon factors for a transition from the neutral molecule's ground state. By the time the molecular ion reaches the collision, the coherence of the initial wave-packet has been lost.

R_0 (Å)	D_0 (eV)	ν_0 (eV)	E_{ion} (eV) (at R = ∞)	E'_{ion} (eV) (at R_0)
1.06	2.65	0.285	16.25	29.97

Table 1.3: *Properties of the H_2^+ molecular Ion [32]. R_0: equilibrium distance, D_0: dissociation energy, ν_0: fundamental vibrational frequency, E_{ion}: ionization potential.*

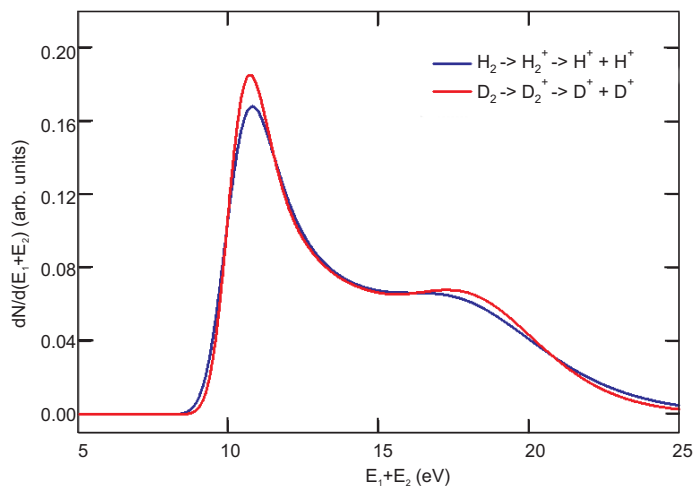

Figure 1.10: *Energy distribution of ionized H^+-H^+ and D^+-D^+ molecular fragments calculated by M.H. Prior [31], as described in the text.*

The energy distribution of the H^+-H^+ (D^+-D^+) fragments (Fig. 1.10) is wide. At the lower energies, it has a sharp onset with a peak around E_1+E_2=11 eV. Towards higher energies, the peak has a broad shoulder extending to about E_1+E_2=20 eV.

Chapter 2

Theoretical Model

2.1 The D_2^+ Molecular Wave function in the LCAO Approximation

The D_2^+ molecular ion and its isotopes is the simplest stable molecule. It consists of two deuterons and one electron (see Fig. 2.1). The Schrödinger equation for this system (in atomic units) is

$$\left(-\frac{1}{2}\nabla_r^2 - \frac{1}{r_A} - \frac{1}{r_B} + \frac{1}{R} - E_s\right)\Psi_s = 0 \tag{2.1}$$

where R is the internuclear separation of the two protons, and r_A and r_B are the distances between the electron and proton A and B, respectively. In principle, this equation is separable at fixed R, and the bound states can be written analytically. Here, an approximation method is discussed instead, the linear combination of atomic orbitals (LCAO) method [32], because of its relevance to the collision model that is used to calculate collision cross-sections.

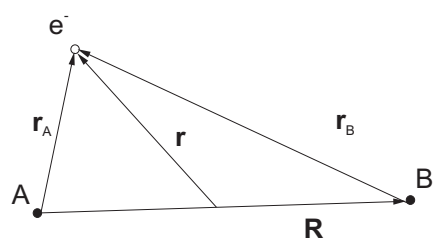

Figure 2.1: *The deuterium molecular ion.*

In the LCAO approximation, the hydrogen molecular ion ground state wave function is constructed from a linear combination of hydrogen atom ground state wave

functions $\psi_{1s}(r)$:

$$\Psi_g(\mathbf{R};\mathbf{r}) = \frac{1}{\sqrt{2}}[\psi_{1s}(r_A) + \psi_{1s}(r_B)] \tag{2.2}$$

Only the gerade symmetry is considered here because it results in a bound ground state. The ground state energy is given by the expectation value of the Hamiltonian,

$$E_g(R) = \frac{\int \Psi_g^\star H \Psi_g d\mathbf{r}}{\int |\Psi_g|^2 d\mathbf{r}} \ . \tag{2.3}$$

A limitation of this approximation is that the wave function $\Psi_g(R=0)$ does not describe the united-atom limit correctly, where the molecular ion goes to the united-atom limit, $He^+(1s)$, with Z=2. A better approach is to use hydrogenic wave functions with variable effective charge, $u_{1s}(Z^\star, r) = \left(\frac{Z^{\star 3}}{\pi}\right)^{1/2} e^{-Z^\star r}$ in Eq. (2.2), leaving the effective charge a parameter which is determined at every internuclear separation R by applying the variational principle to the ground state energy E_g in Eq. (2.3). (See [33], for example). The resulting effective charge as function of internuclear distance is plotted in the top graph of Fig. 2.2. At R=0, $Z^\star = 2$, and at large internuclear separations, $Z^\star$ approaches 1. The bottom graph of Fig. 2.2 shows the ground state energy E_{1s} as a function of internuclear distance. The Coulomb term $1/R$ is not included in this calculation. The solid line shows the LCAO result with Z=1. The dashed line is the result from the variable $Z^\star$ LCAO, which is very close to the exact calculation, shown by the dash-dotted line. At the D_2^+ equilibrium separation of $R_0 = 2$ a.u., the effective charge is 1.25 and the ionization potential of the ground state is 1.13 a.u. The ionization potential at the equilibrium separation is by 0.5 a.u. larger than in the separated atom limit ($R \to \infty$). The increase is caused by the presence of the second proton only 2 a.u. away.

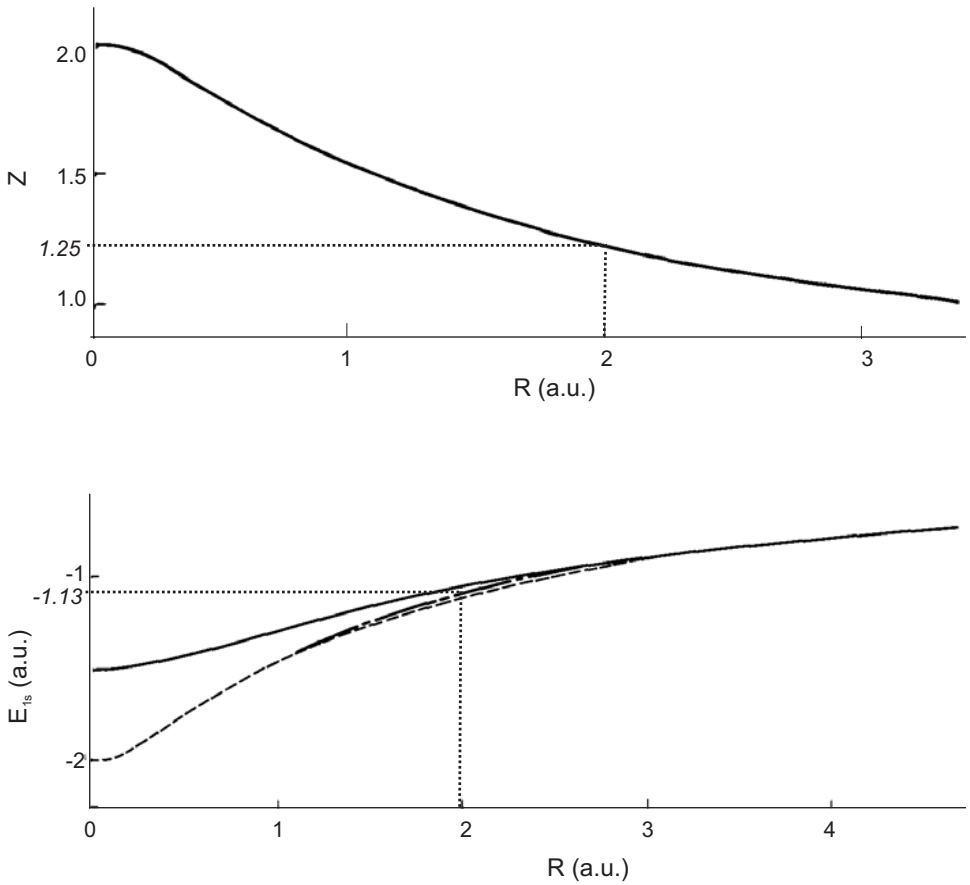

Figure 2.2: *Effective charge $Z^\star$ and ground state energy E_{1s} of the D_2^+ $(1s\sigma g)$ state as a function of internuclear separation R calculated from the LCAO model with variable $Z^\star$. Bottom graph: Solid line: result from LCAO with constant Z=1. Dashed line: result from variable $Z^\star$ LCAO. Dash-dotted line: exact calculation. From [33].*

2.2 Theoretical Model: Electron Capture in Collisions between Ions and Molecules

To obtain cross sections for the molecular ion collision system, an atomic model for electron capture in ion-molecule collisions, developed by Shingal and Lin in 1989 [6], has been implemented. Within this model, orientation-dependent cross sections can be calculated, as well as total cross sections. The model does not include angular scattering of the projectile ion. The derivation of this model is outlined in the following; for further details refer to their article.

The collision geometry is shown in Fig. 2.3. The molecule consists of two equi-mass atoms A and B, separated by the internuclear distance R. The coordinate origin C is located at the midpoint of the internuclear axis. The projectile travels in the z-direction and b is the impact parameter. At keV collision energies, the molecular target can be considered frozen during the collision, since the collision time is much shorter than the rotational and vibrational periods of the nuclei. Therefore, within this model, capture cross sections are determined for fixed values of the internuclear distance R.

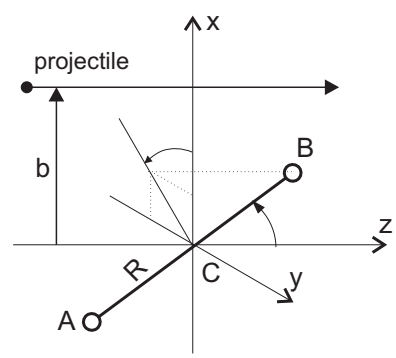

Figure 2.3: *Geometry for an ion-molecule collision.*

The molecular target initial wave function can be approximated by a time-dependent LCAO wave function

$$\Psi_i(\vec{r}_A, \vec{r}_B, t) = \frac{1}{\sqrt{2}} \left[\psi_{1s}(\vec{r}_A) + \psi_{1s}(\vec{r}_B)\right] \times \exp\left(-iE_i t\right) \ . \tag{2.4}$$

E_i is the initial state electronic energy and $\psi_{1s}(\vec{r})$ is a hydrogenic ground state wave function centered at atoms A(B). After the collision, the electron moves along with the

projectile ion, which is accounted for by including the plane wave electron translation factor, $\vec{v} \cdot \vec{r} - v^2 t/2$, in the final state wave function

$$\Psi_f(\vec{r}, t) = \psi_f(\vec{r}_P) \exp\left[-i(E_f t - \vec{v} \cdot \vec{r} + v^2 t/2)\right] \ . \tag{2.5}$$

Here, $\psi_f(\vec{r}_P)$ is the time-independent final state of the projectile and E_f is the final state electronic energy. Originally, the collision was treated in a perturbation model to obtain the scattering amplitudes. Later, the model was generalized to include the non-perturbative regime. Within perturbation theory, molecular electron capture amplitudes are obtained through

$$a_{fi} = \int_{-\infty}^{\infty} \langle \Psi_i | V | \Psi_f \rangle \, dt \ . \tag{2.6}$$

Inserting the initial state from Eq. (2.4), this capture amplitude turns into a sum of electron capture amplitudes for each molecular constituent A and B:

$$a_{fi} = \frac{1}{\sqrt{2}} \int_{-\infty}^{\infty} \left[\langle \psi_{1s}(\vec{r}_A) | V | \Psi_f \rangle + \langle \psi_{1s}(\vec{r}_B) | V | \Psi_f \rangle\right] \times \exp\left(iE_i t\right) \, dt \ . \tag{2.7}$$

Generally, in an ion-atom collision, the collision geometry is such that the coordinate origin is located at the target and $t = 0$ when the projectile is at closest approach to the target. Here, the coordinate origin, as well as the distance of closest approach, is with respect to the midpoint of the molecular axis. For the integral of each matrix element, the coordinate origin is now shifted separately to the respective centers, A or B, by setting $\vec{r} = \vec{r}_{A(B)} \pm \vec{R}/2$ and changing the integration variable to $d\vec{r}_{A(B)}$ for each center A(B). Also the time-integration is shifted by a constant τ such that t=0 occurs when the projectile is at closest approach to either center A or B. τ is the time it takes the projectile to travel from A to C (or B to C), $\tau = \pm(R\cos\theta)/(2v)$.

Performing these transformations and retaining only the relative phase, the molecular capture amplitude a_{fi} can be written as a coherent sum of two ion-atom collision

capture amplitudes $a(\vec{b}_A)$ and $a(\vec{b}_B)$, where $\vec{b}_A$ and $\vec{b}_B$ are impact parameters relative to atom A or B, and $a(\vec{b_{A(B)}})$ is the amplitude for capture of an electron from an atomic center A or B:

$$a_{fi} = \frac{1}{\sqrt{2}} \left\{ a(\vec{b}_A) + a(\vec{b}_B) \times \exp\left[-iR\cos(\theta) \left(\frac{v}{2} - \frac{\omega}{v} \right) \right] \right\} . \tag{2.8}$$

R is the internuclear separation, θ is the alignment angle of the molecular axis with respect to the projectile beam direction, v is the relative velocity and $\omega = E_f - E_i$ is the change in internal energy or the negative reaction Q-value (Q $\geq$ 0 exothermic). The impact parameters $\vec{b}_A$ and $\vec{b}_B$ are determined from Fig. 2.4.

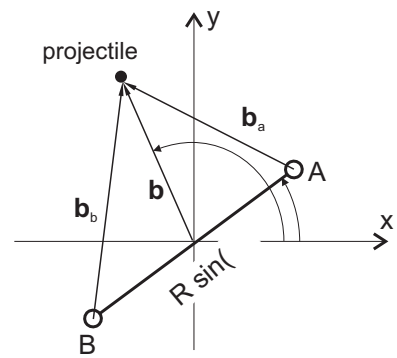

Figure 2.4: *The impact parameter plane in an ion-molecule collision. The projectile is moving out of the plane.*

Equation (2.8) allows one to calculate scattering amplitudes for an ion-molecule collision system from the atomic scattering amplitudes $a(\vec{b})$ of the corresponding ion-atom collision system. Initially, the Eq. (2.8) was derived from a first order perturbation model. The authors then generalized it to cases where the electron capture can no longer be treated perturbatively. Then a semi-classical close-coupling approach [14] could be used to obtain the scattering amplitudes for the corresponding ion-atom collision system.

From the scattering amplitude in Eq. (2.8), probabilities are calculated through

$$P(\vec{b}) = |a_{fi}|^2 . \tag{2.9}$$

Since the model is being applied to non-perturbative collisions, the transition probabilities of the atomic collision system might be large, in which case the transition probability of the molecular collision system could exceed unity. To guarantee the

probability to be equal or less than unity, the ansatz $\sin^2\sqrt{P}$ is used in place of P [6]. Orientation-dependent cross sections are obtained by integrating the probability

$$\sigma(\theta,\phi) = \int_0^{2\pi}\int_0^{\infty} bP(b,\beta)\,db\,d\beta\ . \tag{2.10}$$

As opposed to ion-atom collisions, this integral is two-dimensional because the impact parameter now is a vector $\vec{b} = (b,\beta)$ that lies in the plane perpendicular to the projectile direction as shown in Fig. 2.4. Integration over all angles β restores the cylindrical symmetry. Averaging over all orientation results in the total cross section

$$\bar{\sigma} = \frac{1}{4\pi}\int \sigma(\theta,\phi)\,d\Omega \tag{2.11}$$

This model has been applied to collisions between H_2^+ molecular ions and He^{2+}, Ar^{2+} and N^{2+} projectiles. The internuclear separation of the nuclei in the hydrogen molecular ion, R, is replaced by its mean value <R>, with <R>=R_0 in the harmonic oscillator approximation (R_0 is the equilibrium distance of H_2^+). The atomic electron capture amplitudes were calculated for H($Z^\star$) - X^{2+} collisions (X=He,Ar,N) through close-coupling. The hydrogenic atom had effective charge of $Z^\star = 1.25$, obtained from the LCAO model description of H_2^+ at the equilibrium distance of 2 a.u.. At this internuclear separation, the ionization potential ($=E_f$) is 1.13 a.u.. The He^{2+} projectile is a bare nucleus with a Coulomb charge of Z=2. 10 projectile states are included in the calculation. The two projectiles with core electrons, Ar^{2+} and N^{2+}, were described through spherical symmetric model potentials with parameters chosen such that the binding energy of the p-state was reproduced [34]. Only capture into Ar^+(3p) or N^+(2p) was assumed. For the Ar^{2+} projectile,

$$V_{Ar}(r) = \frac{-2 + (-16 + 2.1703r)e^{-2.1703r}}{r} \tag{2.12}$$

was used, which gives a binding energy of 1.016 a.u. for Ar^+(3p) (experimental:

1.015 a.u.). The N^{2+} core was described through

$$V_N(r) = \frac{-2 + (-5 + 2.375r)e^{-2.375}}{r} \tag{2.13}$$

is used, which gives a binding energy of 1.08 a.u. for $N^+(2p)$ (experimental: 1.09 a.u.). The experimental data for the ionization potentials were taken from [35]. For the Ar^{2+} and N^{2+} projectiles, only the (np0) and (np1) states are included in the calculation (with n=3 for Ar, n=2 for N)[1].

Fig. 2.5 shows the probabilities for the atomic systems as a function of impact parameter, at collision velocities of v_{coll} = 0.2 a.u. and v_{coll} = 1 a.u. For the N^{2+} projectile, P(b) is shown only at v_{coll} = 0.2 a.u.. The P(b) distributions for the Ar^{2+} and the N^{2+} projectiles oscillate strongly, an effect which is due to the small reaction Q-values. Also, the probabilities extend to relatively large impact parameters, dropping off around b=6 a.u. only. This is true for both collision velocities. In contrast, for the He^{2+} projectile, the P(b) distribution is much narrower, in particular at the lower velocity, and there is no oscillatory structure. This is due to the large reaction Q-value of about 0.6 a.u.. Note that if a different target were used, like atomic or molecular hydrogen, this latter collision system would be quasi-resonant.

2.3 Model Calculation Results; Comparison to Experiment for Total Cross Sections

The total electron capture cross sections (TCS), calculated using the above model, are shown in Fig. 2.6 and compared to experimental data taken at the ion-ion collision apparatus of the University of Gießen (Germany) [9] (this paper is reprinted in appendix A). Calculation results are shown as a line, the experimental data as symbols. The experimental error bars shown include statistical error only. The absolute

[1]The notation used to label the electronic state is (n, l, m_l).

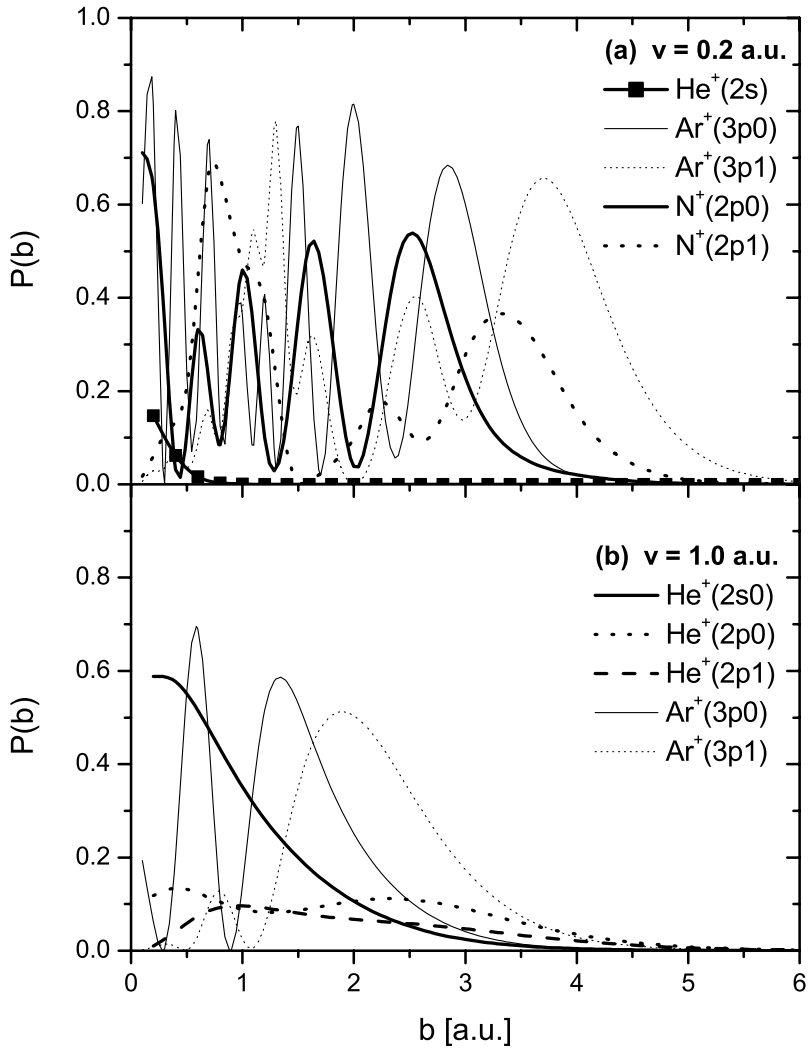

Figure 2.5: *Impact parameter dependence of the probabilities P(b) of the atomic collision systems* $X^{2+} + H(Z^{\star} = 1.25) \rightarrow X^{+} + H^{+}$, *where X=(He,Ar,N), at collision velocities (a)* $v_{coll} = 0.2$ *a.u.; (b)* $v_{coll} = 1.0$ *a.u.*

overall uncertainty in the experimental data is 21%.

The top panel shows the TCS in H_2^+ - He^{2+} collisions as a function of collision velocity. Both the data and the calculation exhibit a pronounced maximum around v_{rel} = 1 a.u.. This feature is due to the relatively large Q-value of this reaction, Q=-16.3 eV for capture into He^{2+}(n=2). This is a very non-resonant reaction.

The inset of the top panel shows polar plots of alignment-dependent cross sections for the H_2^+ - He^{2+} collision system. The average of the alignment dependent cross sections is normalized at each velocity. The direction of the collision velocity is to the right. The rapid change in shape at lower velocities is due the velocity dependence of the phase factor in the coherent sum in Eq. (2.8), $\Phi_0 = -R(\frac{v}{2} - \frac{\omega}{v})$.

The middle graph shows the TCS in H_2^+ - Ar^{2+} collisions. The TCS velocity dependence is very different, which is due to the much smaller reaction Q-value of only -2.3 eV, for capture into Ar^+(3p). The smaller Q-value shifts the maximum of the TCS curve to lower relative velocities, such that only the tail of the distribution is observed in this range. Also the theoretical total cross section for H_2^+ - N^{2+} collisions is shown, together with a polar plot of the alignment-dependent cross section. The alignment dependence for H_2^+ - Ar^{2+} collisions is very similar (see Fig. 2.7 on page 33). No experimental total cross section data has been taken using N^{2+}-projectiles, but the alignment dependence has been measured for this collision system.

The bottom graph shows the phase Φ_0 as a function of collision velocity. For the He^{2+} projectile, Φ_0 falls off steeply with increasing relative velocity, leveling off at about $v_{rel} = 0.6$ a.u.. In contrast, the phase factors for the Ar^{2+} and N^{2+} projectiles vary little as a function of velocity. Because the Q-values of those reactions is much smaller, the phase factor is 'attenuated' and does not go through a full cycle of 2π in the range shown. For those collision systems, the present theoretical model predicts the alignment dependence to change little as a function of velocity, as for the He^{2+} projectile at velocities above 0.6 a.u..

In the bottom graph, the velocity ranges accessible for alignment-dependent measurements are indicated. Arrows indicate where the actual measurements were taken. The velocity ranges differ from the velocity region where the total cross section data has been obtained. As mentioned before, the total cross section data has been ob-

tained using the Gießen ion-ion apparatus, whereas alignment dependent measurements are performed using the KSU ion-ion apparatus, which covers a different range of collision energies.

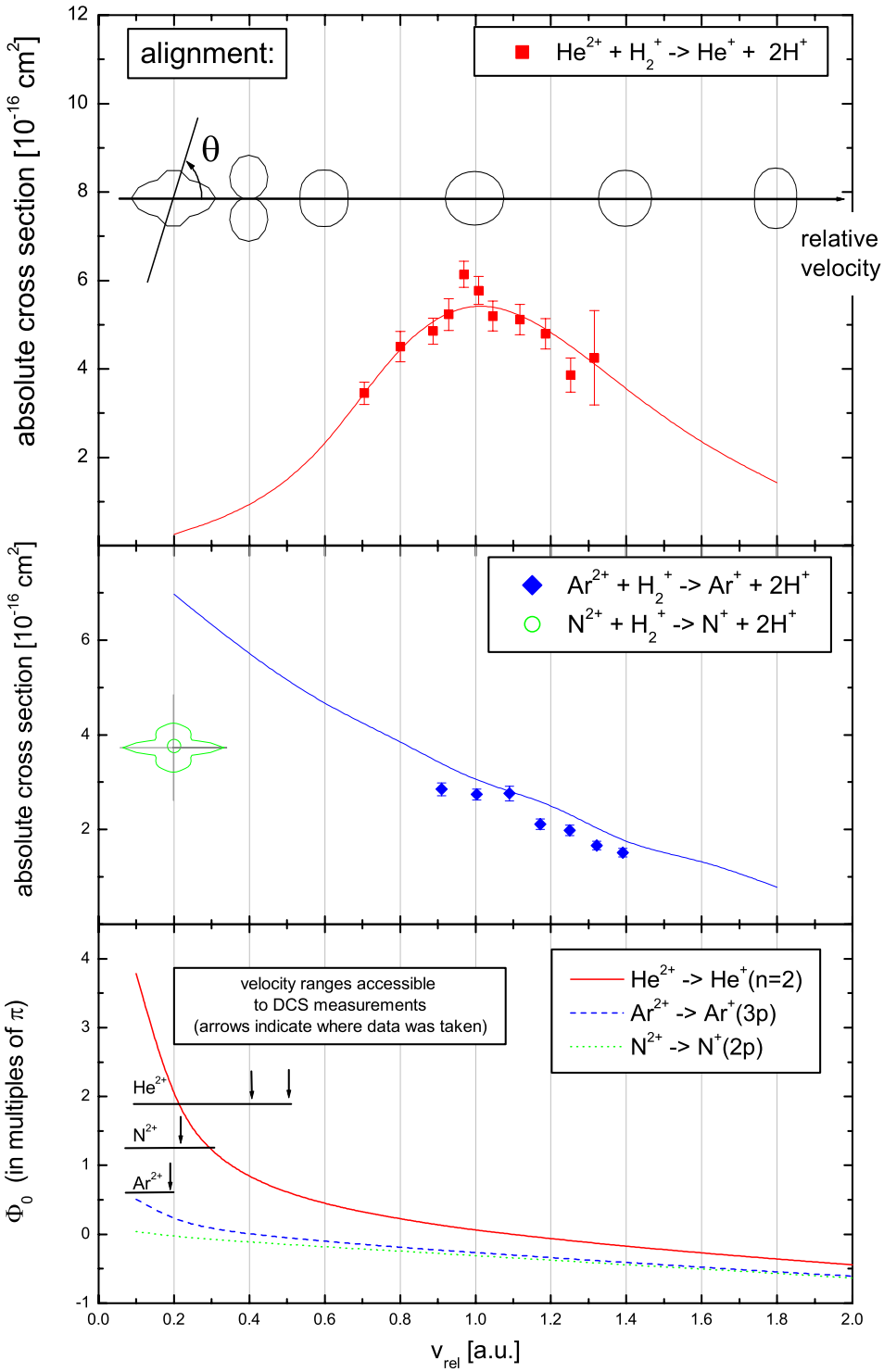

Figure 2.6: *Absolute total cross sections for electron capture in ion - molecular ion collisions, as a function of collision velocity. The insets are polar plots of alignment-dependent cross sections, where θ is the angle between molecular axis and projectile velocity. The bottom graph is a plot the phase factor Φ_0 as a function of collision velocity. Arrows indicate where alignment-dependent cross section data was obtained.*

2.3.1 Model Predictions for the Molecular Alignment Dependence

Fig. 2.7 shows the model predictions for the alignment dependence of the electron capture cross sections, for $X^{2+}+H_2^+ \rightarrow X^+ + 2H^+$ (X=He,Ar,N), at collision velocities where measurements were carried out.

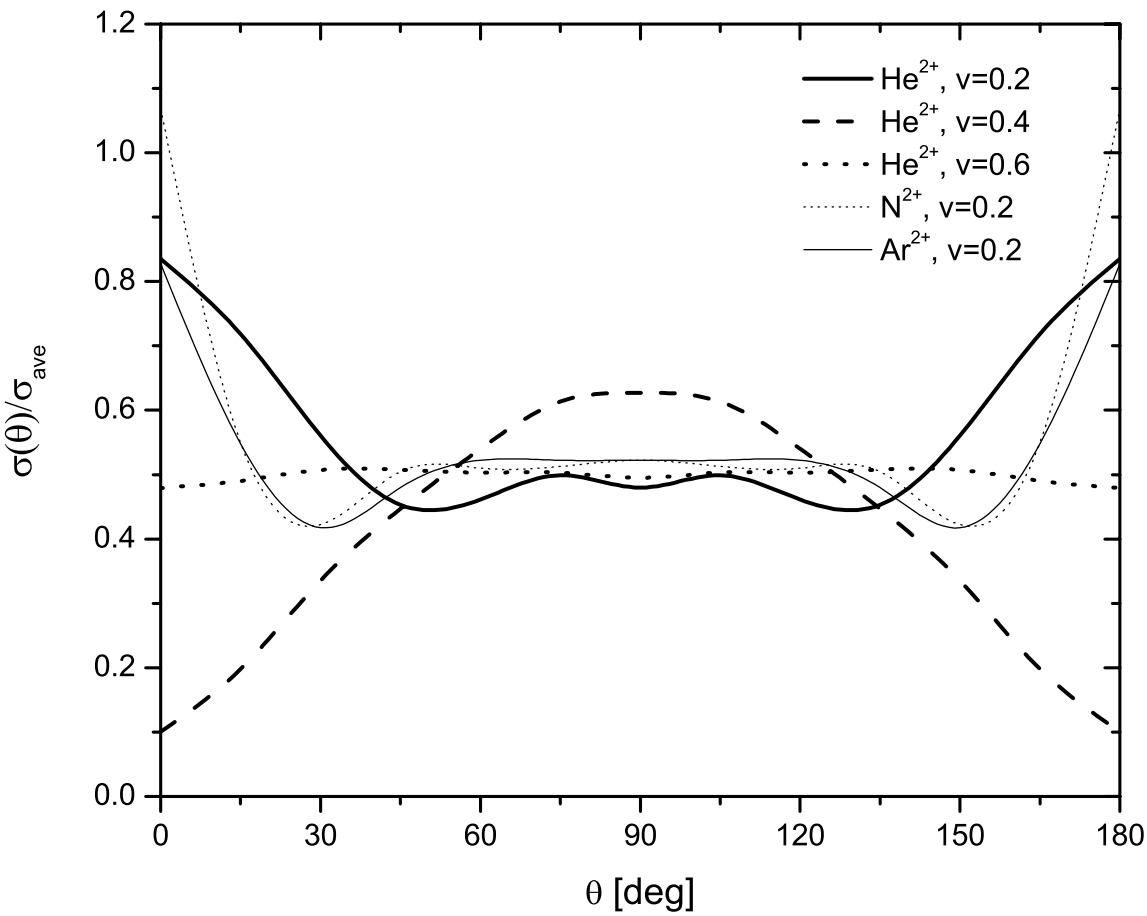

Figure 2.7: *Alignment dependence of the electron capture cross section for* $He^{2+}+H_2^+$, $Ar^{2+}+H_2^+$ *and* $N^{2+}+H_2^+$ *collisions.*

At this point it is useful to re-examine the equation which governs the alignment dependence. Inserting Eq. (2.8) into Eq. (2.9), the probability for electron capture from an aligned H_2^+ molecular ion is

$$P(\theta) = \frac{1}{2}\left\{|a_A|^2 + |a_B|^2 + 2\mathrm{Re}(a_A a_B^\star)\cos(\Phi_0\cos(\theta))\right\} \tag{2.14}$$

where θ is the angle between the molecular axis and the projectile velocity. As before, $\Phi_0 = -R(\frac{v}{2} - \frac{\omega}{v})$ from Eq. (2.8). For clarity, $a(\vec{b}_{A(B)})$ has been replaced by $a_{A(B)}$.

The interference term in this equation consists of two factors which vary as a function of alignment angle θ, one of which is the relative phase between the two centers, $\cos(\Phi_0\cos(\theta))$. The alignment dependence of this factor is determined by the magnitude of Φ_0, since $\cos(\theta)$ varies between 1 and -1. This factor predominantly determines the alignment dependence of electron capture in $He^{2+}-H_2^+$ collisions, as mentioned earlier. Since the Q-value for this collision system is large, Φ_0 varies as a function of velocity. The alignment curves changes from favoring parallel alignment at v=0.2 a.u. to favoring perpendicular alignment at v=0.4 a.u. (Fig. 2.7). At v=0.6 a.u., the alignment effect is canceled out and it remains canceled in the entire velocity region where the total cross section curve has its maximum (see Fig. 2.6).

The second factor in Eq. (2.14) which is causing an alignment dependence is the product $\mathrm{Re}(a_A a_B^\star)$, since the spatial overlap of the two molecular centers varies with molecular axis alignment. This is illustrated in Fig. 2.8. The atomic scattering amplitudes are assumed to be real as in Graph (b), with $a(b) = a_0$ for $b \leq b_0$ and $a(b) = 0$ for $b > b_0$. Setting the phase factor $\Phi_0 = 0$ in Eq. (2.14), and integrating the probability as in Eq. (2.10), one obtains the alignment dependent cross section of $\sigma(\theta) = \pi b_0^2 a_0^2\{1 + A(R_{perp})\}$. $A(R_{perp})$ describes the overlap of the two 'scattering disks' with $A(R_{perp}) = 1/(\pi b_0^2 a_0^2)\int Re(a_A a_B^\star)dbd\beta$, as shown in Fig. 2.8(a). $R_{perp} = R_0\sin(\theta)$ is the disk separation. The area of overlap varies as the molecular axis

alignment changes: for molecules aligned parallel to the projectile velocity, $R_{perp} = 0$ and $A(R_{perp}) = 1$. For molecules aligned perpendicular to the projectile velocity, $A(R_{perp}) = 0$ if $b_0 < R_0$. Graph (c) of Fig. 2.8 shows the overlap area as a function of disk separation.

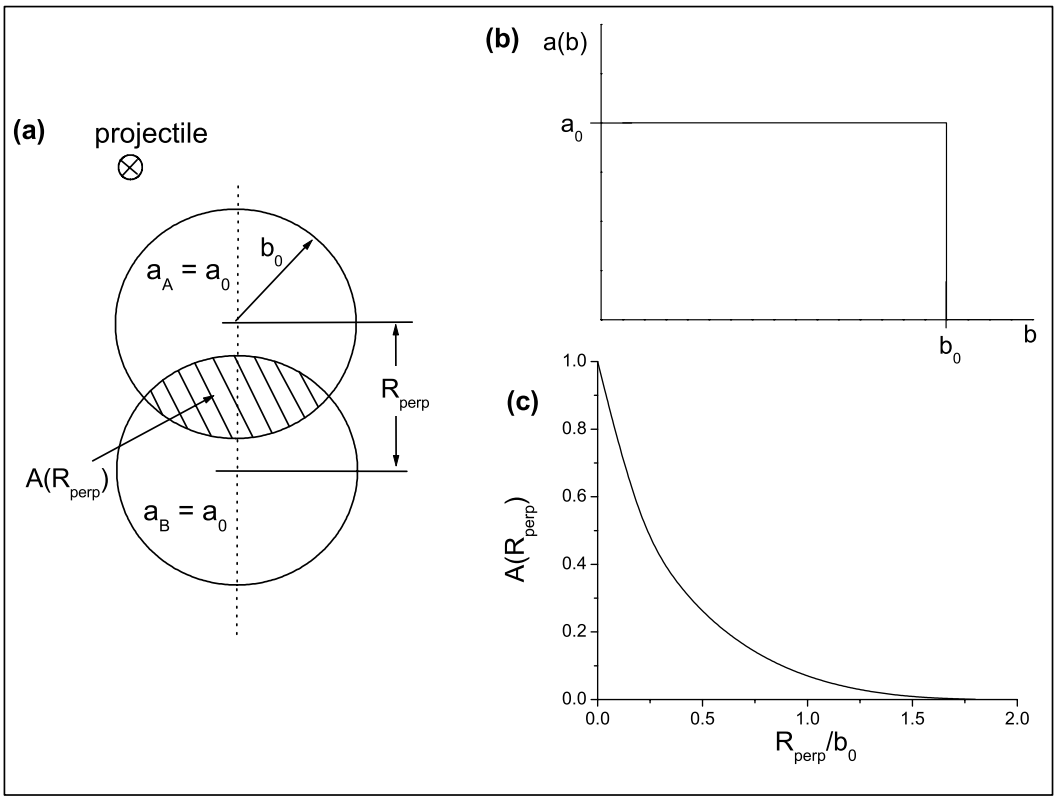

Figure 2.8: *Illustration of the alignment effect caused by the changing overlap of the geometrical cross section areas of the two molecular centers. (a) Schematic projection of the scattering amplitudes of each center onto the plane perpendicular to the projectile velocity. (b) Scattering amplitude used in this illustration. (c) Area of overlap of two disks $A(R_{perp})$ as a function of disk separation R_{perp}/b_0. b_0 is the disk radius.*

This effect causes the forward and backward peaking of the calculated alignment curves for the Ar^{2+}-H_2^+ and N^{2+}-H_2^+ collision systems. The atomic scattering amplitudes extend to large impact parameters b, larger than the internuclear separation R_0 of the deuterium molecular ion, such that the geometrical overlap is expected to

vary significantly as a function of alignment angle. In addition, the atomic scattering amplitudes vary rapidly as a function of b, as can be seen in the atomic probabilities in Fig. 2.5. Changing the alignment angle slightly shifts the atomic scattering amplitudes relative to each other. The oscillations can then cause "destructive interference", making the spatial overlap effect more pronounced. This can be observed in those two collision systems at alignment angles close to parallel alignment ($\theta = 0°$ or $180°$) in Fig. 2.7. The alignment dependence for these collision systems can not be caused by the phase factor Φ_0 as for the He^{2+} projectile, since it is constant and close to zero over the entire velocity range (see Fig. 2.6).

Chapter 3

Experimental Approach

3.1 Apparatus

The KSU ion-ion collision apparatus is a crossed-beam apparatus. It consists of two beamlines that intersect each other at an angle of 90°. The doubly-charged atomic beam, created in the ECR Ion source, is called the projectile beam. The molecular beam, created in a Penning Ion source, is called the target beam. This notation will help distinguishing the two beams throughout the following discussions. The reason for using D_2^+ as molecular ion target is because this ion has exactly the same mass-to-charge ratio as He^+, which is used when testing the performance of the appartus. For apparatus testing, resonant electron capture in collisions of He^+ with He^{2+} is measured, which requires only a two-particle coincidence setup to detect true ion-ion collision products. A detailed description of the apparatus is given in [36]. Here, a brief description of all the components is given, followed by a more detailed discussion of the components that were added to carry out the molecular ion - ion collision experiment. An overview of the complete apparatus is shown in fig. 3.1.

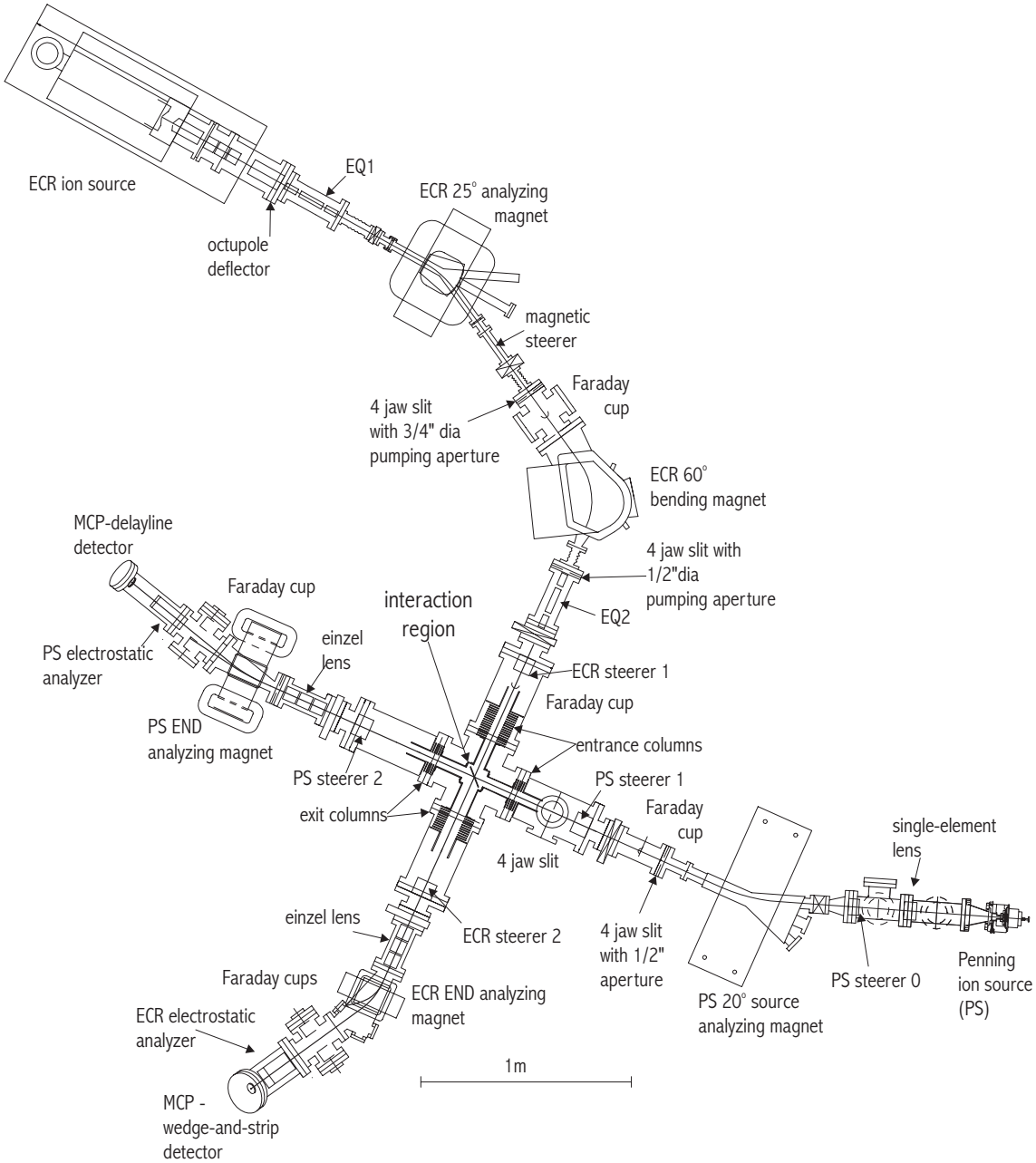

Figure 3.1: *The KSU ion-ion collision apparatus.*

3.1.1 Projectile Beam

The doubly charged projectiles are produced in a 4.5 GHz electron cyclotron resonance (ECR) ion source from a source gas. The source acceleration voltage is up to 18 kV. The extracted ions are momentum analyzed by a 25° magnet, and travel through a second 60° bending magnet before they enter the interaction region. Between the source and the analyzing magnet, as well as prior to the interaction region entrance, ions can be focussed by means of electric quadrupole triplets (EQ1 and EQ2). The beam's vertical and horizontal alignment can be adjusted with an octupole deflector immediately following the source, a magnetic steerer set between the two magnets, and a vertical electrostatic deflector (steerer 1) located between EQ2 and interaction region entrance.

The interaction region is held at a retarding potential, usually several kV, in order to energetically distinguish between rest gas collisions in the interaction region and elsewhere in the beamlines. In order to further reduce background events, the projectile beam is cleaned immediately before and after the beam intersection by a set of electrostatic analyzers (a detailed description is given in section 3.1.4).

Leaving the interaction region, the ion beam contains both parent and product ions, which are separated by an analyzing magnet located 1.5 m downstream the beam intersection. An einzel lens allows one to focus the ions at the magnet chamber entrance in order to avoid losses in the 5 cm gap. An electrostatic deflector (steerer 2) controls the vertical beam alignment. At the magnet chamber exit, the parent ion beam is collected in a Faraday cup. The product ions are further energy-analyzed in a 45° cylindrical electrostatic analyzer. This allows one to select charge exchange products from within the interaction region only. Those ions are detected on a position sensitive MCP detector. Their position and flight time is recorded. The timing signal

serves as reference (stop) of the triple coincidence and the position information is used in conjunction with the beam cleaner for background reduction.

3.1.2 Target Beam

The molecular D_2^+ target beam is produced in a Penning Ion Source (PS), which creates ions by electron impact from D_2 gas. Since the ionization process leads to a vertical Franck-Condon transition, the D_2^+ molecular ions are in a vibrationally excited state (sec. 1.6).

The ions extracted from the source are charge-state analyzed by a 20° magnet. Prior to the magnet chamber, a single element einzel lens focusses the beam. The vertical beam alignment is controlled by an electrostatic deflector located between the lens and the magnet chamber entrance. Following the magnet, two sets of four-jaw-slits 43 cm apart define the angular width of the beam. The beam enters the interaction region, where it travels through a beam cleaner identical to the one in the atomic beam (see 3.1.4 on page 43). In the present ion-ion collision experiments with a molecular ion beam, no voltage was applied to the cleaner plates, because the large-angle scattering of the ion-ion collision fragments (fig. 1.7 on page 15) is of the same order as the angular separation achieved by the beam cleaner. Similar to the atomic beam, the parent ion beam is separated from collision products by an analyzing magnet and collected in a Faraday cup. The reaction products are energy-analzyed in a 20° cylindrical electrostatic analyzer before being detected on a position sensitive multi-hit detector. The detector is located about two meters downstream from the interaction region. The positions and flight times of both molecular fragments are measured by using a micro channel plate detector in conjunction with a delay-line anode (described in sec. 3.2.1).

The imaging requirements to ensure proper collection of both molecular fragments

are described in detail in section 4.1 on page 66.

3.1.3 Interaction Region

Retarding Voltage

The interaction region is held at a retarding potential of 3.4 kV. Ions produced in collisions within the interaction region experience a net change in kinetic energy upon exiting the HV region, which allows their separation from ions produced in rest gas collisions along the beamline by means of an electrostatic analyzer. The ion beams enter and exit the interaction region through columns consisting of equally spaced ring electrodes. At the molecular beam exit, the column has been connected to ground, effectively creating a lens at the interaction region exit.

The Gate at the Beam Intersection

Fig. 3.2 shows the gate which is centered at the beam intersection, oriented at 45° with respect to both ion beams. This gate can be translated vertically by means of a 6 inch linear motion feedthrough, moving a number of elements in and out of the beam intersection:

- 2 mm dia aperture
- 1 mm slit
- beam cleaner
- molecular beam deflector

The 2 mm diameter aperture is used for beam tuning to ensure that the beam intersection is located at the center of the interaction region.

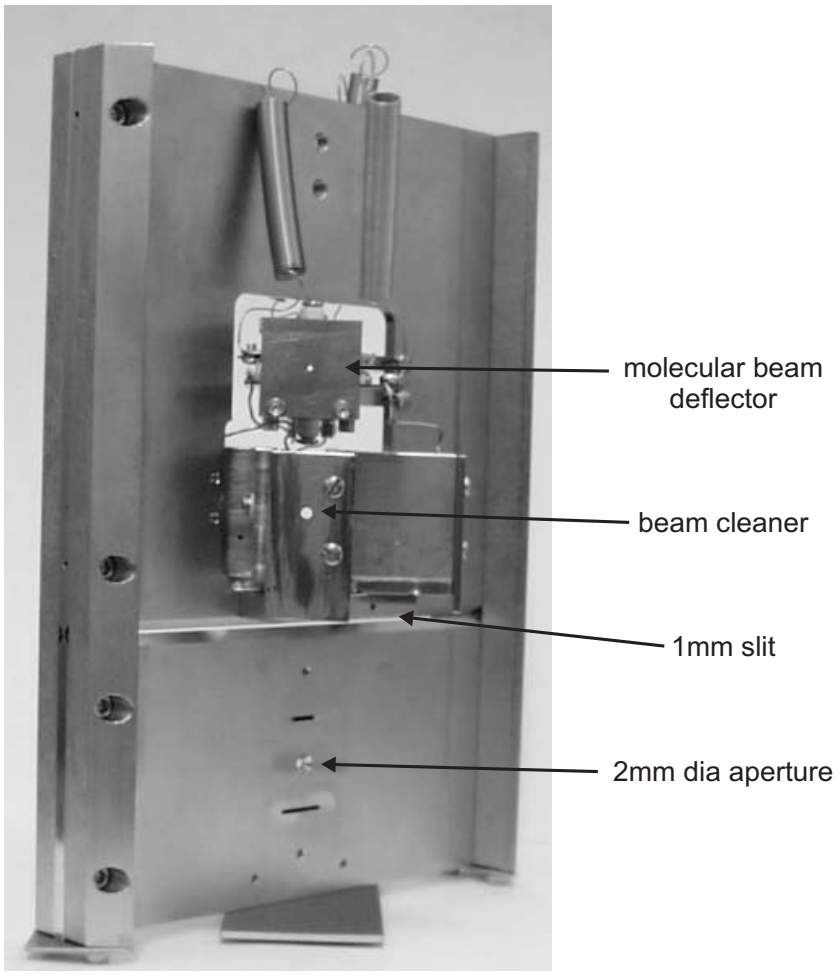

Figure 3.2: *The gate at the intersection region, as seen by the molecular ion coming from the PS ion source. The gate is mounted on a vertical translation stage.*

The central slit with a width of 1 mm, is used to evaluate the *form factor* $\mathcal{F}$, which measures the beam overlap:

$$\mathcal{F} = \frac{\int I_1 dz \cdot \int I_2 dz}{\int (I_1 \cdot I_2) dz} \tag{3.1}$$

where I_1 and I_2 are the beam currents in both beams. Alternatively, the experiments can be run with an aperture at the beam intersection; the form factor is then given by the height of the aperture.

The molecular beam deflector consists of two sets of vertical and horizontal plates, with a plate length of 2.54 cm and spaced by 0.51 cm. The centers of the two sets are located 1.52 cm before and after the beam intersection. This device allows one to deflect the molecular ion beam in a controlled manner in order to map out the target post-collision beamline.

This device is absolutely crucial, first of all to allow one to ensure experimentally that the angular acceptance of the apparatus is sufficient. It also plays an essential role in calibrating the detector position, which is done by sending a particle beam with well-defined energy through the deflector, and recording the beam position on the detector as a function of deflection voltage. This creates a map of the detector surface, relating positions to scattering angles, which can then be calibrated into transverse momentum (see sec. 5.4 on page 80).

3.1.4 Beam Cleaner

The purpose of the beamcleaner is to tag collision products with an angle that depends on the location of the collision along the ion's path. The beamcleaner separates collision products from three different regions:

- interaction region entrance to cleaner entrance (l = 17 cm)
- beam intersection region (l = 2 cm)
- cleaner exit to interaction region exit (l = 17 cm)

On the detector, collision products from those three region appear as distinct beam spots, which allows one to separate out background collisions.

The beamcleaner consists of a pair of electrostatic deflectors, arranged at equal distance before and after the beam intersection. The electric field vectors are antiparallel (Fig. 3.4). In the ECR beam, where reaction products have captured an

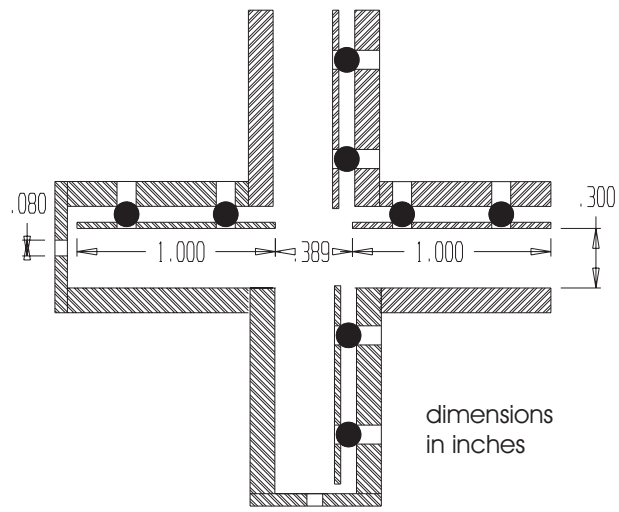

Figure 3.3: *Top view of the beam cleaner. The ECR beam is coming in from the bottom, the PS beam from the left. The two arms are identical.*

electron and decreased their charge state from two to one, the magnitude of the field in the exit deflector is twice that of the entrance deflector, such that reaction products created between the deflectors remain undeflected. Collision products from before or after the deflector set experience a net deflection, which results in separate beam spots on the detector two meters downstream from the cleaner. This effect is shown in a SIMION simulation of the beam cleaner (Fig. 3.4). The simulation first shows an ideal situation, where charge exchange only occurs in distinct regions (these are the three shaded regions in Fig. 3.4a). In this case one would observe three distinct beam spots.

In practice, charge exchange takes place throughout the entire cleaner, in particular also while the beam travels through the field region. (Fig. 3.4b). On the detector, one can only observe spots produced by charge exchange before or after the cleaner. The spot caused by charge exchange at the beam intersection will not be visible, unless a condition is set in the coincidence spectrum. This means in particular that it will not be visible while tuning beam. Once the beam spot that contains the true

ion-ion collision products has been identified, the background beam spots can then either be blocked with a beam block in front of the detector, or excluded by setting position gates in the data analysis software.

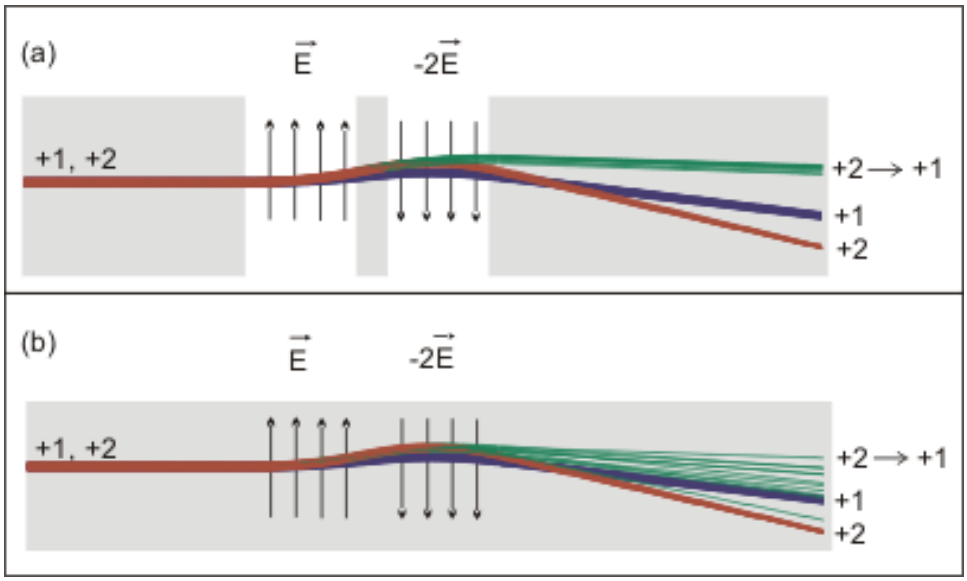

Figure 3.4: *Principle of a beam cleaner. The ion beam is travelling from left to right. It is initially doubly charged, but singly charged ions are created continously through electron capture from restgas in the shaded areas. In the top figure, no charge capture occurs while the beam is travelling through the field regions. In the bottom figure, charge capture occurs along the entire beam path. In the apparatus, the beam intersection is located between the two field regions. The detector would be to the right of the cleaner.*

To test the performance of the beam cleaner, resonant charge exchange in He^{+} + He^{2+} →He^{2+} + He^{+} collisions has been measured. The backgound reduction due to the cleaner is shown in Fig. 3.5. In this experiment, the cleaner has been used in both beams, as opposed the experiments with molecular targets, where the beamcleaner can only be used on the projectile beam. With a gate on the coincidence spectrum, the beam spot caused by charge exchange at the intersection region becomes visible in the position spectra. Comparing the coincidence spectra at the top and bottom of Fig. 3.5, the beam cleaner reduces the background by a factor of 100.

The position spectra show another interesting feature: In the ECR beam (projectile beam that captures an electron), the respective intensities of the background and the true ion-ion collision events are as expected from the varying interaction lengths (10 cm vs. 4 cm). In the PS beam, the He^{+} ions lose an electron, which, as a background channel, can only be accomplished through ionisation in a collision with a neutral restgas atom(molecule). The cross section for ionization in the keV range is very low and thus the intensities in the background beam spots are smaller than the intensity of the true beam spot, which predominantly contains charge exchange through the resonant capture by the He^{2+} ion beam.

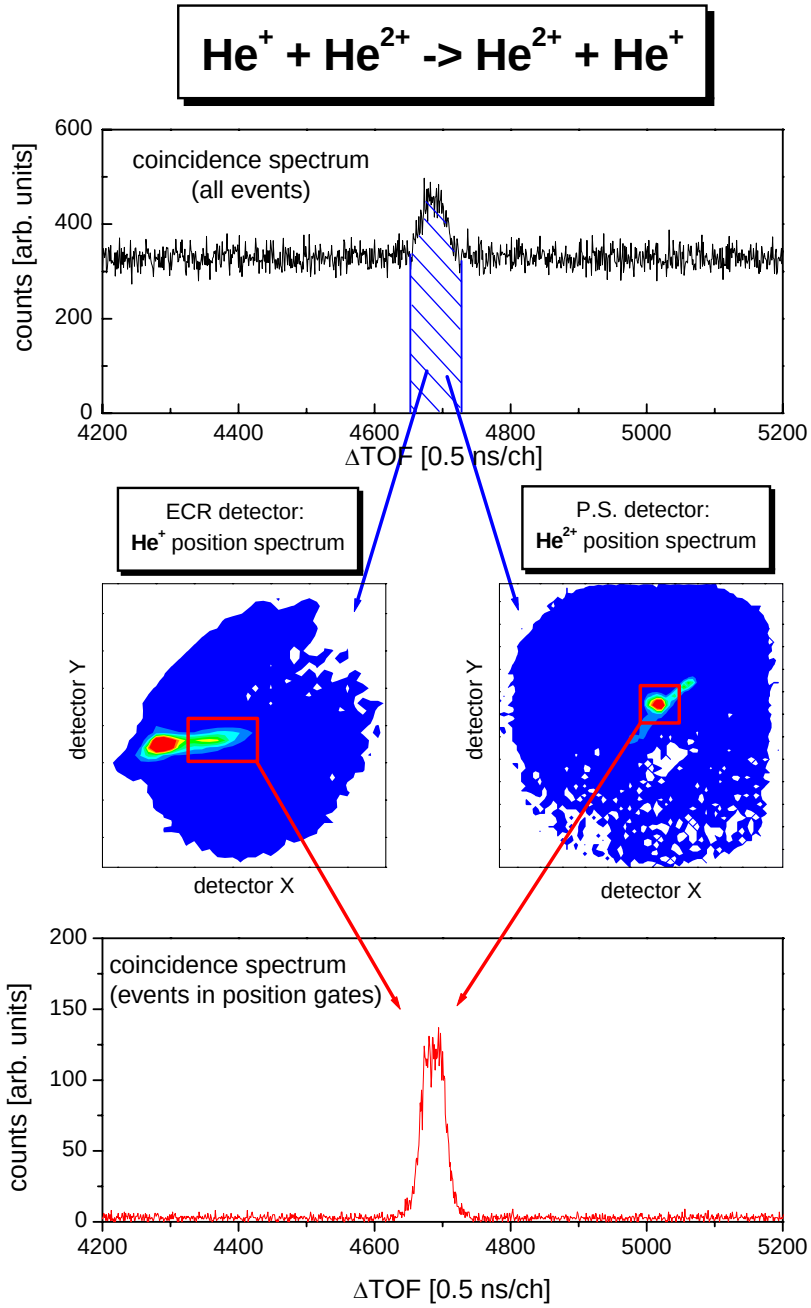

Figure 3.5: *Background reduction through use of the beam cleaner in He^{+} - He^{2+} collisions.*

3.2 Particle Detection

The collision products in both beamlines are detected with two-dimensional position sensitive detectors, which allow recording both time and position of each impacting particle. The detectors consist of two microchannel plates (MCP) in chevron configuration followed by a wedge-and-strip (W&S)-anode (projectile detector) or a delay-line (DL) anode (target detector). The advantage of using a delay-line detector for detection of the molecular fragments is the multi-hit capability of the delay-line anode. The double-hit resolution of this detector is limited by the pulse-pair resolution of the NIM-electronics, which is about 10 ns here. This means that two hits arriving within 10 ns will appear as one single pulse. Fig. 3.6 shows the DL-detector assembly with MCP and delay-line anode. For a description of MCP detectors with W&S anodes see [37] and references therein. The MCP-DL-detector will be described in some detail in the following.

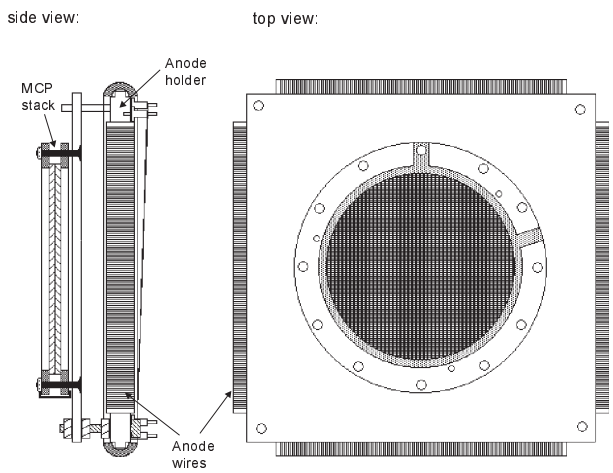

Figure 3.6: *Side- and top view of a delay-line detector with microchannel plates. In our setup, the diameter of the microchannel plates is 50 mm.*

3.2.1 Multi-Hit Detector

MCP-signal

When a keV ion impacts on to a microchannel plate surface, secondary electrons are created and multiplied in the microchannels. The electron shower then exits the back of the MCP stack and is accelerated towards the anode, which is held at a positive potential with respect to the back MCP. The replenishing of the MCP charge through an external voltage source gives rise to an electronic pulse which can be used to determine the time of ion impact. A more detailed description of MCP operation can be found in [38].

In the configuration used in this setup, two channelplates in Chevron configuration are spaced by a 1 mm stainless steel ring. The timing signal is taken from this center ring through the signal-pick-up-box shown in Fig. 3.7. This device has the advantage of providing an adjustable impedance through the potentiometer, which helps to minimize reflections of the fast timing signal due to impedance mismatch. After amplification by an Ortec VT120B fast preamplifier, the signal amplitude is about 2 V and the signal rise time is 3.5 ns. The noise level is less than 300 mV.

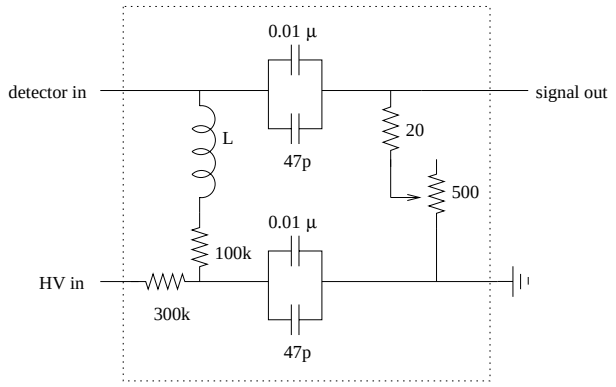

Figure 3.7: *Filterbox used to pick up the timing signal from the MCPs. The voltage rating of the capacitors needs to be in accordance with the voltage applied at the HV input.*

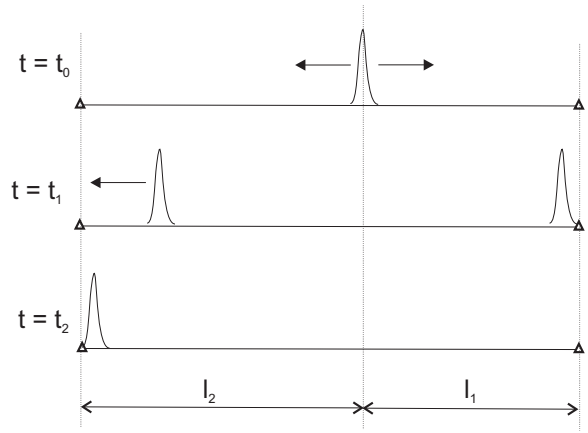

Figure 3.8: *Snapshots of a signal propagating in a delay line. Time moves downward.* **t=t$_0$:** *the pulse is induced in the line.* **t=t$_1$:** *the signal reaches the end of the closer right end of the delay line.* **t=t$_2$:** *the signal reaches the further, left end of the delay line.*

Delay-Line Principle

The delay experienced by an electronic signal travelling along a line depends on the length of the cable. This effect can be used to determine the location of a lightning strike to a power line. Here, this effect is used to determine the position of a particle impacting a MCP-detector, as illustrated in Fig. 3.8. The electron shower, created by the particle impact, exits the MCP stack and induces an electric pulse in the delay-line at $t = t_0$. This pulse then propagates in both directions and towards the ends of the wire. It arrives at each end after a time $t_i = l_i/v \quad i = 1, 2$ relative to t_0. The labels 1,2 stand for the two ends, l_i is the distance on the wire the signal has to travel to reach either end and v is the signal's propagation speed. In order to obtain position information in two dimensions, two sets of delay-lines perpendicular to each other (x,y) are used. t_{x1} and t_{x2} denote the signal propagation time to the ends of the wire along the x-direction, t_{y1} and t_{y2} along the y-direction.

Position Reconstruction

The particle's horizontal (x) and vertical (y) positions are proportional to the difference

$$x_j = x_{cal} * (t_{x1j} - t_{x2j}) \tag{3.2}$$

$$y_j = y_{cal} * (t_{y1j} - t_{y2j}) \tag{3.3}$$

where $x_j = 0$, $y_j = 0$ are located at the midpoint of each wire. The label j denotes the j-th hit. The calibration constants x_{cal}, y_{cal} are usually determined in a proper calibration procedure (e.g. a mask for position calibration, or see section 5.4 for our calibration procedure).

Adding the times it takes the signal from both ends of one delay line gives the *time-sum* constant $T\Sigma$

$$T\Sigma_{x,j} = t_{x1j} + t_{x2j} \tag{3.4}$$

$$T\Sigma_{y,j} = t_{y1j} + t_{y2j} \tag{3.5}$$

For clarity, $t_0 = 0$ is assumed here. In our multi-hit setup, the MCP timing signal is used to give the time reference t_0. The time-sum in x and y is a constant for a given detector setup, since it depends only on cable lengths. The distribution of sum signals from our delay-line anode has a FWHM of 2 ns. Setting a gate on the sum provides a means to choose events for which all five signals (flight time and four position signals) were recorded.

Delay-Line Anode Design

The MCP stack is followed by the delay-line anode, which consists of wires wound around the anode holder. The anode holder is made of stainless steel with ceramic guides at the edges. There are two layers of wires perpendicular to each other to

input (9PIN)		output (LEMO)
signal in	diff. in	signal out
9 (X_1^S)	5 (X_1^D)	1
8 (X_2^S)	4 (X_2^D)	2
7 (Y_1^S)	3 (Y_1^D)	3
6 (Y_2^S)	2 (Y_2^D)	4

Table 3.1: *EDL DLA800 differential amplifier in- and output connections. Input #1 is connected to ground. In brackets are the detector output connections.*

measure positions in two dimensions. Each layer consists of two parallel wires, called the signal wire and the difference wire. The signal wire is held at a more positive potential than the difference wire, attracting the electron cloud exiting the back of the last MCP. Electronic noise is picked up by both the signal and the difference wires. In a differential amplifier (EDL DLA800), the signals on the difference wire are subtracted from those on the signal wire, eliminating electronic noise induced in the wires. This requires in turn that the signal- and difference wires are kept close to each other to ensure that they pick up the same electric noise. The in- and output channels of the differential amplifier are listed in Table 3.1. Eight inputs are provided for the signal and difference wire outputs fromthe four corners of the delay-line anode. The EDL DLA800 output signals have a rise time of 8.5 ns, with an amplitude of 250 - 500 mV. The voltages used to operate the MCP-DL-detector are shown in Table 3.2.

3.2.2 Beam Viewer

Sometimes it is useful to be able to see the detector image on-site, e.g. while tuning beam, instead of having to go to a computer screen. With a simple electronics scheme as shown in Fig. 3.9, the positions can be 'calculated' in hardware and displayed on an oscilloscope in XY-mode. The idea is to use a time-to-amplitude converter (TAC) to

MCP-DL-detector	Voltage[V]
front MCP	-1800
center ring	-900
back MCP	0
anode holder	+75
difference wire	+75
signal wire	+115

Table 3.2: *Operating voltages of the MCP-DL detector for keV ion detection.*

obtain the time-difference required in Eq. (3.2). Each TAC is started with the MCP timing signal, and stopped with one of the x- and y- timing signals. (In principle, the position is proportional to either time-difference of a pair out of t_1, t_2 or t_{MCP}, as can be seen by combining Equations (3.2) and (3.4). For best resolution, t_1 and t_2 are used.) For the 50 mm diameter channelplate-detector used here, the TAC range is 100ns and the stop-signals are delayed by 20ns to position the detector image into the first quadrant.

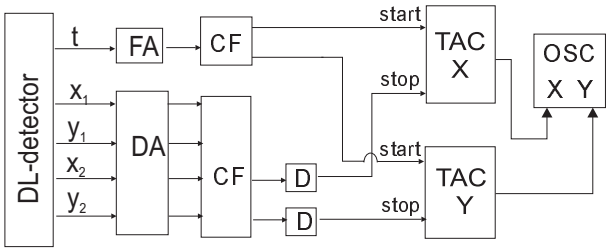

Figure 3.9: *Electronics scheme used to display the image acquired with a delay-line detector on an oscilloscope in XY-mode. DA: Differential Amplifier; FA: Fast Timing Amplifier; CF: Constant Fraction Discriminator; D: Delay.*

3.3 Electronics Scheme and Data Acquisition

In this experiment, the rates on the detector are much higher than the the actual true event rate. This requires implementing a coincidence scheme such that a strobe is generated only if events have the signature of a true ion-ion collision, namely the detection of two molecular fragments in coincidence with a charge-changed projectile ion. This triple coincidence scheme is shown in Fig. 3.10, and explained in more detail in the following section.

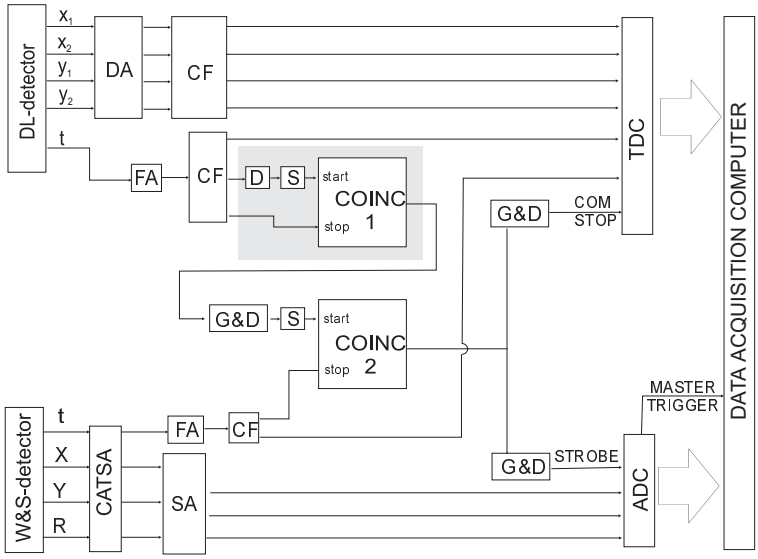

Figure 3.10: *Triple-coincidence scheme. DA: Differential Amplifier; FA: Fast Timing Amplifier; CF: Constant Fraction Discriminator; CATSA: Charge And Time Sensitive Amplifier; SA: Spectral Amplifier; D: Delay; S: Stretcher; D&G: Gate and Delay Generator. A timing diagram for the shaded area is shown in fig. 3.11.*

3.3.1 Coincidence Scheme

An ion-ion collision event is identified by detecting the charge-changed projectile and two charged molecular fragments in coincidence. Since the two fragments impact on the same detector, a self-coincidence setup is required to make a coincidence between

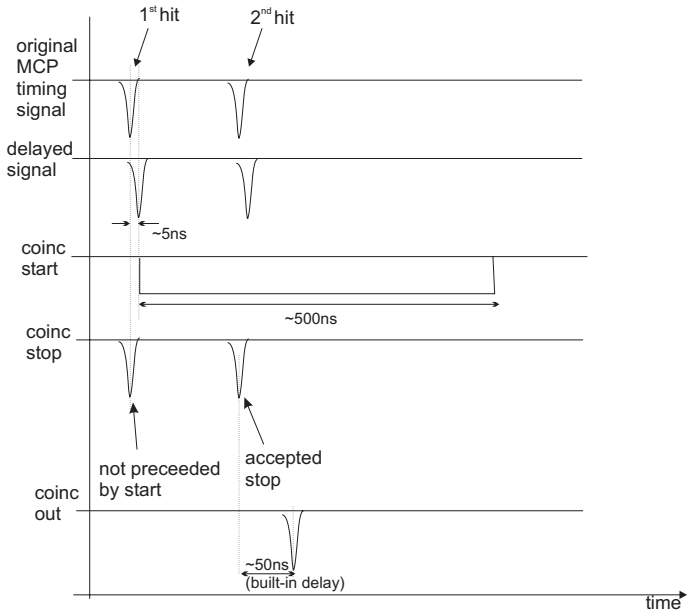

Figure 3.11: *Self-coincidence timing scheme.*

two signals travelling on the same line. The self-coincidence setup relies on accepting a signal as valid stop only if it has been preceeded by a valid start within the selected time range. To obtain a coincidence on two consecutive signals travelling on one line, the line is split in two. The stop signal is fed directly into the coincidence unit. The signal to be used as start is delayed by at least the signal rise time. This ensures that by the time the first event starts the coincidence unit, this same event has already passed by the stop input and the coincidence is stopped by the second event. In our setup an overlay coincidence unit (EG&G CO4010) is used. The use of this unit has the advantage that the coincidence window is chosen through the width of the start signal. In this setup, the start signal is stretched to 500 ns. The timing diagram of this setup is shown in Fig. 3.11.

The resulting coincidence signal is used to start the second coincidence between the two molecular fragments and the charge-changed projectile. Again, the start is delayed and stretched (usually to 2 μs) to give the proper coincidence window, and

the stop is provided by the timing signal of the projectile detector. The resulting triple-coincidence signal is then used to strobe the ADC, which triggers the CAMAC-LAM signal (LAM stands for "look at me" and enables the data to be transfered to the computer.) An advantage of this setup is that the strobe is in-phase with the projectile detector timing signal, as well as the projectile detector position signals, which makes it easier to ensure that the correlated W&S position signals are within the strobe window.

3.3.2 Data Acquisition

This triple-coincidence scheme is used only to generate a strobe. The coincidence spectra are created in software from the TDC outputs. The timing signals from the two detectors as well as the position signals from the delay-line anode are fed into six channels of a TDC (LeCroy3377), a multi-hit TDC that accepts up to 16 hits per channel with a resolution of 0.5 ns and a maximum range of 32 μs. The three position signals from the Wedge-and-Strip anode are fed into an ADC (Ortec811). The TDC and ADC are operated in master-slave mode with the ADC as master, triggering the CAMAC-LAM signal, since the ADC conversion time of 70 μs is much longer than that of the TDC (few μs). The data is stored in list mode, such that it can be analyzed further offline. The program files used for offline sorting are listed in apppendix E.

3.3.3 Second Hit Resorting Algorithm

In this experiment, flight time and position of both molecular fragments need to be measured in order to obtain the three-dimensional Coulomb-sphere. In our apparatus, the MCP-detector efficiency has been determined to be 40% [36]. For triple hit, this results in a overall efficiency of 6.4 % just for the timing signal. In addition, 2×four

TΣ H1	TΣ H2	resort	rel. counts
-	-	-	1.0
X	X	-	0.33
X	X	X	0.56

Table 3.3: *Comparison of event rates with and without using the resorting algorithm. The event rates are normalized to the rate when no time-sum conditions are applied. TΣ H1 and TΣ H2 are the time-sum condition (Eq. 3.4) for both x and y of the first and second hit respectively.*

position signals have to be read. This decreases the detector efficiency by another 40 % when operating the delay-line detector in multi-hit mode. The resulting overall efficiency is then 3.8 %.

Our setup is particularly sensitive to the detection efficiency of the position signals of the second hit. Requiring the time-sum condition TΣ, Eq. (3.4), of the second hit positions to be satisfied, reduces the total detection efficiency further (see table 3.3). This is caused by ringing in the signal lines, which may preceed the second hit position signal in any of the four lines.

To recover second hit position signals that have been preceeded by noise, a resorting algorithm, which is shown in a flow diagram in Fig. 3.12, has been implemented. In case the time-sum condition TΣ of one of the second hit position is not satisfied, the algorithm searches for a permutation of the K-th and L-th hit in the two ends (K$\geq$ 2 and $L \geq 2$) which do satisfy the time-sum condition. The depth to which this search extends is a parameter. For our data, the true second hit was found within the third through fifth hit in the event buffer. The effect of applying the resorting algorithm to a dataset is shown in Table 3.3.

So-called *entangled* hits, for which the first and second hit positions are interchanged, are not recovered through this algorithm. Such events can occur when the time difference between two hits is shorter than the "length" of the anode wires,

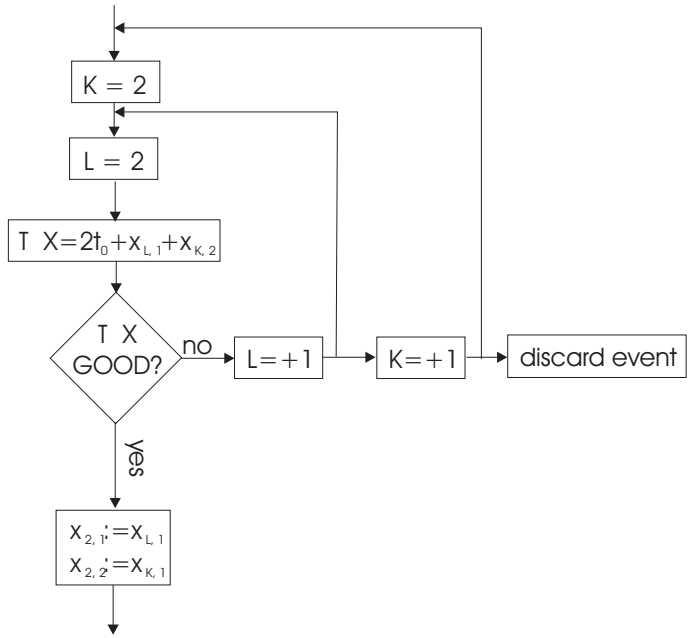

Figure 3.12: *Algorithm used to recover second hit position signals, shown here for position signals on the two ends of the x-signal line. The first index specifies the hit number (1 through 16), the second index specifies the signal line end (1 or 2). A parameter, not shown in this flow diagram, specifies the depth of the search (or how many times the loops are repeated).*

which is the time it takes a signal to travel from one end of the anode to the other end. This effect causes the pulse-pair resolution gap not to have parallel edges, but rather sloped edges with the smallest separation at the center of the detector. The slope is unity.

3.4 Event Rates

In this section, event rates are calculated for ion-ion collision events, as well as for background events created through collisions with the rest gas constituents. It will be shown that a triple coincidence condition is necessary to distinguish the true ion-ion collision events from background events. First, the reactions that result in particles that are detected on the channelplate detectors need to be identified. Only particles

with the correct momentum-to-charge and energy-to-charge ratios are selected by the magnetostatic and electrostatic analyzers to follow trajectories leading to the detector. Electron capture as a result of an ion-ion collision by design results in particles that are detected, but so do some of the collisions between ions and rest gas constituents. In the second step, coincidence rates are calculated.

3.4.1 Ion-Ion Collisions

The reaction studied throughout these experiments is electron capture from a molecular ion by a doubly charged projectile ion:

$$X^{2+} + D_2^+ \rightarrow X^+ + D^+ + D^+ \qquad\qquad X = N, Ar, He \tag{3.6}$$

This process is identified by detection of the two molecular fragments in coincidence with the charge-changed projectile. The final state is unique, it is the only reaction channel that leads to the production of three positive ions.

The molecular ion's initial vibrational state remains undetermined, as well as the final state of the X^+ ion. The ion-ion collision capture rate, R^c_{ion}, is

$$R^c_{ion} = \sigma^c \cdot \frac{I_1}{q_1} \cdot \frac{I_2}{q_2} \cdot \frac{v_{rel}}{v_1 v_2} \cdot \frac{1}{\mathcal{F}} \tag{3.7}$$

where σ^c is the total capture cross section, $I_{1(2)}$, $q_{1(2)}$ and $v_{1(2)}$ are current, charge state and velocity of each ion beam, v_{rel} is the relative velocity of the ion beams and $\mathcal{F}$ is the form factor. For its definition, see Eq. (3.1). Table 3.4 summarizes the rates for electron capture in collisions between 1.6 keV D_2^+ ions with the various projeciles used in the experiment. Detector efficiencies are not yet taken into account. Also shown are the true rates as observed in the experiment, which are lower than the calculated rates by a factor of 20 - 50. This drop is caused by the detector efficiency, it indicates an overall detector efficiency of about 7%. Since three particles need to be

projectile	E_{proj} [keV]	v_{rel} [a.u.]	σ^c_{ion} 10^{-16}cm^2	rate(theory) [Hz]	rate(expt) [Hz]
Ar^{2+}	5.2	0.19	7.4	5.2	0.093
N^{2+}	7.2	0.23	3.8	1.8	0.11
He^{2+}	14.2	0.42	0.72	0.27	0.022
He^{2+}	23.2	0.51	1.5	0.52	0.039

Table 3.4: *Total cross section (taken from sec. 2.3), relative collision velocity and capture rate for electron capture in collisions between 3.1 keV D_2^+ with He^{2+}, Ar^{2+} and N^{2+}. E_{proj} is the energy of the atomic beam inside the interaction region. The beam currents are 20 nA for the molecular beam and 50 nA for the atomic beam. The form factor is 2 mm. Detector efficiencies are not included in the theoretical rates. The true rate as observed in the experiment is shown as well.*

detected for a true ion-ion collision event, this translates to a single particle efficiency of each MCP detector of 41%, which is what the detectors have been characterized for earlier [36]. The rates shown in the table are for beam currents of 20 nA in the molecular ion beam and 50 nA in the atomic ion beam, typical values.

3.4.2 Rest Gas Collisions

Even though the rest gas pressure is kept in the low 10^{-10} torr range, the rest gas density is comparable to the ion beam densities. Due to the longer pathlength, which is about two orders of magnitude larger than the beam diameters, the background (BG) collision rate is by orders of magnitude larger than the true ion-ion collision rate. In the following, event rates and coincidence rates for the $N^{2+} + D_2^+$ collision system are calculated. The rates obtained are similar for the other projectiles used in the experiment.

From the ideal gas law, the rest gas density corresponding to a certain pressure is $n_{BG} = 3.5\ 10^6 \#/cm^3/10^{-10}$ torr. The rest gas collision rate is determined through

$$R_{N^+} = \sigma_{BG} \cdot n_{BG} \cdot \frac{I}{q} \cdot l \cdot \epsilon \tag{3.8}$$

where σ_{BG} is the capture cross section for the particular background (BG) production channel, I, q are beam current and charge state, l is the path length over which the beam interacts with the rest gas, here given by the length of the interaction region (l=38 cm). ϵ is the efficiency of the MCP-detectors, taken to be 40%. The BG rate depends on the particular ion only through the total cross section, it is independent of ion velocity. The BG production channels for each beam are discussed below.

Atomic Ion Beam

Any projectile ion that captures an electron from a rest gas atom or molecule in the interaction region is detected on the MCP-detector.

$$N^{2+} + X \rightarrow N^{+} + X^{+} \tag{3.9}$$

At a rest gas pressure of $3 \cdot 10^{-10}$ torr, the capture rate for a beam current of $I_{at} =$ 50 nA is

$$R^{c}_{BG} = 12.4 \text{ kHz} \tag{3.10}$$

with $\sigma^{c}_{BG} = 5 \cdot 10^{-16}$ cm^2. For all projectiles used in the experiment, the absolute capture cross section is of this order [39, 40]. The rate observed on the detector can be reduced by about an order of magnitude by using the beam cleaner (see section 3.1.4).

Molecular Ion Beam

Any collision within the interaction region that leads to the dissociation of a molecular ion into a charged and uncharged fragment will result in one deuterium ion that is detected. This can occur either in rest gas collisions, or in slit scattering when the molecular beam passes through an aperture:

$$D_2^{+} + X \rightarrow D^{+} + D + X^{*} \tag{3.11}$$

With the same rest gas density as used for the atomic beam calculation, the dissociation rate observed on the detector for a beam current of $I_{mol} = 20$ nA is

$$R^d_{BG} = 10 \text{ kHz} \tag{3.12}$$

with $\sigma^d_{BG} = 5 \cdot 10^{-16}$ cm^2 [41].

3.4.3 Coincidence Rates

True Coincidences The true coincidence rate is given by the ion-ion collision capture rate, multiplied by the detector efficiencies ϵ. With detector efficiencies of 40%, the expected true rate is

$$\begin{aligned} R_{true} &= R^c_{ion} \cdot \epsilon_{proj} \cdot \epsilon^2_{mol} \\ &= 0.11 \text{ Hz} . \end{aligned} \tag{3.13}$$

Accidental coincidences The particles contributing to the accidental coincidences are mainly produced in three independent events. The contribution of correlated particles is neglected in the following.

In a two-particle coincidence setup, the rate of accidental coincidences is

$$\begin{aligned} R^{(2)}_{acc} &= R_{N^+} \cdot R_{D^+} \cdot \delta t \\ &= 250 \text{ Hz} . \end{aligned} \tag{3.14}$$

The time coincidence window δt was set to be 2 μs. In order to reduce this rate, a second molecular fragment was required within $\delta t' = 500$ ns. This reduces the accidental coincidence rate to

$$\begin{aligned} R^{(3)}_{acc} &= R^{(2)}_{acc} \cdot R_{D^+} \cdot \delta t' \\ &= 1.3 \text{ Hz} . \end{aligned} \tag{3.15}$$

This number corresponds to the total event rate of the experiment, since in these experiments, the true event rate is neglible compared to the background. In order to evaluate the feasibility of the experiment, the rate of accidental coincidences within the width of the true coincidence peak needs to be compared to the true event rate. Looking at the time-of-flight difference between the charge-changed projectile ion and the center-of-mass of the molecular fragments, the width of the coincidence peak is about $\delta t''$ =30 ns (see Fig. 3.13(c)). The rate of accidental coincidences within $\delta t''$ is then

$$\begin{aligned} R_{acc} &= R_{acc}^{(3)} * \frac{\delta t''}{\delta t + \delta t'/2} \\ &= 0.019 \text{ Hz} . \end{aligned} \tag{3.16}$$

This is smaller than the true rate, so a coincidence peak should become visible in the spectrum for those conditions. Table 3.5 shows the coincidence rates as observed in the experiment. The accidental coincidence rates are calculated from the singles rates on the detector. The true-to-random ratio of the experimental data is further improved by setting tight gates around the true beam spot on the projectile detector, where the beam cleaner (see sec. 3.1.4) was used.

The resulting coincidence spectra for N^{2+}+D_2^+ collisions are shown in Fig. 3.13. The top two spectra, Fig. 3.13(a) and 3.13(b), are coincidence spectra between the N^+ projectile and the first (a) and second (b) molecular fragment. Due to the large variation of laboratory energy, the molecular fragments are spread over a wide range of time, here about 100 ns. The bottom spectrum, (c), shows the coincidence spectrum between the N^+ projectile and the center-of-mass of the molecular ion, whose flight-time is $(t_1 - t_2)/2$. The coincidence peak is much narrower, determined mainly by the width of the overlapping ion beams.

Table 3.6 summarizes the the total number of counts used for further data analysis

projectile	X^+ rate [kHz]	D^+ rate [kHz]	R_{acc} (in 30 ns) [Hz]	R_{true}(expt) [Hz]	R_{true}(theory) [Hz]
Ar^{2+}	11	28	0.11	0.093	0.31
N^{2+}	10	27	0.10	0.11	0.11
He^{2+}(v=0.4 a.u.)	12.5	38	0.18	0.022	0.016
He^{2+}(v=0.5 a.u.)	8	38	0.11	0.039	0.031
calculated	12.4	10	0.019		

Table 3.5: *Measured rates in collisions of D_2^+ with He^{2+}, Ar^{2+} and N^{2+}. X^+ is the associated charge changed projectile. The current of the molecular beam is 20 nA. The projectile beam currents are 50 nA. The last row summarizes the rates calculated in section 3.4.2. The same BG capture cross section is assumed for all projectiles. The last column shows the theoretical rates from table 3.4, multiplied by the total detector efficiency of 7%.*

projectile	$\frac{\text{real}}{\text{random}}$	total cts analyzed	running time [s]
Ar^{2+}	2.5	57500	4.25E5 (5 days)
N^{2+}	1.6	23100	3.2E5 (4 days)
He^{2+}(v=0.4 a.u.)	0.4	23700	76E4 (9 days)
He^{2+}(v=0.5 a.u.)	0.4	56200	6E5 (7 days)

Table 3.6: *Summary of the statistics of the four data sets: real-to-random ratio, total number of counts used in the analysis and total running time for each collision system.*

for each collision system. Those numbers are not normalized to the same beam currents. Since every system was run under different conditions. In both He^{2+} runs, the ECR beam current was about 100 nA, whereas it was on average about 50 nA when using N^{2+} and Ar^{2+} projectiles. The molecular beam current was kept around 30 nA in all runs. The real-to-random ratio is much smaller for both He^{2+} runs, which is due to the much smaller cross section, and also caused by the higher background rate. Using He as source gas elevated the rest gas pressure in the interaction region somewhat. On the other hand, the beam cleaner seemed to be most effective on the He^{2+} beam.

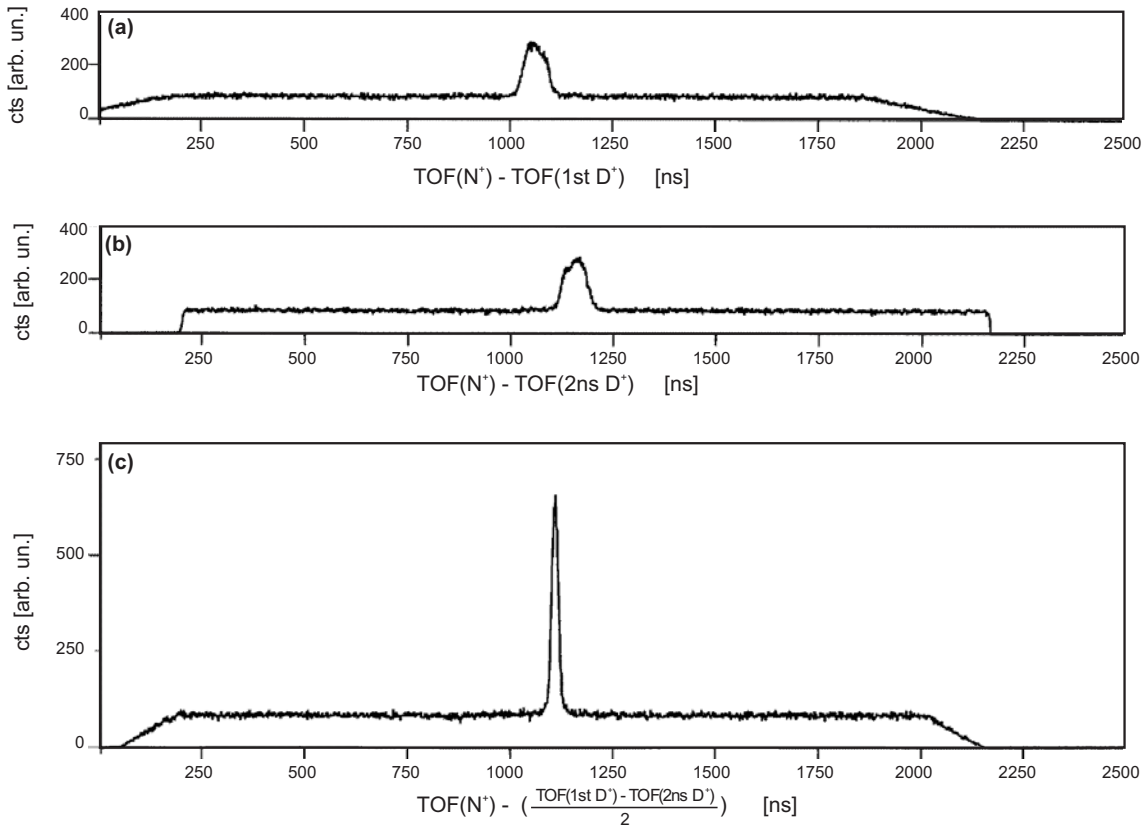

Figure 3.13: *Coincidence spectra in $N^{2+}+D_2^+$ collisions. The histograms have been taken at 0.5ns/ch. The running time was 321465 s. Beam currents were $I_{D_2^+} = 35nA$, $I_{N^{2+}} = 54nA$.*

Chapter 4

Ion Trajectory Simulations

4.1 Fragment Imaging

In this experiment, it is not only important to collect all the molecular fragments on the position sensitive detector, it is also necessary to retain the information on the alignment of the molecular axis at the time of the collision. This is done by arranging the ion optics (see Fig. 4.1) such that all fragments which emerge from the collision do hit the detector, and do so in such a way that fragments with the same velocity vector are observed in one spot on the detector, independent of where the Coulomb-explosion took place within the collision volume. The condition for this so-called *velocity map imaging* [42] is to have the collision center in the focus of the first lens, which creates a parallel beam at the exit of this lens, and to have the detector at twice the focal length of the second lens. The optical analog of such a lens system is shown in Fig. 4.1(a) A SIMION simulation of the ion optics of the electrostatic components of our actual apparatus is shown in Fig. 4.1(b). In an ion optical lens, the focal length depends on the ratio of beam energy to lens voltage. This restricts the range of retarding voltage, since the velocity mapping condition needs to be satisfied, but also the beam velocity has to be such that the maximum fragment angle in the laboratory frame is well below $\arctan(2d/l)$, where d is the electrode inner diameter,

and l is the distance between collision point and electrode entrance (see fig. 1.7 on page 15).

The magnification M of this system is $M = \tan(\gamma_2)/\tan(\gamma_1) = f_1/f_2$.

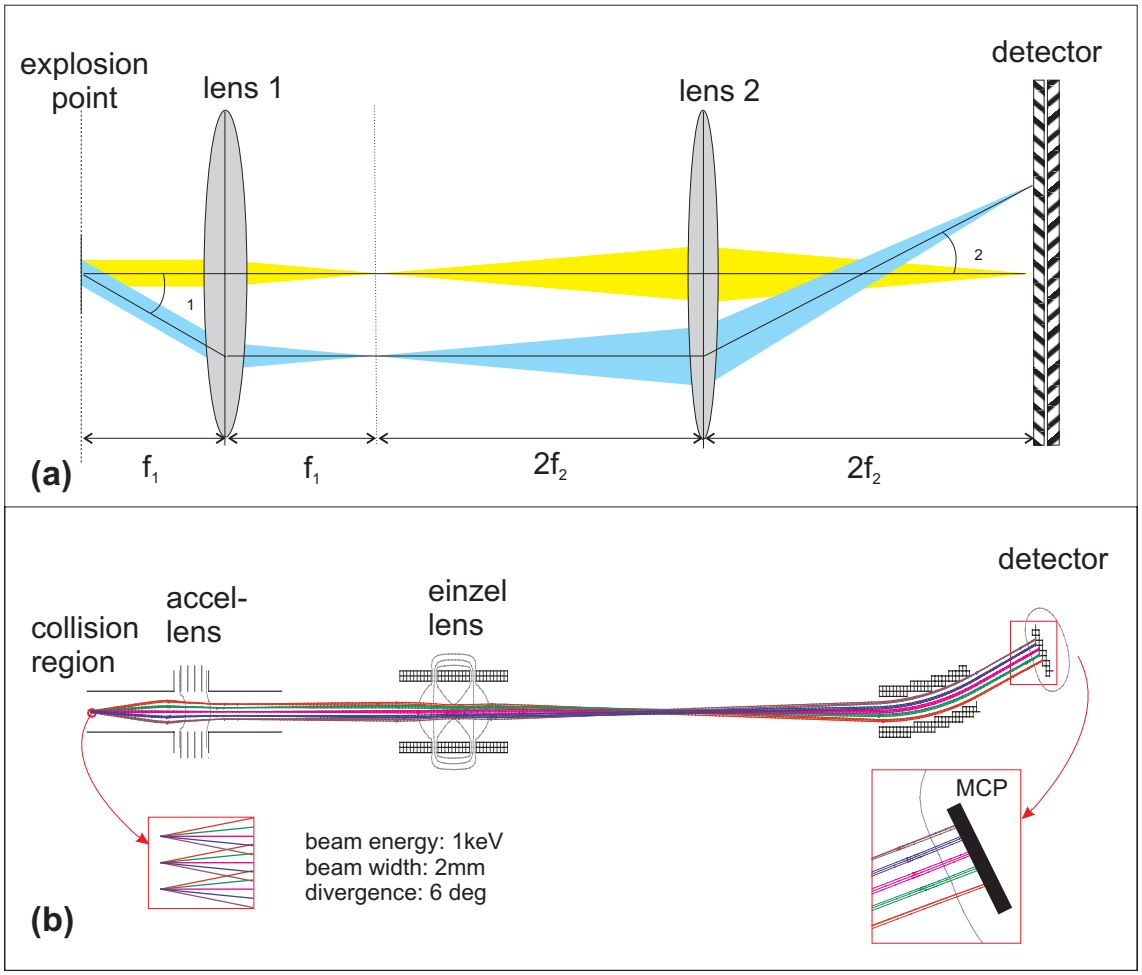

Figure 4.1: *Velocity mapping in geometrical optics (a) and in a SIMION ion trajectory simulation (b).*

While the principle shown in Fig. 4.1(a) was approximately used, the details of the actual experimental arrangement are somewhat different and more complex as is shown in Fig. 4.1(b), which does not include the magnetic analyzer. The effects of both the electric and magnetic analyzing fields onto the Coulomb-sphere are discussed

in appendix D and the results are summarized below.

4.2 Imaging of a Coulomb-sphere through Magnetic and Electric Analyzers

The purpose of the magnetic and electric analyzers is to separate ions which have different energy per charge ratios. Overall, these analyzers allow separation of product ions from the parent ion beam in the magnetic analyzer, and separation of collision products created in the interaction region from those created elsewhere in the beam lines. But the analyzers also affect the true molecular fragments, and these effects need to be understood in order to interpret the raw data:
Consider fragments of a Coulomb-exploded molecule that was aligned along the molecular ion beam. In the laboratory frame, the energies of the forward- and backward emitted fragments differ by as much as 400 eV, for a mean fragment energy of 1.55 keV and a Coulomb-energy of $E_{coul} = 6\ eV$ (see sec. 1.5.3 on page 14). Those two fragments travel along different trajectories through the analyzers, and consequently do not impact at the same point of the detector surface.

A general discussion of the distortions of a Coulomb-sphere traveling through magnetic and electric field is presented in appendix D. The conclusions of that section are in summary:

Magnetic Analyzer

The distortions introduced by the magnetic analyzer depend on the direction of the Coulomb-sphere velocity vector relative to the molecular ion beam and magnetic field direction. The Coulomb-sphere velocity $\vec{v}_{CS}$ is the velocity of the molecular fragments with respect to their center-of-mass, as defined in Equation (1.6) on page 13. For fragments traveling along the beam, $\vec{v}_{CS}$ is parallel to the molecular ion beam

direction $\vec{v}_{targ}$. After passing the magnetic field, these two vectors are at an angle, and the absolute value of $|\vec{v}_{CS}|$ changed. In contrast, for fragments ejected in the breakup of molecular ions aligned perpendicular to the beam and perpendicular to the magnetic field direction, $\vec{v}_{CS}$ is perpendicular to the beam direction and remains so after passing the magnetic field. Any velocity vectors parallel to the magnetic field lines are not affected, since then the vector product is zero. (See also Fig. D.1 on page 131.)

Electrostatic Analyzer

A Coulomb-sphere traveling through an electric field is not subject to any distortions in a short range after exiting the field (see Fig. D.3 on page 136). In our apparatus, the fragments are detected within this range. Since the main beam got deflected, the entire Coulomb-sphere is now rotated with respect to the beam direction, in the plane defined by the beam direction and the electric field vector. Fragments whose Coulomb-sphere velocity vectors are perpendicular to the field are not affected.

Chapter 5

Data Analysis

5.1 Introduction

The data reduction involves several steps. At first, the random events need to be subtracted to obtain spectra of the true ion-ion collision events only, which is done in section 5.2. In the resulting raw data spectra, the Coulomb-sphere appears distorted, which is caused by the ion optical lenses and the magnetic and electrostatic analyzers that the molecular fragments pass prior to arriving at the detector. In section 5.3, the results from a SIMION ion trajectory simulation are used to parameterize and quantify the distortions introduced by each ion optical element. An equation is derived which relates the measured quantities to the undistorted Coulomb-sphere. Based on this equation, a reconstruction scheme is devised in section 5.6, through which the distortions observed in the raw data are reversed.

Section 5.4 explains how the measured detector positions are related to the corresponding scattering angle in the collision. This is done *in situ* by recording the position of a D^+ ion beam for a given deflection angle in the interaction region. In section 5.5, the calibration factor to convert this deflection angle into transverse momentum is derived from first principles. Also a calibration factor to convert time-of-flight difference into longitudinal momentum is derived.

All experimental data shown in this chapter is from measurement of $N^{2+} + D_2^+$ collisions. The simulated Coulomb-sphere is obtained from a SIMION simulation, which includes all the ion optical elements between the beam intersection and the detector, namely the two lenses as well as the magneto static and the electrostatic analyzers. Throughout this chapter, only the shape of the Coulomb-sphere is of relevance. The distribution within the sphere is subject of chapter 6.

5.2 Background Subtraction

In the time window of the true coincidences, up to 50% of the events are background collision products (depending on the collision system). In order to obtain distributions of the molecular fragment on the delay-line detector, this background needs to be subtracted. A typical coincidence spectrum is shown in Fig. 5.1. Three windows are set on this spectrum: One window includes the time-peak, containing true as well as random events. Two windows are set symmetrically to the left and right of the peak, containing only random events. Spectra are calculated from data within each window. As an example, position spectra of the first hit are shown here. Pure background spectra, created from data within gates to the left and right of the coincidence peak (spec(II) in Fig. 5.1), are subtracted from the spectra containing data within the peak window only (spec(I) in Fig. 5.1). The background spectra need to be scaled, since those windows include more random events than the peak window, just because the windows are larger (to improve the statistics). For this scaling, a linear background is assumed.

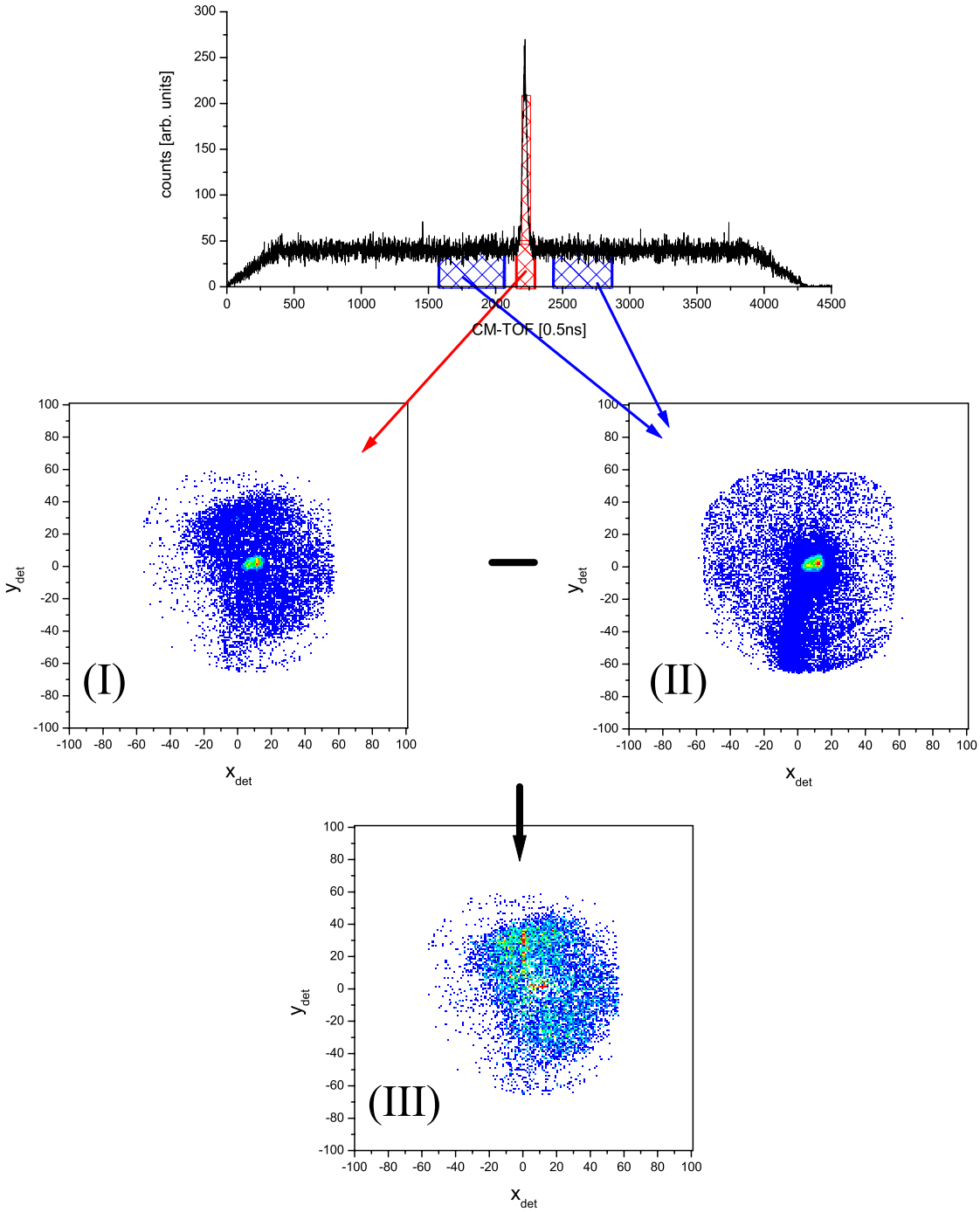

Figure 5.1: *Coincidence spectra in N^{2+}-D_2^+-collisions. The three gates which are used in the background subtraction are: I, trues plus randoms; II, randoms; III, trues only.*

The resulting spectrum shows the first fragment position of the true events only (spec(III) in Fig. 5.1). As expected, the true molecular fragments are spread over a large fraction of the detector surface, as a result of the relatively large energy release in the Coulomb-explosion. The random events are caused by dissociation of molecular ions, with a small energy release, thus the position distribution is very narrow.

5.2.1 The Raw Position and Time-of-Flight Spectra

Fig. 5.2 shows the two-dimensional position spectra of the first and second hit. The spot created by the random events is visible as a white spot close to the center of each distribution. It can be noticed that the positions of the first and second hits are not distributed equally with respect to the position of the random events, which is the same in both spectra. Also the intensity distributions are different for the two, although they seem to be mirror images of each other.

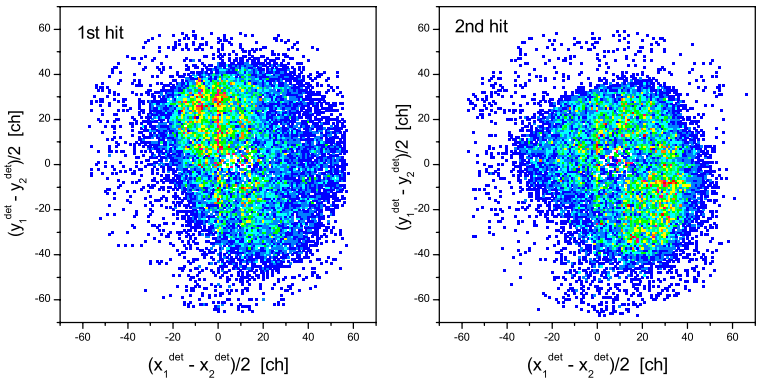

Figure 5.2: D_2^+ - N^{2+} *experimental data: The position spectra of the first and second hit. Background is subtracted.*

Using the first and second hit positions and flight times, a raw image of the Coulomb-sphere can be obtained through

$$x_{cs} = \frac{x_1^{det} - x_2^{det}}{2} \tag{5.1}$$

$$y_{cs} = \frac{y_1^{det} - y_2^{det}}{2} \tag{5.2}$$

$$z_{cs} = \frac{t_1 - t_2}{2} \tag{5.3}$$

where x_i^{det} and y_i^{det} are the first and second hit positions (i=1,2) and t_i is the flight time associated with each hit. Projections of the resulting Coulomb-sphere are shown in Fig. 5.3. Background is subtracted. The gaps in the projections (b) and (c) are caused by the limited pulse-pair resolution of the detector system: Fragments impacting on the detector within less than 10 ns are not detected. Note that, by definition, z_{cs} is negative. In these spectra positive values of z_{cs} are generated by reversing t_1 and t_2 in Eq. (5.3). The corresponding positions are created by exchanging first and second hit in Eqns. (5.1) and (5.2).

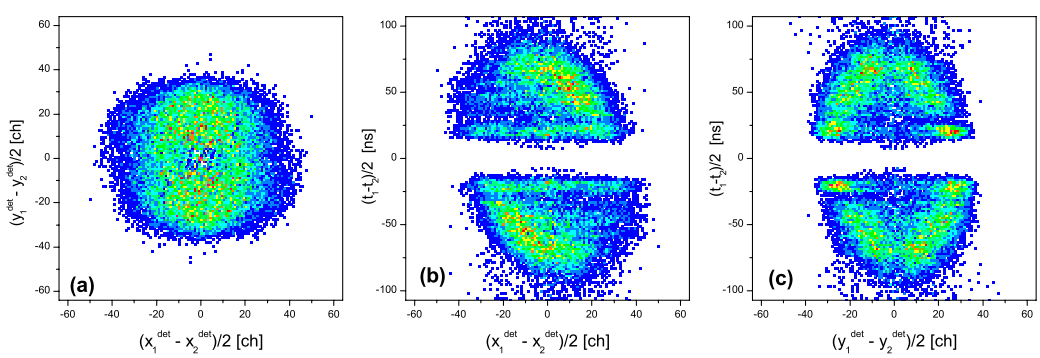

Figure 5.3: D_2^+ - N^{2+} *experimental data: The Coulomb-sphere as observed on the detector. (a): Projection onto the* (x^{det}, y^{det}) *plane. (b): Projection onto the* (x^{det}, TOF) *plane. (c): Projection onto the* (y^{det}, TOF) *plane. TOF is the time-of-flight direction.*

The shape of the Coulomb-sphere is not as circular as one might expected. In

particular the projections onto planes involving the time-of-flight directions appear to be of slight elliptic shape. These features are caused by the ion optics elements in the apparatus: The molecular fragments are projected onto the detector by two electrostatic imaging lenses, which introduces distortions to the image. Furthermore, they pass a magnetic and an electrostatic analyzer. Those effects are investigated and quantified in the following section, and a reconstruction scheme is devised.

5.3 The Coulomb-Sphere in the Detector Frame

In the ion-ion collision apparatus, a magnetic analyzer is used to separate product ions from the parent ion beam, and from the product ions, an electrostatic analyzer energy-selects ions created within the collision region. Thus, when the molecular fragments arrive at the detector, they have passed both analyzers. Fragments ejected forward and backward along the molecular ion beam, which travel along the beam direction at different speeds, are now impacting at different positions on the detector surface. The Coulomb-sphere as it is observed in detector coordinates $[(\vec{x_1}, t_1)^{det} - (\vec{x_2}, t_2)^{det}]$ is not simply proportional to the velocity-space Coulomb-sphere $(\vec{v})^{lab}_{cs}$ produced in the collision (Fig. 5.4).

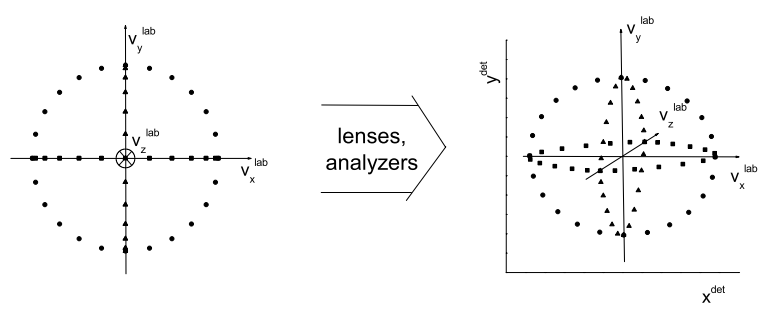

Figure 5.4: *Simulated slices (from SIMION) of a Coulomb-sphere at different times:* left: *as emerging from the collision in the* $(\vec{v})^{lab}_{cs}$ *frame;* right: *as viewed in detector coordinates* $(\vec{x}, t)^{det}$*, after passing the lenses and analyzers. In both cases, the molecular ion beam direction is into the page.*

In order to compare to the experiment more directly, the trajectories of the molecular fragments through the apparatus have been simulated with SIMION. This simulation includes the two imaging lenses and the magnetic and electrostatic analyzers. The field lines of both the magnetic analyzer and electrostatic analyzer are in the vertical $(\hat{y}^{lab}, \hat{z}^{lab})$-plane. Instead of simulating molecular fragments from molecules aligned randomly about the beam intersection, molecular fragments distributed on rings with $v_{cs,k} = 0$, k=x,y,z along the lab frame unit vector directions, are chosen. One of the ring lies in the plane perpendicular to the beam direction, the other two lie in a horizontal or vertical plane containing the ion beam direction. The three rings start out at the collision center and travel through the lens arrangement as well as the two analyzers. The Coulomb-energy per fragment is $E_{coul} = 6$ eV. For each ion hitting the detector surface, position and flight time is recorded, analogous to the experiment. Fig. 5.5 shows projections of slices of the simulated Coulomb-sphere. The three frames in the figure are

(a) the projection onto the detector surface (x^{det}, y^{det})

(b) the projection onto the (x^{det}, t) plane, spanned by the detector x-position and flight time

(c) the projection onto the (y^{det}, t) plane, spanned by the detector y-position and flight time.

In the first frame, the projection of the slice perpendicular to the beam (with $v_{cs,z} = 0$) has a slight elliptic shape, which is an indication that the $v_{cs,x}$ and $v_{cs,y}$ axes did not get tilted by the same amounts. The last two frames, Figs. 5.5(b) and (c), show clearly that fragments ejected forward and backward along the beam axis at different laboratory energies arrive at different locations on the detector surface. The shape of

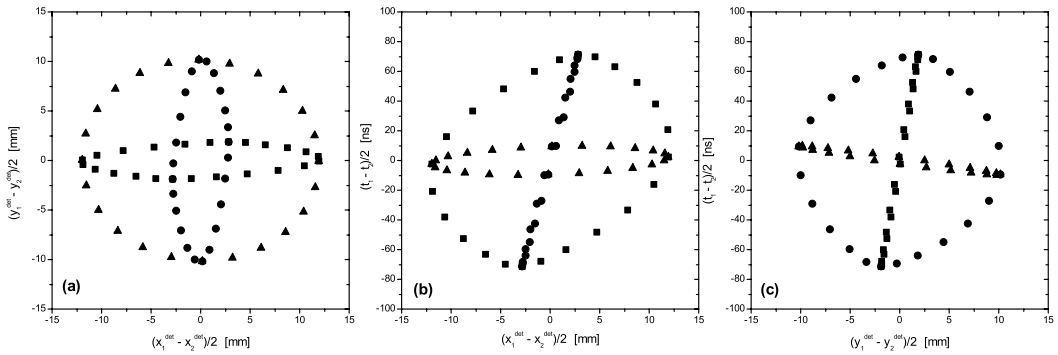

Figure 5.5: *Simulation result: Projections of molecular fragments impacting on a two-dimensional detector surface. The fragments emerge from the collision distributed on rings. Triangles:* $v_{cs,x} = 0$*; Squares:* $v_{cs,y} = 0$*; Circles:* $v_{cs,z} = 0$*.*

the Coulomb-sphere slices in the last two frames reminds more of a square than of a circle. This is caused by the distortions due to the imaging lenses. The distortions are non-linear and create a pin-cushion image. The general features of a Coulomb-sphere traveling through a magnetic or an electric field have been investigated in appendix D. The characteristics obtained are used to quantify the distortions caused by the analyzers.

The effect of each element is parametrized in the following. The order of the elements is as encountered by a beam traveling towards the detector. Prior to passing any distorting element, the velocity components of the Coulomb-sphere in the laboratory frame are proportional to the respective space coordinates and time-of-flight through $\mathbf{v}_{cs} = (v_x, v_y, v_z) \propto (x_1 - x_2, y_1 - y_2, t_1 - t_2))$.

- The **imaging lenses** introduce distortions by affecting each ion's trajectory. The distortions occur predominantly in the plane perpendicular to the beam direction:

$$v'_x = f(v_x, v_y) \tag{5.4}$$

$$v'_y = g(v_x, v_y) \tag{5.5}$$

$$v'_z = v_z \tag{5.6}$$

The dependence of the distortions on v_z is negligible within the Coulomb-sphere laboratory energy variations.

- The effect of the **magnetic analyzer** onto the Coulomb-sphere is to disperse ions which are not traveling at the same speed in the horizontal plane, which is equivalent to skewing the molecular axis parallel to the beam, $v_{cs,z}$. The molecular axes perpendicular to the beam direction remain perpendicular to the beam after passing the analyzer.

$$v''_x = av'_x + bv'_z \tag{5.7}$$

$$v''_y = v'_y \tag{5.8}$$

$$v''_z \approx v'_z \tag{5.9}$$

- The **electrostatic analyzer** rotates the entire Coulomb-sphere in the vertical plane. The axes of the Coulomb-sphere remain approximately orthogonal to each other, but not to the beam direction. To account for an imperfect rotation, two angles, δ and ϵ characterize the twist of each axis.

$$v'''_x = v''_x \tag{5.10}$$

$$v'''_y = \cos(\delta)v''_y + \sin(\delta)v''_z \tag{5.11}$$

$$v'''_z = \cos(\epsilon)v''_z - \sin(\epsilon)v''_y \ . \tag{5.12}$$

Combining the three sets of equation gives

$$v'''_x = af(v_x, v_y) + bv_z \tag{5.13}$$

$$v'''_y = \cos(\delta)g(v_x, v_y) + \sin(\delta)v_z \tag{5.14}$$

$$v'''_z = \cos(\epsilon)v_z - \sin(\epsilon)g(v_x, v_y) \ . \tag{5.15}$$

Apart from calibration factors, this is equivalent to the measured data, $(v'''_x, v'''_y, v'''_z) \propto (x_1^{det} - x_2^{det}, y_1^{det} - y_2^{det}, t_1 - t_2)$.

The analyzer effects can be observed in the simulation: The second frame, Fig. 5.5(b), is mostly affected by the magnetic analyzer. The $v_{cs,z}$ axis is clearly not along the beam direction (the beam direction is along the time-of-flight axis). The $v_{cs,x}$ is along the x^{det} direction, as expected. The last frame, (c), is mostly affected by the electrostatic analyzer. Both axes are still at right angles to each other, approximately, but they are rotated with respect to the time-of-flight direction. For both analyzers, the rotation or skewing angles are small.

The reconstruction of the initial Coulomb-sphere from the measured data amounts to reversing the skewing and distortions introduced by the ion optics and the analyzers. In mathematical terms, Eqns. (5.13)-(5.15) need to be inverted to find the initial velocity components of the Coulomb-sphere (v_x, v_y, v_z) from the the measured quantities (x^{det}, y^{det}, t). The parameterization equations involve several types of parameters:

- the angles, δ and ϵ, and b, by which the axes are skewed(slanted). They will be determined from the simulation and applied to the data.

- the mapping function (f, g) which describes the distortions introduced by the imaging lenses. The mapping function will be determined *in situ* by mapping out the apparatus with a D^+ ion beam. The mapping procedure is described in sec. 5.4.

- the calibration factors c_{pos} and c_t which are used to convert scattering angle (or detector position) and flight time into units of momentum, are derived sec. 5.5 from first principles.

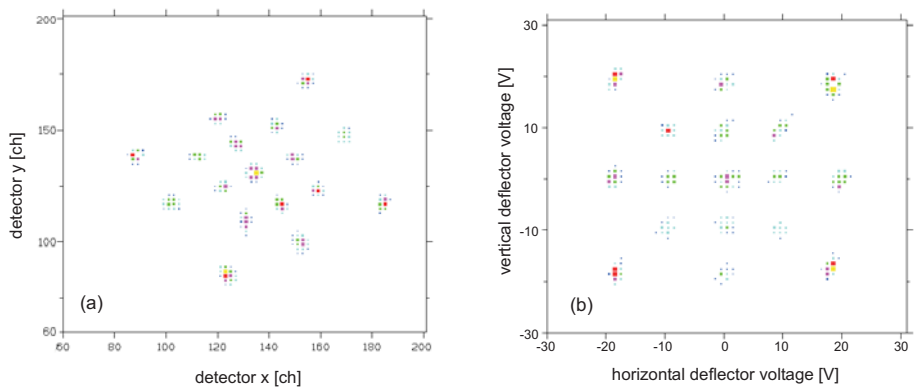

Figure 5.6: *Detector image, obtained by deflecting a 1.55 keV D^+ beam in the collision region in a regular checkerboard pattern. (a) Raw image. (b) Image corrected for lens aberrations and converted into units of deflector voltage.*

5.4 Mapping Properties and Lens Distortions

The mapping properties of the lens arrangement are investigated in situ by deflecting a D^+ beam with a set of electrostatic deflectors (see section 3.1.3) located at the center of the collision region. This is effectively a D^+ source with well-defined beam energy and scattering angle, originating at the beam intersection. The impact position of this beam on the delay-line detector is recorded as a function of deflector voltage, creating a map of the detector surface. Such a map is shown in Fig. 5.6a. It relates detector position to scattering angle at the beam intersection, which is ultimately converted into transverse momentum.

The raw image, Fig. 5.6a, is clearly distorted by the lenses. This raw detector image also shows that the detector is actually rotated by 27° with respect to the vertical and horizontal laboratory planes. The distortion as well as the rotation are corrected for by fitting the measured data (x^{map}, y^{map}) to the initial, regular voltage

pattern u_x, u_y:

$$u_x = \sum_k a_k \Phi_k(x^{map}, y^{map}) \tag{5.16}$$

$$u_y = \sum_k b_k \Phi_k(x^{map}, y^{map}) \tag{5.17}$$

The coefficients (a_k, b_k) are obtained through a 2d-linear least-squares fit as derived appendix B. The basis functions $\Phi_k(x, y)$ are polynomials in x and y up to third order and include terms mixed in x and y. The result of this fit is shown in Fig. 5.6b. The image is corrected and the positions are given in units of deflector voltage, which is proportional to the angle of the beam, or, the transverse momentum of the molecular fragments.

This image is not sensitive to the initial beam energy, therefore, one set of fitting parameters is used to convert fragment position into deflector voltage or momentum. The absolute location of the center of the checkerboard pattern however does depend on the beam energy. Before being able to apply the position map, the dependence of absolute beam position on beam energy has to be removed. This will the first step when reconstructing the initial Coulomb-sphere from the measured data in section 5.6. Position maps are created for each set of run, after beam tuning has changed. The position maps used to convert detector positions, as well as the fit coefficients derived from each map, are listed in appendix C.

5.4.1 Deflector Offset

To deflect the test-molecular ion beam at the beam intersection, a set of vertical and horizontal deflectors are mounted at the center of the collision region. For design reasons, the two deflectors are located slightly before and after the exact center (they are shifted by ±16 mm each).

The effect of this arrangement is studied in a SIMION-simulation. Fig. 5.7 shows

the detector image created by ions deflected by the same amount, but originating *at*, *before*, or *after* the collision region center.

The image created by ions whose origin was before the collision point is largest, whereas the image created by the ions originating from after the collision point is smallest. By scaling the horizontal and vertical positions with a common *scaling factor s* (open circles), the images can be brought to overlap with the image of those ions which originated from exactly the collision region center.

$$x_{sc} = x/s \qquad\qquad y_{sc} = y \cdot s \tag{5.18}$$

x and y are horizontal and vertical detector positions.

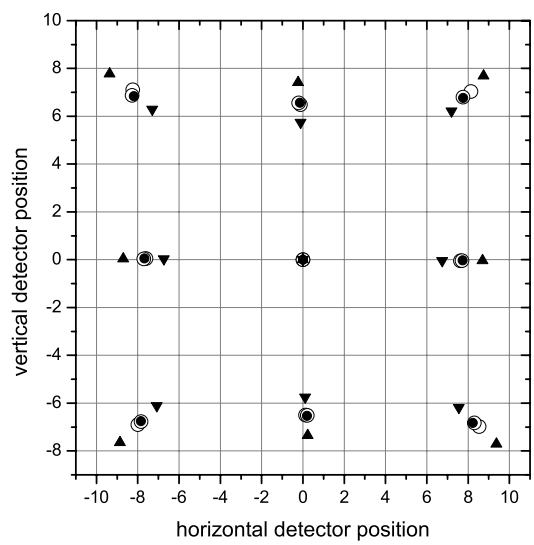

Figure 5.7: *Ions deflected by the same amount, but originating from different locations along the beam axis. The images are created by ions whose origin is located at (solid circles), before (up triangles), or after (down triangles) the collision region center. The images are brought to overlap using a scaling factor of 0.88 (open circles).*

5.5 Calibration Factors

5.5.1 Time Calibration

The flight time of a molecular fragment is proportional to the z-component of the fragment's momentum, p_z. To derive the calibration factor, consider molecular fragments that exploded along the molecular beam direction only. v_z is the longitudinal component of the velocity acquired by the fragment in the Coulomb explosion in the molecular frame, the potential energy released in the explosion is E_c. E_b (v_b) is the energy (velocity) of the molecular fragments inside the collision region, which is held at high voltage. This first region has an extension of l_{in}.

When the fragments exit the collision region, they are accelerated towards ground potential, resulting in an energy gain of $E_R = qV_R$. The distance the particles travel in this region until they reach the detector is l_{out}.

The first and second fragment's flight time to the detector is

$$t_1 = \frac{l_{in}}{v_b + v_z} + \frac{l_{out}}{\sqrt{\frac{2}{m}E_R + (v_b + v_z)^2}} \tag{5.19}$$

$$t_2 = \frac{l_{in}}{v_b - v_z} + \frac{l_{out}}{\sqrt{\frac{2}{m}E_R + (v_b - v_z)^2}} \tag{5.20}$$

The first term can be written as

$$\frac{1}{v_b \pm v_z} \approx \frac{v_b \mp v_z}{v_b^2} \tag{5.21}$$

since $\mathrm{E}_b = 1550$ eV and $\mathrm{E}_c = 6$ eV. Call $E_{out} = E_R + E_b$, the beam energy outside the collision region. With $(mv_bv_z) \ll E_{out}$ the square root can be expanded into

$$\frac{1}{\sqrt{\frac{2}{m}E_R + (v_b + v_z)^2}} \approx \frac{1}{\sqrt{\frac{2}{m}E_{out}}} \cdot (1 - \frac{mv_bv_z}{2E_{out}}) \tag{5.22}$$

The flight time difference between the first and second fragment is then

$$t_1 - t_2 = \frac{-2l_{in}v_z}{v_b^2} - \frac{l_{out}}{\sqrt{\frac{2}{m}E_{out}}} \cdot \frac{mv_b v_z}{E_{out}} \tag{5.23}$$

$$= -\frac{l_{in}\, p_z}{E_b} - \sqrt{\frac{E_b}{E_{out}}} \cdot \frac{l_{out}\, p_z}{E_{out}} \tag{5.24}$$

where p_z is the longitudinal component of the momentum given to the fragment in the Coulomb explosion. The time calibration factor $c_t = p_z/\Delta t$ is then

$$c_t = -\left(\frac{l_{in}}{E_b} + \sqrt{\frac{E_b}{E_{out}}} \cdot \frac{l_{out}}{E_{out}}\right)^{-1} \tag{5.25}$$

With $E_{out} = 4.95$ keV, $E_b = 1.55$ keV, $l_{in} = 17$ cm and $l_{out} = 1.6$ m one obtains

$$c_t = -(0.68 + 1.13)^{-1} \cdot 10^{-24} \text{ [kg m/s/ns]} \tag{5.26}$$

$$= -0.55 \cdot 10^{-24} \text{ [kg/m/s /ns]} \tag{5.27}$$

$$= -0.28 \text{ [a.u./ns] (with 1 a.u. } = 2 \cdot 10^{-24}\text{kg m/s)} \tag{5.28}$$

5.5.2 Position Calibration

After applying the mapping function to the data, the positions will be given in units of volts, corresponding to the voltage applied to the deflector plates. One then needs a calibration factor that converts this voltage into atomic units of transverse momentum.

If a beam of energy E_b travels trough a deflector with a voltage difference U_{pl} applied to the plates, it will be deflected by an angle

$$\tan(\theta) = \frac{U_{pl}}{2E_b}\frac{l}{d} \tag{5.29}$$

In terms of beam velocity components, the scattering angle ψ is also given by

$$\tan(\psi) = \frac{v_c \sin(\alpha)}{v_b + v_c \cos(\alpha)} \simeq \frac{v_c \sin(\alpha)}{v_b} \tag{5.30}$$

since the beam velocity v_b is much larger than the velocity v_c acquired in the Coulomb explosion. As in Eq. (1.10), α is the angle between molecular axis and beam direction, such that $mv_c \sin(\alpha)$ is the transverse momentum $p_\perp$. Combining these two equations, the transverse momentum as a function of plate voltage is

$$p_\perp = \frac{qU_{pl}}{2E_b}\frac{l}{d}p_b \tag{5.31}$$

For the deflector geometry used here, l/d = 5. The conversion factor c_{pos} with $p_\perp = c_{pos} \cdot U_{pl}$ is, for a 1.55 keV D^+-beam with $p_b = 647$ a.u. :

$$c_{pos} = 1.04[\text{ a.u./V}] \tag{5.32}$$

In the actual calibration, c_{pos}=1.425 a.u./V is used, because that is the value which makes the data round. The calibration thus relies on the time calibration factor c_t which is more accurate.

5.6 Reconstruction Scheme

Within the reconstruction algorithm, Eqns. (5.13)-(5.15) are inverted. The equations are derived in sections 5.6.1 through 5.6.3. The algorithm is summarized in Fig. 5.8, where it is applied to the experimental as well as the simulated "data".

5.6.1 Axis Corrections

The first step in the reconstruction of the initial Coulomb-sphere is to reverse the analyzer effects, which make the position at which a molecular fragment hits the detector dependent not only on the transverse velocity components v_x and v_y, but also on the longitudinal velocity component v_z. Inserting v_z from Eq. (5.15) into Eqns. (5.13) and (5.14) and neglecting terms containing products of $\sin(\epsilon) * \sin(\delta)$

and $b * \sin(\epsilon)$ since the angles δ and ϵ are small, and b is small, one obtains

$$\begin{aligned} a v'_x &= v'''_x - b v_z \\ &\approx v'''_x - \frac{b}{\cos(\epsilon)} v'''_z \end{aligned} \tag{5.33}$$

$$\begin{aligned} \cos(\delta) v'_y &= v'''_y - \sin(\delta) v_z \\ &\approx v'''_y - \frac{\sin(\delta)}{\cos(\epsilon)} v'''_z \end{aligned} \tag{5.34}$$

and

$$v_z = \frac{v'''_z}{\cos(\epsilon)} + \tan(\epsilon) v'_y \tag{5.35}$$

Using the proportionality between the Coulomb-sphere velocity components and position difference, the correction equations which reverse the axis skewing are

$$(x_1 - x_2)^{lab} = (x_1 - x_2)^{det} + b(t_1 - t_2)/2 \tag{5.36}$$

$$(y_1 - y_2)^{lab} = (y_1 - y_2)^{det} + \delta(t_1 - t_2)/2 \tag{5.37}$$

$$(z_1 - z_2)^{lab} = (t_1 - t_2) - \epsilon(y_1 - y_2)^{lab} \tag{5.38}$$

where x^{lab} and y^{lab} are space coordinates in the laboratory frame, and x^{det} and y^{det} are detector positions. z^{lab} here is the velocity component of the Coulomb-sphere along the beam direction and is still in units of ns. The approximation $\cos(\delta) \approx 1$ and $\cos(\epsilon) \approx 1$ is used. Sin and tan of the angles are replaced by the angles. The values of the parameters b, δ and ϵ are determined from the simulation and applied to the experimental data. For this reconstruction, b=0.09 ch/ns, δ=0.066 ch/ns and ϵ=0.33 ns/ch were used. As a result of correcting the axes, particles emitted with zero transverse momentum arrive on the same location on the detector. Or, the particle's position on the detector depends now only on its transverse velocity components v'_x and v'_y. This allows one to do the next step in the reconstruction procedure, which is to remove the two-dimensional image distortions.

5.6.2 Image Distortions

The image distortions due to the electrostatic lenses in the apparatus are determined *in situ* by sending a beam of D^+ ions with well-defined laboratory energy and scattering angle through the apparatus and recording their impact position on the detector surface. The flight time of the ions to the detector remains undetermined. Choosing the beam energy and scattering angles such that the D^+ ions have the same kinematics as molecular fragments with $v_z = 0$, the image observed on the detector, $(\vec{v})^{map}$, is distorted in the way as the data. This becomes apparent by setting $v_z = 0$ in Eqns. (5.13)-(5.15):

$$v_x^{map} = af(v_x, v_y) \tag{5.39}$$

$$v_y^{map} = \cos(\delta)g(v_x, v_y) \ . \tag{5.40}$$

This is identical to the left hand side of Eqns. (5.33) and (5.34). Thus the measured map is equivalent to the Coulomb-sphere velocity components in the lab frame, after correcting for the axes tilts.

In section 5.4, the undistorted detector image was obtained by applying Eqns.(5.16) and (5.17) to the measured, distorted positions (x^{map}, y^{map}). Since it was just shown above (Eqns. (5.39),(5.40)) that the measured map is equal to the Coulomb-sphere velocity components, Eqns.(5.16) and (5.17) need to be applied to the measured velocity components x^{lab}, y^{lab} to retrieve the undistorted Coulomb sphere:

$$u_{x,i} = \sum_k a_k \Phi_k(x_i^{lab}, y_i^{lab}) \qquad i = 1, 2 \tag{5.41}$$

$$u_{y,i} = \sum_k b_k \Phi_k(x_i^{lab}, y_i^{lab}) \qquad i = 1, 2. \tag{5.42}$$

Proportionality between position and velocity is inferred as before. The pattern of the map relative to its center depends only weakly on laboratory beam energy, such

that one set of parameters (a_k, b_k) is used to convert the entire Coulomb-sphere. As a result, the undistorted Coulomb-sphere transverse velocity components are given in units of deflector voltage u_x and u_y. They are calibrated into units of momentum in the next step.

5.6.3 Calibration into Momentum

The resulting, undistorted image is transformed into momentum using the calibration factors calculated in section 5.5 through

$$k_x = c_{pos}/s\frac{u_{x,1} - u_{x,2}}{2} \tag{5.43}$$

$$k_y = c_{pos} * s\frac{u_{y,1} - u_{y,2}}{2} \tag{5.44}$$

$$k_z = c_t\frac{(z_1 - z_2)^{lab}}{2} \ . \tag{5.45}$$

s is the scaling factor introduced in sec. 5.4.1, which takes into account to the shifted locations of the deflectors used for the position calibration. To determine variations of the distribution of fragments with respect to the projectile ion velocity, the Coulomb-sphere needs to be transformed into the CM-frame of each collision system.

5.6.4 Summary of the Algorithm

A summary of the reconstruction algorithm is given in Fig. 5.8, which shows the outcome of applying the actual algorithm to both the measured data and to the simulated "data" calculated from SIMION step-by-step. The three top frames (a)-(c) are projections of the measured and simulated data from the N^{2+}+D_2^+ experiment and from the simulation. The first step in the reconstruction is to straighten out the axes. The equations were derived in sec. 5.6.1 and have been applied to the frames (d)-(f). In those frames, the axes are now in the lab frame. The last step in the reconstruction, which is the position mapping (sec. 5.6.2) and the axis calibration

into units of momentum (sec 5.6.3) results in the fully reconstructed Coulomb-sphere. Projections of the reconstructed Coulomb-sphere are shown in frames 5.8(g)-(i) for both experimental data and simulated "data". All projections are approximately circular. In the reconstructed simulation, the radius of each circle is 40 a.u. of momentum, as a result of the explosion energy of E_{coul} = 6 eV per fragment. The same parameters were used to reconstruct the data and the simulation, except for the coefficients of the position map. To compare apples with apples, the position axes in the simulation are converted from mm into channels, with a conversion factor of 2.4 ch/mm.

5.6.5 Quality of the Reconstruction Algorithm

The quality of the reconstruction procedure, or the angular uncertainty introduced by the imperfection of the reconstruction procedure, can be estimated by measuring the change in detector position as a function of beam energy and comparing those values to the ones used in the reconstruction, which had been obtained in the simulation. The measured shift in detector position is 11 ch horizontal and 8 ch vertical for an energy difference of ΔE=(6.7 keV - 6.3 keV), which translates to a time-of-flight difference of 73 ns, using $\Delta t = \Delta p / c_t$ where Δp is the momentum difference of two particles with energies E_1=6.7 keV and E_2=6.3 keV, and c_t is the time calibration factor derived in Eq. (5.28). This results in 0.14 ch/ns horizontal and 0.106 ch/ns vertical shift measured, compared to 0.09 ch/ns horizontal and 0.066 ch/ns vertical from the simulation. Translating these numbers into angles (using 0.4 ch/ns to roughly calibrate the time-axis into the same dimension as the position axes), the measured and simulated angles differ by 9° at worst (for the horizontal case). Thus the uncertainty in angle introduced by the reconstruction procedure is 9°.

Raw Coulomb-sphere in detector frame:

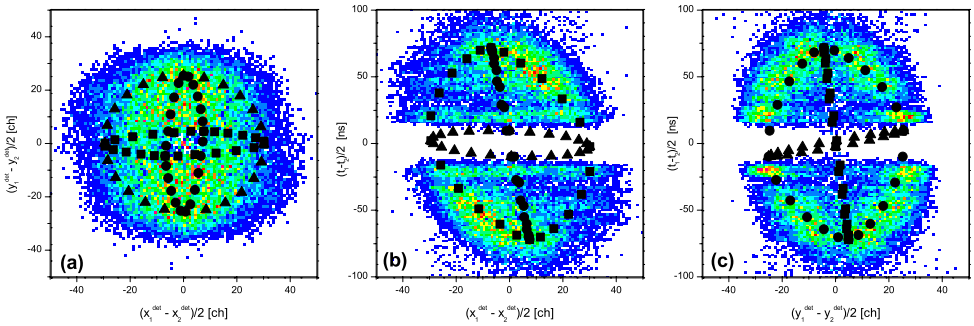

Axis corrections (sec. 5.6.1):

$$
\begin{aligned}
x_i^{lab} &= x_i^{det} + b(t_i - t_{3-i})/2 \qquad i = 1,2 \\
y_i^{lab} &= y_i^{det} + \delta(t_i - t_{3-i})/2 \qquad i = 1,2 \\
(z_1^{lab} - z_2^{lab}) &= (t_1 - t_2) - \epsilon(y_1^{lab} - y_2^{lab})
\end{aligned}
$$

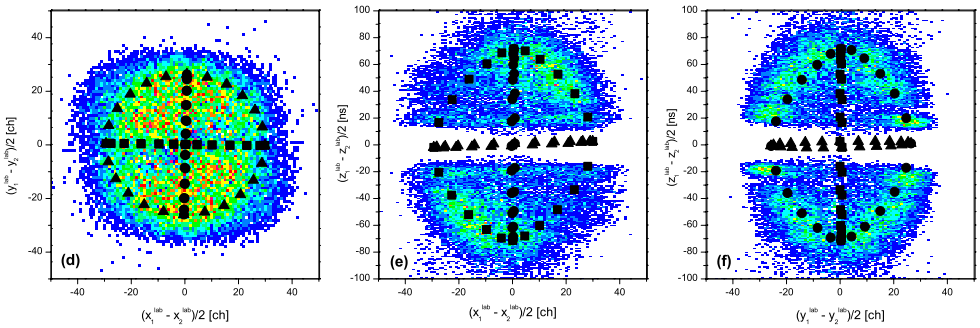

Image distortions (sec. 5.6.2):

$$
\begin{aligned}
u_{x,i} &= \sum_k a_k \Phi_k(x_i^{lab}, y_i^{lab}) \qquad i = 1,2 \\
u_{y,i} &= \sum_k b_k \Phi_k(x_i^{lab}, y_i^{lab}) \qquad i = 1,2
\end{aligned}
$$

Momentum calibration (sec. 5.6.3):

$$
\begin{aligned}
k_x &= (u_{x,1} - u_{x,2})/2 * c_{pos}/s \\
k_y &= (u_{y,1} - u_{y,2})/2 * c_{pos} * s \\
k_z &= (z_1^{lab} - z_2^{lab})/2 * c_t
\end{aligned}
$$

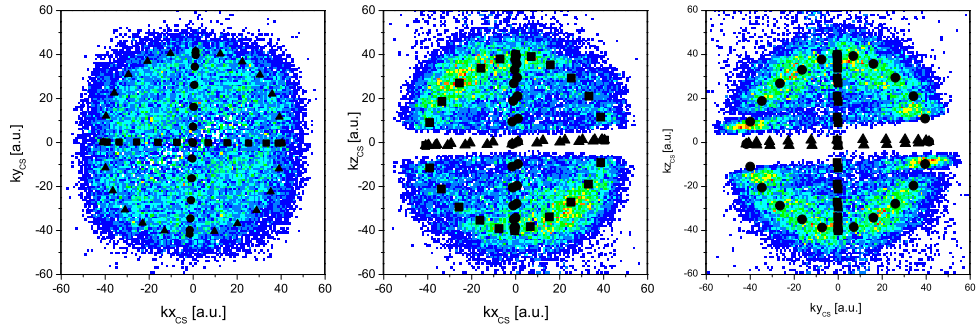

Figure 5.8: *The reconstruction procedure: Summary of the equations. Step-by-step results for both data and simulation.*

5.7 Transformation into CM Coordinates

The last step in the data analysis is to transform the reconstructed Coulomb-sphere into the center-of-mass frame of the collision system. The lab-and CM-coordinate axes were chosen such that this operation amounts to a clockwise rotation about the $\mathbf{v}_y$-axis by γ (see fig. 1.5 on page 12).

$$k_x^{CM} = k_x^{lab} * \cos(\gamma) - k_z^{lab} * \sin(\gamma) \tag{5.46}$$

$$k_y^{CM} = k_y^{lab} \tag{5.47}$$

$$k_z^{CM} = k_z^{lab} * \cos(\gamma) + k_x^{lab} * \sin(\gamma) \tag{5.48}$$

The angle γ for the various projectiles are tabulated in table 1.2 on page 13.

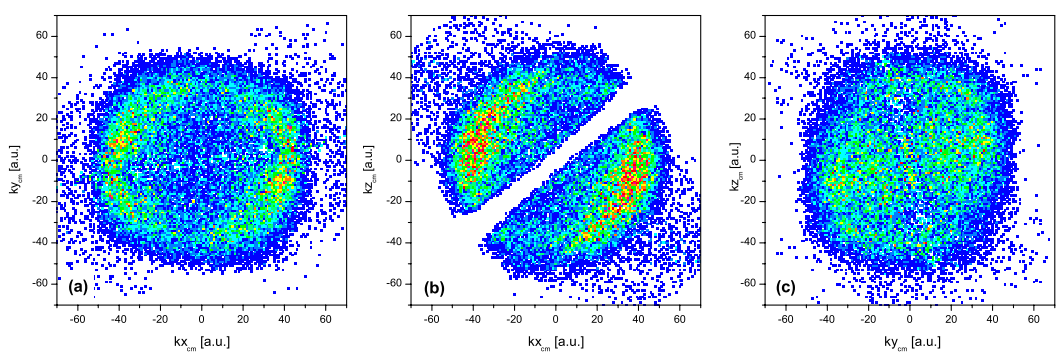

Figure 5.9: *Projections of the Coulomb-sphere in $N^{2+}+D_2^+$ collisions, corrected, calibrated and transformed into the collision system's center-of-mass frame.*

The relative velocity is along the kz-axis. The spectra are somewhat difficult to interpret because of the pulse-pair resolution gap, which is now cutting out a slice of the sphere at some angle with respect to the projections. Nevertheless, frame Fig. 5.9(a) is the projection perpendicular to the relative velocity direction. The pulse-pair resolution gap cuts a leaf-shaped section in the center. In the second frame, Fig. 5.9(b), the pulse-pair gap is still clearly visible. The intensity peaks left and right of the relative velocity direction, thus more molecular breakups occurred if

the molecular ion was aligned perpendicular to the relative velocity. For perpendicular alignment, the last frame, Fig. 5.9(c), should be identical to the (b). Obviously both frames are affected by the gap in a different manner. In frame (c), the pulse-pair resolution gap cuts out a ring on the outside.

5.8 Energy distribution of the Fragments

The energy distribution of the fragments is obtained through

$$E_{frag} = (k_x^2 + k_y^2 + k_z^2)/2m \tag{5.49}$$

from the fragment momentum components calculated in the previous section. To obtain the energy per fragment in eV from the momenta in a.u., $E_{frag} = k^2 \cdot 0.0037$. The resulting distribution is shown in Fig. 5.10. Note that in this figure, the energy of one fragment is plotted, as opposed to the theoretical calculation in Fig. 1.10 on page 20, where the energy sum of the two fragments is plotted. The energy distribution observed in the experiment is asymmetric, with a centroid similar to that of the calculated distribution, but the specific shape seen in Fig. 1.10 is not observed.

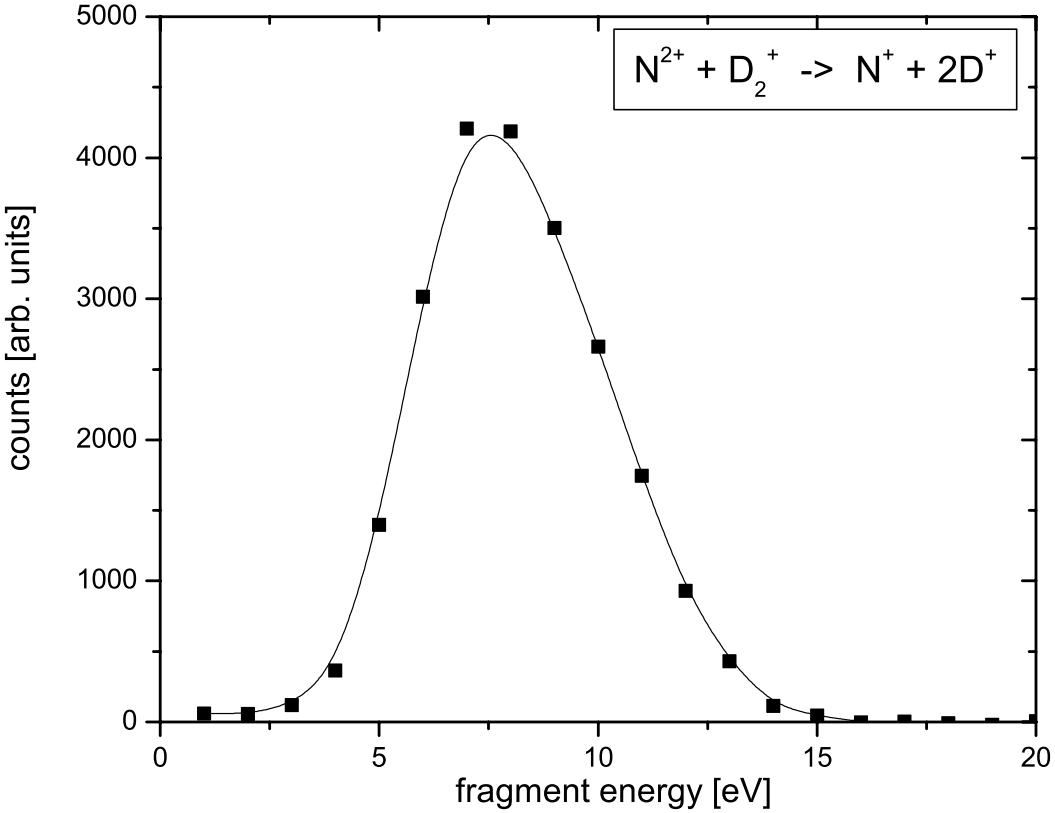

Figure 5.10: *Energy distribution of a D^+ fragment produced in a collision between N^{2+} and D_2^+.*

Chapter 6

Results and Discussion

In this chapter, the results of the collision experiments are presented. Measurements of the molecular alignment were performed for the four collision systems:

$$\begin{aligned}
Ar^{2+} + D_2^+ &\longrightarrow Ar^+ + 2D^+ \qquad v_{coll} = 0.19 \text{ a.u.} \\
N^{2+} + D_2^+ &\longrightarrow N^+ + 2D^+ \qquad v_{coll} = 0.23 \text{ a.u.} \\
He^{2+} + D_2^+ &\longrightarrow He^+ + 2D^+ \qquad v_{coll} = 0.42 \text{ a.u.} \\
He^{2+} + D_2^+ &\longrightarrow He^+ + 2D^+ \qquad v_{coll} = 0.51 \text{ a.u.}
\end{aligned}$$

v_{coll} is the relative velocity between the projectile and target ions. Not only its magnitude, but more importantly its direction is different for every collision system. If the electron capture shows an anisotropy as a function of molecular alignment, this effect has to be symmetric about the relative velocity vector. The kinematic quantities of the various projectile ions used in the experiment are tabulated in table 1.2 on page 13.

6.1 The Raw Coulomb-spheres

Fig. 6.1 shows projections of the raw Coulomb-spheres as observed in the detector frame. Each dataset has one row of frames. The projections are

(a) the projection onto the detector surface (x^{det}, y^{det})

(b) the projection onto the (x^{det}, t) plane, spanned by the detector x-position and flight time

(c) the projection onto the (y^{det}, t) plane, spanned by the detector y-position and flight time.

The gap in the spectra (b) and (c) is caused by the pulse-pair resolution of the multi-hit detector. The spectra for the four collision systems were taken under similar conditions. Qualitatively, the anisotropy in those frames can be investigated even before performing any corrections. The relative velocity vector is lying in the (x^{lab}, z^{lab}) plane, which, is closest to the (x^{det}, t) plane (column (b) in Fig. 6.1). In this plane, the direction of the molecular ion beam is downward, and of the atomic projectile beam to the left. Thus the relative velocity vector points up and to the left in frames (b). The intensities in those frames is peaked in the second and third quadrant, thus perpendicular to the relative velocity. The peak of the intensity distribution in frames (b) is shifting away from the pulse-pair resolution gap, starting with the Ar^{2+} projectile going to the faster He^{2+} projectile. The Ar^{2+} projectile is slower than the D_2^+ target, thus the relative velocity vector is closer to the time-of-flight direction. At v_{coll}=0.5 a.u., the He^{2+} projectile is faster than the D_2^+ target, in this case the relative velocity vector is close to parallel to x^{det} direction. The intensity peak should move in the opposite direction, e.g. starting out close to the time gap for Ar^{2+}, drifting towards the top and bottom of the distribution for the faster He^{2+}.

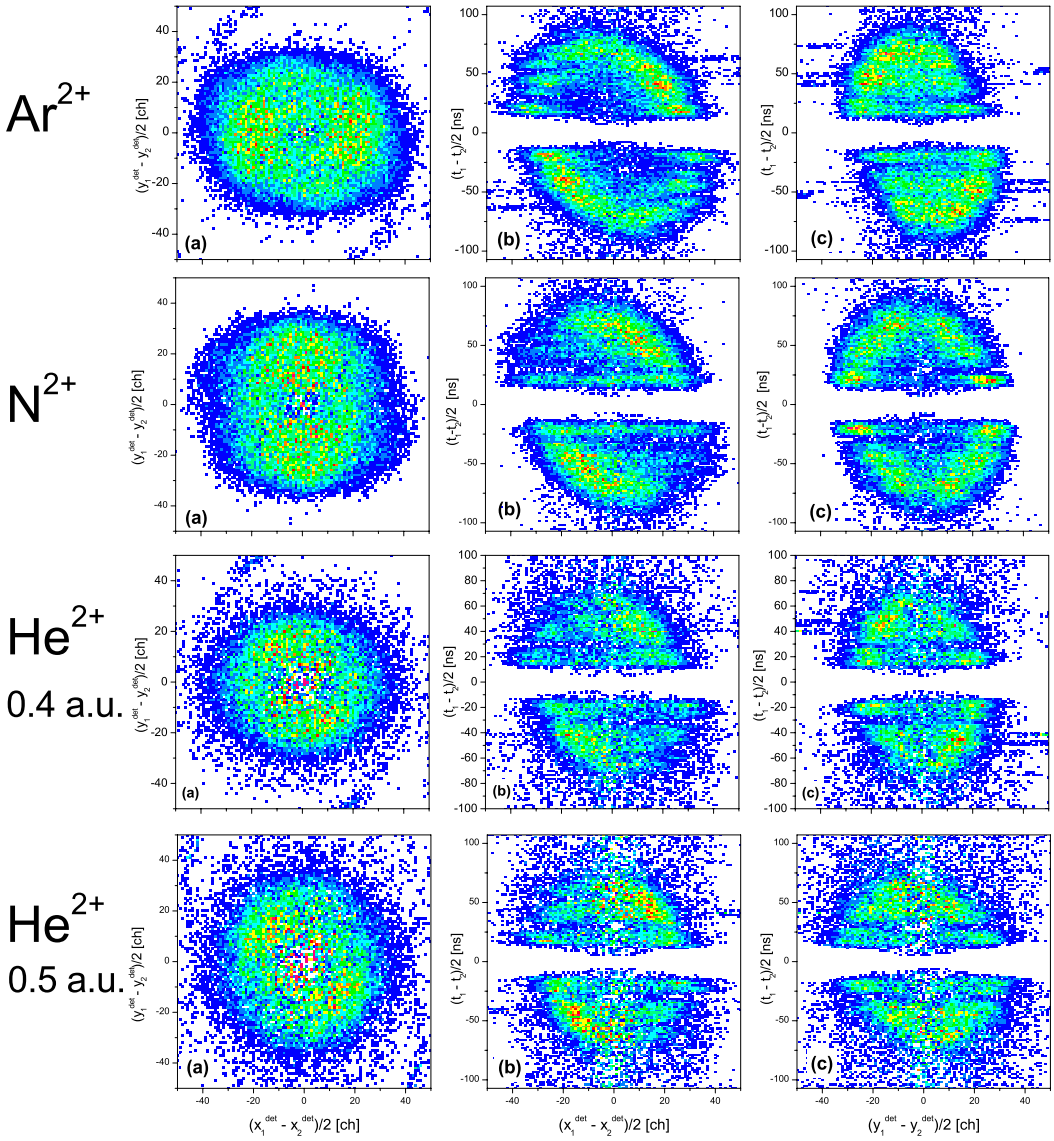

Figure 6.1: *The raw Coulomb sphere in the detector frame. Top:* $Ar^{2+} + D_2^+$, v_{coll}*=0.2 a.u.; second:* $N^{2+} + D_2^+$, v_{coll}*=0.2 a.u.; third:* $He^{2+} + D_2^+$, v_{coll}*=0.4 a.u.; bottom:* $He^{2+} + D_2^+$, v_{coll}*=0.5 a.u.*

6.2 The Corrected Coulomb-sphere in the Laboratory Frame

Applying the reconstruction scheme as described in section 5.6 to the measured data, and taking slices instead of projections, results in the distributions shown in Fig. 6.2. All datasets have been reconstructed using the same parameters. A separate position map has been created for every dataset as described in sec. 5.4. The slices shown are taken around the (v_x^{lab}, v_z^{lab}) plane by requiring that $|k_y| < 20$ a.u. The relative velocity

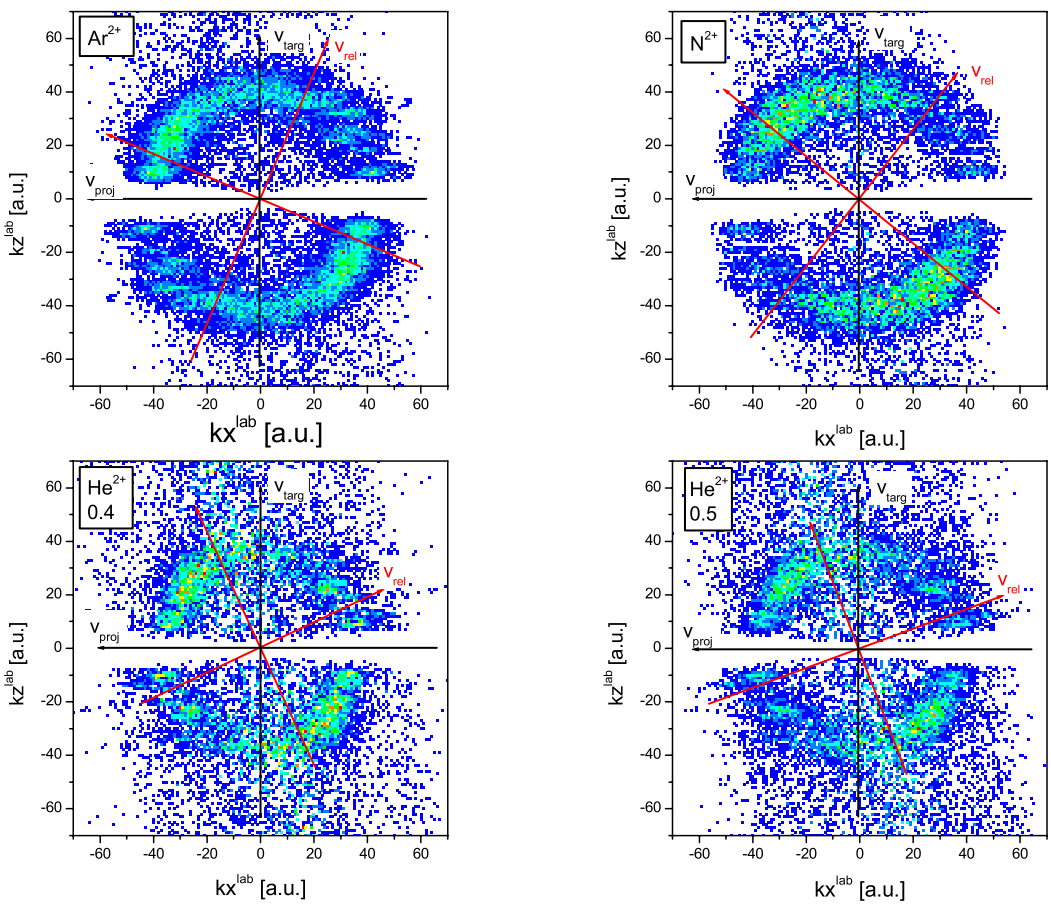

Figure 6.2: *Slices of the Coulomb-sphere centered on the $(v_{cs,x}^{lab}, v_{cs,z}^{lab})$ plane. The directions of the ion beams in the lab frame are shown in black. The relative velocity direction and the direction perpendicular to the relative velocity are shown in red. The latter ones are different for each collision system.*

vector lies in the first quadrant of this plane, since the v_z^{lab} is now pointing up as a result of the calibration. The intensity maxima in the two-dimensional distributions appear clearly, as in the raw data.

From those slices, the angular distributions are obtained. It is clear that there will be two areas of potential problems in those spectra. The pulse-pair resolution gap will create a hole in the angular distribution. Also the background events will affect the distribution. In all spectra, error bars are much larger where background was subtracted. Especially when taking the He data, the multi-hit detector's channelplates started to lose efficiency at the positions where the background events had been impacting at quite a high rate. This effect got worse over time, such that the He^{2+} (v_{coll} = 0.4 a.u.) data is affected most, then the He^{2+} (v_{coll} = 0.5 a.u.) somewhat less, and the effect does not seem to be strong neither in the Ar^{2+} or in the N^{2+} data, which were taken earlier. The efficiency "holes" in the He^{2+} data are filled in software by introducing a gaussian shaped efficiency correction function covering the affected area. No correction is applied to the Ar^{2+} or the N^{2+} data. The angular ranges corresponding to those regions with potential problems are shaded in Fig. 6.3. The data from within those angular ranges is excluded in the final alignment curves.

6.3 The Angular Distributions

Fig. 6.3 shows the alignment curves for each collision system: The data is plotted as a function of alignment angle of the molecular axis. The errorbars shown are statistical errors only. Errorbars are not shown in the grey-shaded areas corresponding to the BG distribution. In this region, the errorbars are by a factor of 1.4(Ar^{2+}–D_2^+) to 3.2(He^{2+}–D_2^+; 1.7 for N^{2+}–D_2^+) larger than the statistical error, depending on the true-to-random ratio of each collision system (see Table 3.6 on page 64).

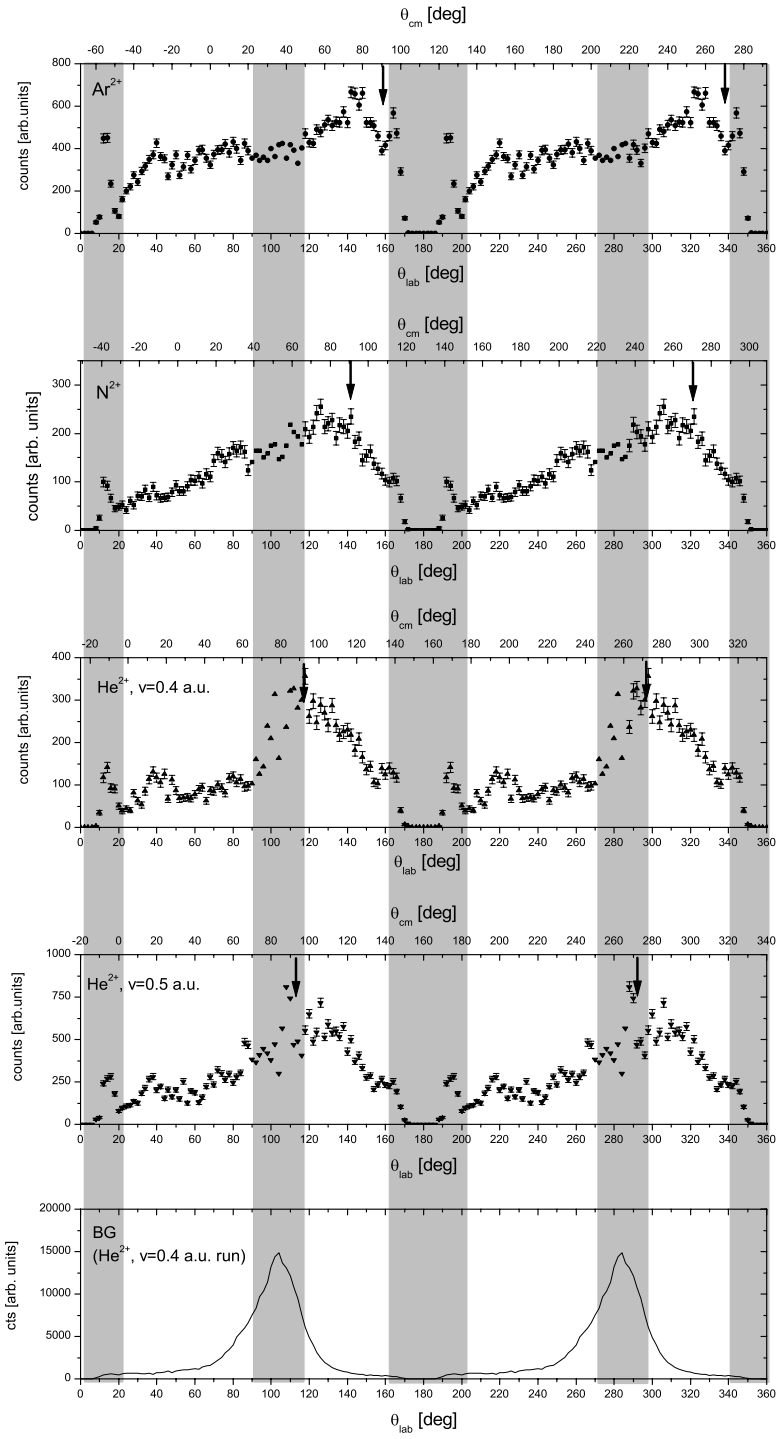

Figure 6.3: *Electron capture as a function of alignment angle. Bottom axis: Alignment with respect to the projectile velocity. Top axis: Alignment with respect to the relative velocity. Bottom graph: Angular distribution of the background collisions.*

The angles are defined as in Fig. 6.4: The bottom axes of each graph show the alignment angle θ_{lab} relative to the projectile velocity. The top axis of each graph is the alignment angle θ_{cm} with respect to the relative velocity of each collision system. It is shifted by a constant angle $\gamma = \text{invtan}(|v_{at}|/|v_{mol}|)$ which is different for the various systems. A little arrow points to $\theta_{cm} = 90°$ and $\theta_{cm} = 270°$ in each graph. The distributions should be symmetric about these points. Note that the distributions have been obtained from slices of the Coulomb-sphere, not from projections, thus in the absence of any alignment effects, those curves would be flat.

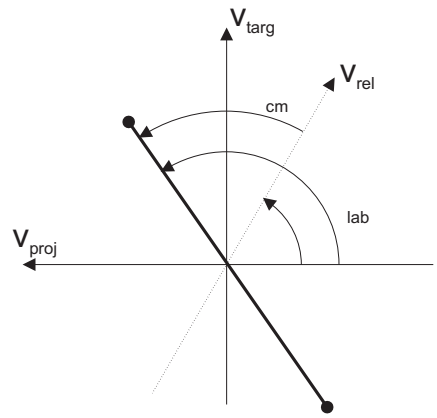

Figure 6.4: *The laboratory- and center-of-mass angles*

The bottom axis is identical for every collision system. Hence the angular ranges that are affected by the pulse-pair resolution gap and the efficiency hole are the same. (The positions related to the background events were very similar for every run.) The bottom graph in Fig. 6.3 shows the angular distribution of the background collisions, to identify the angular range where efficiency problems may have occured. The range in angles is close to the perpendicular CM-angles of the Helium data. The data in Fig. 6.3 has been corrected for the efficiency loss (see appendix E). Nevertheless, the shaded areas are excluded in the final results. The experimental alignment curves from Fig. 6.3 are symmetrized about $\theta_{cm} = 90°$ for each collision system, as shown in Fig. 6.5. Only data points in the non-shaded areas are included. In regions where data from two different θ_{lab} contribute, the geometric average is used.

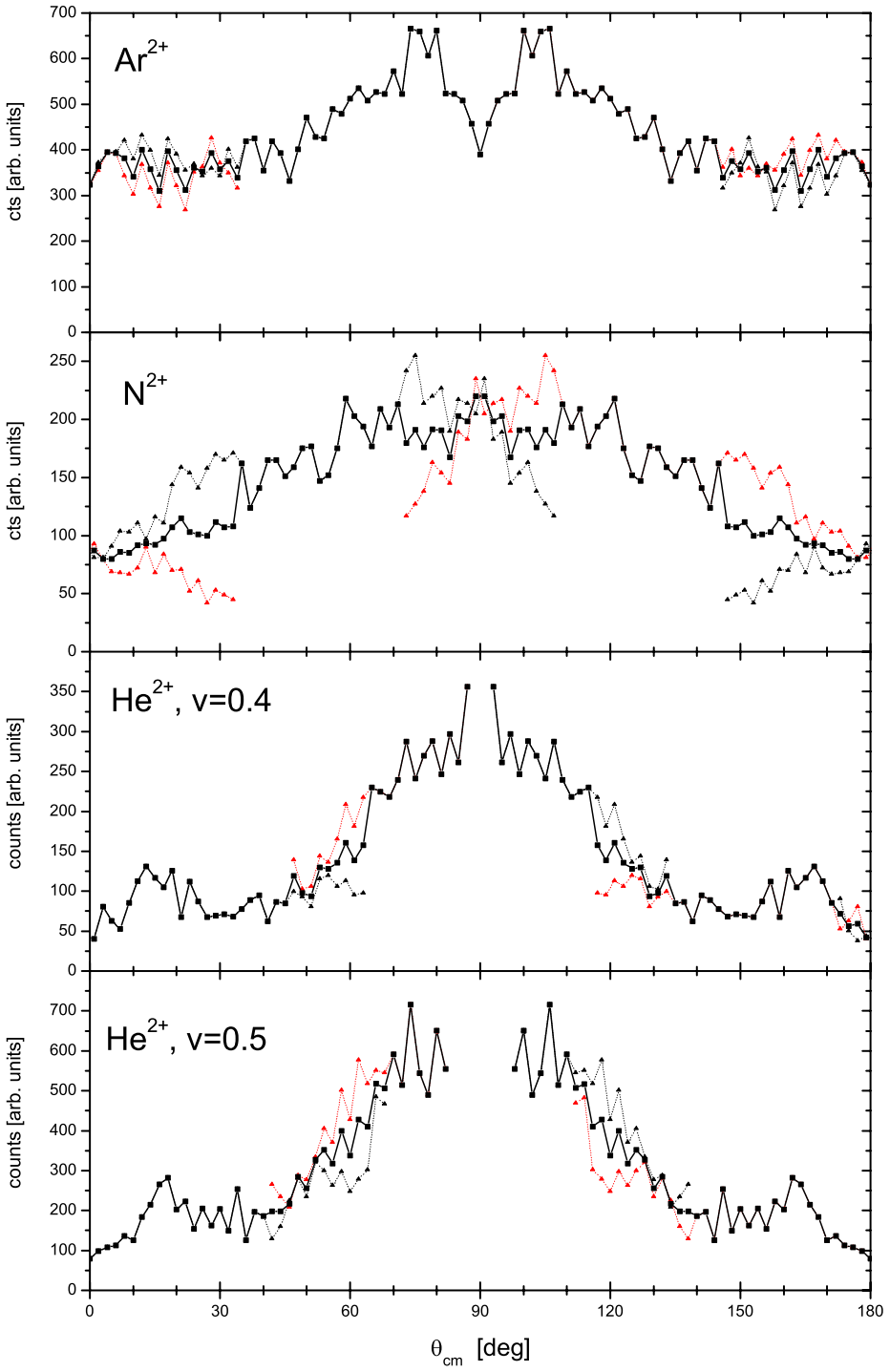

Figure 6.5: *Result of symmetrizing the alignment curves for electron capture of Fig. 6.3 about θ_{cm}=90° for each collision system. The dotted lines are data from different θ_{lab} contributing to the same θ_{cm}. In those regions, the geometrical average is taken.*

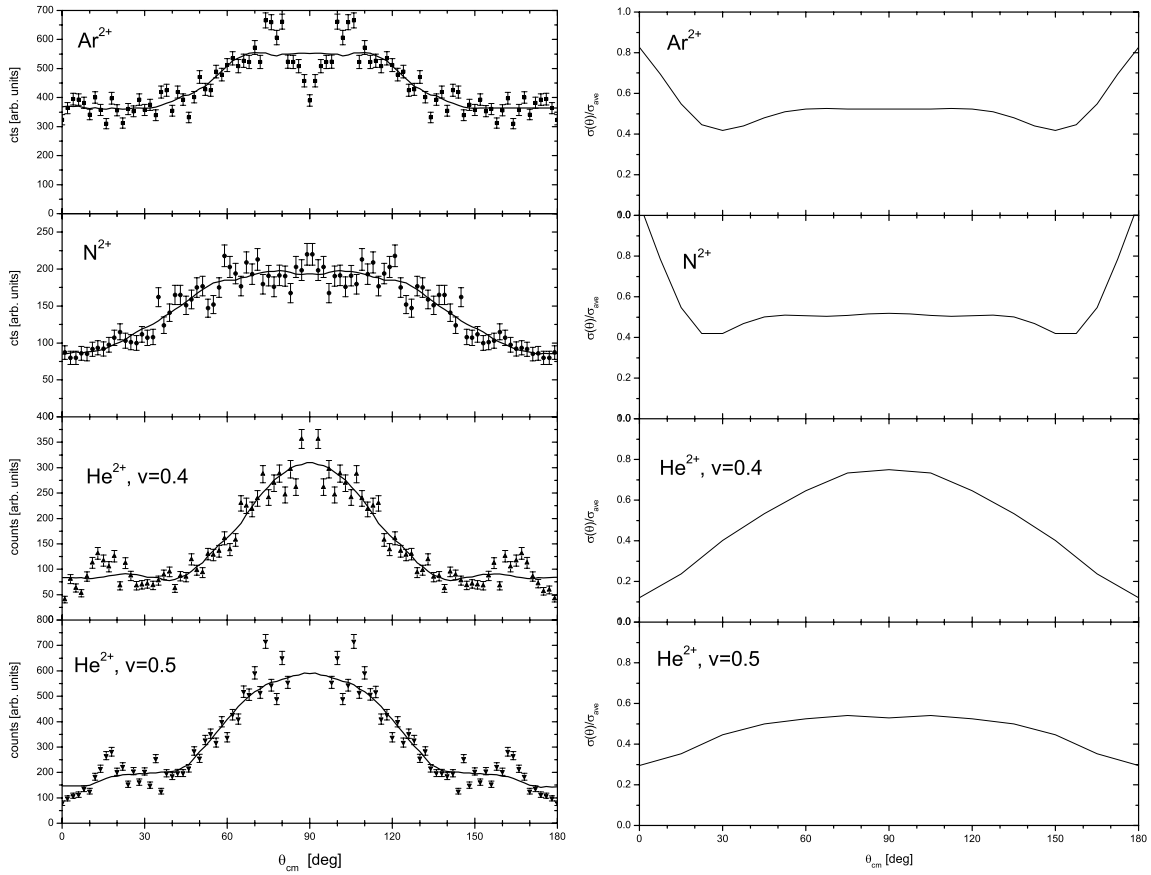

Figure 6.6: *Electron capture as a function of molecular alignment with respect to the relative collision velocity. Left: Experimental data (the line is a smooth of the data points). The data has been symmetrized about $\theta_{cm} = 90°$ for every collision system. Right: Predictions of the interference model in sec. 2.2.*

The resulting final experimental alignment curves are shown in the left column of Fig. 6.6. The errorbars show the statistical error only. The line is result of a smoothing of the data. The dip at θ_{cm} in the Ar^{2+} data is caused by the rapid drop-off near the pulse-pair resolution gap and not physical. The experimental data are compared to the theoretical model from section 2.2, which predicts the alignment curves shown in the right column of the figure.

For both He^{2+} collision systems, there is qualitative agreement between theory and experiment. In both cases electron capture is favored from molecular ions aligned

perpendicular to the relative collision velocity. The theoretical curve is somewhat broader for the lower velocity; this effect is also found in the data. For the Ar^{2+} and the N^{2+} collision systems, the agreement between theory and experiment is not satisfactory. The experiment shows that electron capture is favored for perpendicular alignment, as for the He^{2+} projectiles. The theoretical alignment curve however shows spikes in the forward and backward directions.

This brings some doubts whether those spikes are real or are caused by the nature of the model itself. As mentioned earlier, both the Ar^{2+} and N^{2+} collision systems are very near-resonant, causing oscillations in the atomic transition probabilities. Those oscillations in turn are the cause for the forward- and backward-peaking of the alignment curves. Omitting this behaviour near 0° and 180°, the remaining part of the alignment curve is quite constant, with a slight increase for perpendicular alignment, which is not nearly as pronounced as in the experimental data.

At this point the question arises of how large the experimental uncertainty in angle is. The reconstruction scheme introduces an uncertainty of 9°. Nevertheless, even if the uncertainty was as large as 20°, the experimental data shows convincingly that electron capture occurs more frequently from molecules aligned perpendicular to the beam. Especially for the near-resonant systems, where the real-to-random ratio is relatively large, there is no sign in the data that would indicate the spikes predicted by the interference model.

6.4 A Note on Total Cross Sections

In previous experiments, the apparatus has been used to measure total cross sections for resonant charge exchange in collisions between He^{2+} and He^{+}, Ne^{2+} and Ne^{+}, as well as Ar^{2+} and Ar^{+} [36, 34]. With the apparatus in its current setup, the

measurement of total cross sections is difficult for the following reasons:

- To determine total cross sections, one needs to know the detector efficiencies. The efficiency of a single-hit detector can be measured *in-situ*, following the procedure described by Savin and coworkers [43]. It is not obvious of how to determine the efficiency of a multi-hit detector, which comes into play because in our experiment, a triple coincidence is required to identify the ion-molecular ion collisions since the width of the coincidence peak of one fragment with a projectile is large (compare Fig. 3.13(a) and (c)). In the total cross section measurements carried out in Giessen (see appendix A), it was possible to identify the ion-molecular ion collisions through a two particle coincidence, because the background was lower, and because the coincidence peak was barely broadened by the expanding Coulomb-sphere.

- To reduce the contribution of background collisions, a beam cleaner has been installed in the collision region. The efficiency of this device would need to be determined carefully. During the experiments described here, the beam cleaner has been used only to reduce background in the projectile beam, focussing on reducing random events rather than ensure maximum efficiency.

Chapter 7

Conclusion

In conclusion, we have shown the feasibility of determining the alignment of the molecular axis in an ion - molecular ion - collision and we have measured the alignment dependence of single electron capture from a D_2^+ molecular ion by Ar^{2+} (v_{coll}=0.19 a.u.), N^{2+} (v_{coll}=0.23 a.u.) and He^{2+} (v_{coll}=0.4 a.u. and 0.5 a.u.). For all the collision systems studied, we observed a pronounced peak in the intensity distribution if the molecular ion was aligned perpendicular to the relative collision velocity. We compared the experimental data to predictions of an interference model. The model prediction qualitatively agreed with the measured alignment dependence for both He^{2+} collision systems. For the near-resonant collision systems however, experiment and theory do not agree.

Comparing all four collision systems, the experimental data indicate that perpendicular alignment favors electron capture, independent of the energetics of the collision system. This is definitely in disagreement with the model, which implies that the alignment dependence should strongly depend on collision velocity and reaction Q-value.

As a future development, it would be interesting to carry out an experiment for a collision system which is predicted to favor parallel alignment, such as He^{2+}-D_2^+ at v_{coll} = 0.2 a.u. for instance. With our current apparatus, this is not feasible

because of the low electron-capture cross section at this collision velocity. The use of higher charge state projectiles could circumvent this problem, since the total cross section is expected to increase for bare projectiles with $Z > 2$. Again, with the ECR source currently available, the beam currents delivered for higher charge states are limited and may not be sufficient to carry out an ion-ion collision experiment. In principle, having better control of the experimental parameters could eventually allow to quantitatively determine the energy distribution of the molecular fragments, possibly leading to a characterization of the initial vibrational state distribution of the molecular ion produced in the ion source. A future improvement of the theoretical model would be to include a distribution of internuclear separations, rather than to calculate capture cross sections at the fixed equilibrium separation. This would result in a more realistic modeling of the experiment.

Bibliography

[1] ALADDIN database. www-amdis.iaea.org/aladdin/html. Maintained by J. A. Stephens at the International Atomic Energy Agency (www.iaea.org).

[2] Richard N. Zare. Photoejection dynamics [1]. *Mol. Photochem.*, 4:1, 1972.

[3] H. F. Busnego, S. E. Corchs, and R. D. Rivarola. Single electron capture from molecular hydrogen targets by impact of protons and α particles. *Phys. Rev. A*, 57:2701, 1998.

[4] M. M. Sant'Anna, W. S. Melo, A. C. F. Santos, M. B. Shah, G. M. Sigaud, E. C. Montenegro, H. F. Busnego, S. E. Corchs, R. D. Rivarola, and L. Gulyas. Electronic capture by He^{2+} from atomic and molecular hydrogen. *Phys. Rev. A*, 61:052717, 2000.

[5] Frank Melchert. Ladungsändernde Stöße im keV Energiebereich. Habilitationsschrift, Justus Liebig Universität Gießen, 1997.

[6] R. Shingal and C. D. Lin. Orientation-dependent atomic model for electron transfer in ion-molecule collisions: Applications to $H^+ + H_2$ and $He^{2+} + H_2$. *Phys. Rev. A*, 40:1302–1309, 1989.

[7] R. Padgett and B. Peart. Merged-beam measurements of the mutual neutralization of O_2^+/O^- and NO^- ions. *J. Phys. B*, 31:L995, 1998.

[8] A. Naji, K. Olamba, J. P. Chenu, S. Szücs, and F. Brouillard. Associative ionization in collisions of H_2^+,D_2^+ with H^- and D^-. *J. Phys. B*, 31:4887, 1998.

[9] H Bräuning, I Reiser, A Diehl, A Theiß, E Sidky, C L Cocke, and E Salzborn. Charge transfer in collisions of H_2^+ ions with He^{2+} and Ar^{2+}. *J. Phys. B*, 34:L321 – L325, 2001.

[10] U. Werner, N. M. Kabachnik, V. N. Kondratyev, and H. O. Lutz. Orientation effects in multiple ionization of molecules by fast ions. *Phys. Rev. Lett.*, 79:1662–1665, 1997.

[11] N. Stolterfoht, B. Sulik, V. Hoffmann, B. Skogvall, J. Y. Chesnel, J. Rangama, F. Frémont, D. Hennecart, A. Cassimi, X. Husson, A. L. Landers, J. A. Tanis, M. E. Galassi, and R. D. Rivarola. Evidence for interference effects in electron emission from H_2 colliding with 60 MeV/u Kr^{34+} ions. *Phys. Rev. Lett.*, 87:023201, 2001.

[12] T. F. Tuan and E. Gerjuoy. Charge Transfer in Molecular Hydrogen. *Phys. Rev.*, 117:756–763, 1960.

[13] N. C. Deb, A. Jain, and J. H. McGuire. Electron capture from a hydrogen molecule at a fixed orientation of the molecular axis. *Phys. Rev. A*, 38:3769, 1988.

[14] Wolfgang Fritsch and Chii-Dong Lin. Theory of ion-atom collisions - Coupled Channel Methods. *Phys. Rep.*, 202:1, 1991.

[15] Y. D. Wang, J. H. McGuire, and R. D. Rivarola. Impact-parameter treatment of high-velocity electron capture from diatomic molecules at fixed orientations. *Phys. Rev. A*, 40:3673, 1989.

[16] S. Cheng, C. L. Cocke, V. Frohne, E. Y. Kamber, J. H. McGuire, and Y. Wang. Angular distributions of dissociated deuterons by impact of 2-16-MeV 0^{8+}. *Phys. Rev. A*, 47:3923–3929, 1993.

[17] M. Kimura. Charge transfer in ion-molecule collisions at keV energy regime: Study of H^++H_2 collisions by the electron-translation-factor-modified molecular-orbital-expansion method. *Phys. Rev. A*, 32:802, 1985.

[18] M. Kimura, S. Chapman, and N. F. Lane. Electron capture in Ar^++H_2 collisions in the keV energy regime. *Phys. Rev. A*, 33:1619, 1986.

[19] M. Kimura, Y. LI, G. Hirsch, and R. J. Buenker. Elastic and inelastic processes in H^++CH_4 collisions in the low-kilo-electron-volt regime. *Phys. Rev. A*, 52:1196, 1995.

[20] M. Kimura, Y. Li, G. Hirsch, and R. J. Buenker. Elastic and inelastic processes in H^++C_2H_2 collisions below the 1.5 keV regime. *Phys. Rev. A*, 54:5019, 1996.

[21] M. Kimura, J. Gu, G. Hirsch, R. J. Buenker, and P. C. Stancil. Electron capture in collisions of protons with CO molecules in the keV region: The steric effect. *Phys. Rev. A*, 61:032708, 2000.

[22] Y. D. Wang and J. H. McGuire. Orientation dependence in electron capture to arbitrary projectile n states from molecular hydrogen. *Phys. Rev. A*, 44:367, 1991.

[23] A. K. Edwards, R. M. Wood, M. A. Mangan, and R. L. Ezell. Collisional ionization and excitation of H_2: Dependence on the orientation of the internuclear axis. *Phys. Rev. A*, 46:6970–6976, 1992.

[24] B. Siegmann, U. Werner, Z. Kaliman, N. M. Kabachnik, and H. O. Lutz. Orientation dependence of multiple ionization of diatomic molecules in collisions with fast highly charged ions. *Phys. Rev. A*, 65:010704(R), 2001.

[25] K. Wohrer and R. L. Watson. Model calculations of multielectron ionization of O_2 molecules by fast-heavy-ion impact. *Phys. Rev. A*, 48:4784, 1993.

[26] N. M. Kabachnik, V. N. Kondratyev, Z. Roller-Lutz, and H. O. Lutz. Multiple ionization of atoms and molecules in collisions with fast ions. II. ion-molecule collisions. *Phys. Rev. A*, 57:990–996, 1998.

[27] T. M. Kereselidze, H. A. Mourad, and M. F. Tzulukidze. Electron in the field of three Coulomb centres: asymptotic solutions. *J. Phys. B*, 25:2957, 1992.

[28] J. Los and T. R. Govers. Collision-induced dissociation of diatomic ions. In R. G. Cooks, editor, *Collision Spectroscopy*, page 323 ff. Plenum Press, New York, 1978.

[29] Friedrich von Busch and Gordon H. Dunn. Photodissociation of H_2^+ and D_2^+: Experiment. *Phys. Rev. A*, 5:1726 – 1743, 1972.

[30] G. Herzberg. *Spectra of diatomic molecules.* D. van Norstrand, Toronto, New York, London, 1950.

[31] M. H. Prior. Private Communication, 2001.

[32] B. H. Bransden and C. J. Joachain. *Physics of Atoms and Molecules.* Longman Scientific & Technical, New York, 1992.

[33] J. P. Lowe. *Quantum Chemistry.* Academic Press, New York, 1993.

[34] C Y Chen, C L Cocke, J P Giese, F Melchert, I Reiser, M Stockli, E Sidky, and C D Lin. Studies of charge exchange in symmetric ion-ion collisions. *J. Phys. B*, 34:469–475, 2001.

[35] Charlotte E Moore. *Atomic Energy Levels*, volume 1. Natl. Bur. Stand. (U. S.) No. NSRDS-NBS35 (U.S. G.P.O.), Washington D.C., 1971.

[36] Chun-Yen Chen. *Single charge exchange in ion-ion collisions.* PhD thesis, Kansas State University, 1998.

[37] R Dörner, V Mergel, O Jagutzki, L Spielberger, J Ullrich, R Moshammer, and H Schmidt-Böcking. Cold target recoil ion momentum spetroscopy: A 'momentum microscope ' to view atomic collision dynamics. *Phys. Rep.*, 330:95–192, 2000.

[38] Joseph Ladislas Wiza. Microchannel plate detectors. *Nucl. Instrum. & Methods*, 162:587–601, 1979.

[39] C. Chaudhuri, S. Sanyal, and T. K. Rai Dastidar. Theoretical study of single and double charge transfer in He^{2+}-He collisions at kilo-electron-volt energies in a diabatic molecular representation. *Phys. Rev. A*, 52:1137, 1995.

[40] W. Seim, A. Müller, I. Wirkner-Bott, and E. Salzborn. Electron capture by Li^{i+} (i=2,3), N^{i+} and Ne^{i+} (i=2,3,4,5) ions from atomic hydrogen. *J. Phys. B*, 14:3475, 1981.

[41] J. F. Williams and D. N. F. Dunbar. Charge exchange and dissociation cross sections for H_1^+, H_2^+, H_3^+ ions of 2- to 50-keV energy incident upon hydrogen and the inert gases. *Phys. Rev.*, 149:62, 1966.

[42] André T. J. B. Eppink and David H. Parker. Velocity map imaging of ions and electrons using electrostatic lenses: Application in photoelectron and photofragment ion imaging of molecular oxygen. *Rev. Sci. Instrum.*, 68:3477–3484, 1997.

[43] D. W. Savin, L. D. Gardner, D. B. Reisenfeld, A. R. Young, and J. L. Kohl. *In situ* absolute calibration of a channel electron multiplier for detection of positive ions. *Rev. Sci. Instrum.*, 66:67–71, 1995.

[44] William H. Press, Brian P. Flannery, Saul A. Teukolsky, and William T. Vetterling. *Numerical Recipes in C.* Cambridge University Press, New York, 1990.

Appendix A

Total Cross Section Measurement

INSTITUTE OF PHYSICS PUBLISHING JOURNAL OF PHYSICS B: ATOMIC, MOLECULAR AND OPTICAL PHYSICS

J. Phys. B: At. Mol. Opt. Phys. **34** (2001) L321–L325 www.iop.org/Journals/jb PII: S0953-4075(01)22351-7

LETTER TO THE EDITOR

Charge transfer in collisions of H_2^+ ions with He^{2+} and Ar^{2+}

H Bräuning[1], I Reiser[2], A Diehl[1], A Theiß[1], E Sidky[2], C L Cocke[2] and E Salzborn[1]

[1] Institut für Kernphysik, Strahlenzentrum, Justus-Liebig Universität, Giessen, Germany
[2] J R MacDonald Lab, Kansas State University, Manhattan, KS, USA

E-mail: Harald.Braeuning@strz.uni-giessen.de

Received 28 February 2001

Abstract
Using the crossed-beams technique, we have measured absolute total cross sections for electron capture from H_2^+ molecular ions by He^{2+} and Ar^{2+} at relative velocities $v_{rel} = 0.7$–1.3 au. With He^{2+} a distinct maximum around $v_{rel} = 1$ au is observed, which can be attributed to the large Q-value for the dominant channel of this reaction. Theoretical calculations using an atomic model for ion–molecule collisions are in very good agreement with the experimental data.

Charge changing collisions between ions are of fundamental interest as an ideal testing ground for theory [1–4] as well as for their application in plasma physics, accelerator and fusion research [5]. In contrast to ion–atom collisions, however, the study of ion–ion collisions is still in its infancy and, furthermore, most studies focused on collisions between atomic ions. A few experiments (e.g. [6, 7]) have involved collisions of molecular ions with negative atomic ions. On the other hand, in the last few years charge transfer between highly charged ions and neutral molecules has attracted increasing interest as it gives detailed insight into both the electronic processes involved during the collision and the dynamics of the molecular fragmentation afterwards. H_2 molecules especially, have received particular attention [8–10] due to the relative simplicity of their electronic structure [11]. However, despite its simplicity the neutral H_2 molecule is still a two-electron system with all its inherent theoretical difficulties.

Using the well established technique of crossed ion–ion beams [12], we have measured, for the first time, total cross sections for charge transfer between two positive ions, where one collision partner is a molecular ion. In particular, we have studied the following collision systems

$$H_2^+ + He^{2+} \rightarrow H^+ + H^+ + He^+ \quad (1)$$

$$H_2^+ + Ar^{2+} \rightarrow H^+ + H^+ + Ar^+ \quad (2)$$

at centre-of-mass energies E_{cm} ranging from 16.5 keV $\leqslant E_{cm} \leqslant$ 57.6 keV and 39.3 keV $\leqslant E_{cm} \leqslant$ 82.9 keV respectively. The first collision system especially, is of general interest, as it is a pure one-electron system, with the electron moving in the potential of three bare positive charges. Such prepared systems can be studied experimentally only using ion–ion collisions.

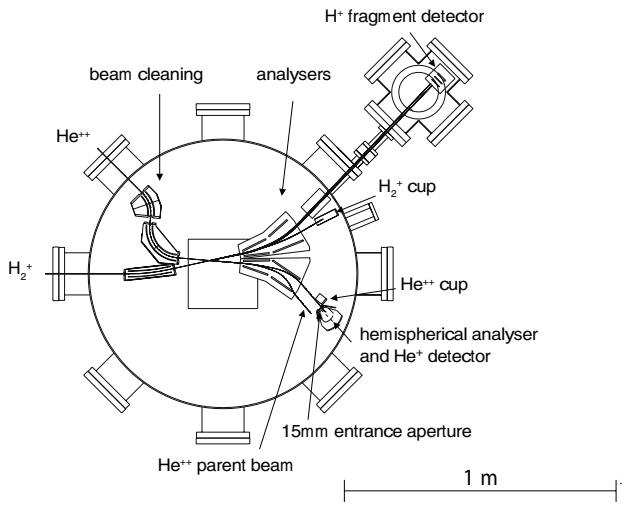

Figure 1. Experimental set-up and beam trajectories for the collision $H_2^+ + He^{2+} \rightarrow H^+ + H^+ + He^+$.

The experiments have been performed using the ion–ion crossed-beams facility at the University of Giessen [13]. The H_2^+ beam from a 10 GHz ECR source with energies in the range 50–130 keV (fast beam) is crossed with the beam of He^{2+} (Ar^{2+}) ions from a 5 GHz ECR source at 10 keV energy (slow beam) at an angle of $\beta = 17.5^\circ$ (figure 1). Both beams are cleaned by electrostatic analysers just before entering the interaction region with a vacuum of 10^{-10} mbar or below. Electrostatic analysers behind the interaction region separate the reaction products from the parent beams. The H^+ fragments are detected using a position sensitive micro channel plate (MCP) detector with 40 mm active diameter and delay line readout. The He^+ (Ar^+) product ions are further deflected by a hemispherical analyser out of the reaction plane and detected in a channeltron-based single-particle detector. Using the time coincidence technique for signal recovery the true reaction rate R is obtained. The absolute cross section is then given by [12]

$$\sigma = \frac{R}{\epsilon_1 \epsilon_2} \frac{v_1 v_2 \sin\beta}{v_{\mathrm{rel}}} \frac{q_1 q_2}{I_1 I_2} F \tag{3}$$

with the initial ion charge states q_1 and q_2, velocities v_1 and v_2 and the relative velocity v_{rel}. Here ϵ_1 and ϵ_2 denote the detector efficiencies, with the efficiency for the channeltron detector being 86% [14]. The single particle detection efficiency of the MCP detector is 60% [15]. Thus the probability to detect at least one of the two fragments is 84%. The intensity I_1 of the H_2^+ beam was continuously measured with a Faraday cup and was typically of the order of 50–100 nA. The intensity I_2 of the slow beam was typically 40–50 nA for He^{2+} and 190–200 nA for Ar^{2+}. As can be seen from figure 1, the Faraday cup was not suited to measure the parent He^{2+} (Ar^{2+}) beam current with the reaction products going to the channeltron detector. I_2 was therefore measured directly before and after a cross section measurement, with differences between these two measurements being typically 5% or less. The form factor F describes the vertical overlap of the two crossed ion beams. It is measured by vertically scanning both beams with a horizontal slit of 0.16 mm height. The form factor is also measured once before and once after the cross section measurement.

The resonant reactions $He^+ + He^{2+} \rightarrow He^{2+} + He^+$ and $Ar^+ + Ar^{2+} \rightarrow Ar^{2+} + Ar^+$ have been used to set up the electrostatic analysers and verify the cross section measurement. The cross

sections obtained from equation (3) however are smaller by a factor 1.74 ± 0.2 and 1.72 ± 0.2 respectively than those measured by Melchert *et al* [16] and Chen *et al* [3], which agree very well with theory. We attribute this discrepancy to an efficiency loss due to the aperture of the hemispherical analyser for the slow beam. Currently, the set-up is optimized to study charge exchange by multiply charged ions with the slow beam losing an electron. In the present experiment however, the slow beam is capturing the electron. In figure 1, the trajectories show that the He^+ product ions enter the hemispherical analyser at a non-negligible angle near the edge. Shown in the figure as well is the path of the parent He^{2+} ion beam, which passes very close to the edge when it exits the parallel plate analyser. Thus the analyser setting is critical to ensure the collection of all the reaction products but maintaining a tolerable background rate in the channeltron detector. The optimum analyser setting is obtained by measuring the cross section as a function of analyser voltage and then choosing values such that the cross section is maximized and independent of small variations of voltage. The energy and position of the slow beam are not changed during the measurements and we thus scale our cross sections obtained by equation (3) with 1.74 for $H_2^+ + He^{2+}$ and 1.72 for $H_2^+ + Ar^{2+}$. This problem does not arise for the fast beam as its position is directly visible on the MCP detector. The resulting cross sections are shown in figure 2.

We also calculated cross sections for electron capture in the systems H_2^++He^{2+} and H_2^++Ar^{2+} following a model for electron transfer in ion–molecule collisions proposed by Shingal and Lin [17]. Within this model, the molecular target initial state wavefunction is obtained through a linear combination of atomic orbitals (LCAO)

$$\Psi_i = \frac{1}{\sqrt{2}}\{u_{1s}(\vec{r}_A) + u_{1s}(\vec{r}_B)\} \tag{4}$$

where $u_{1s}(\vec{r})$ are hydrogenic wavefunctions on each centre. The electron capture amplitude, a_{fi}, can then be decomposed into two coherent contributions from each target centre

$$a_{fi} = \frac{1}{\sqrt{2}}\left\{A(\vec{b}_A) + A(\vec{b}_B)\exp\left[-\imath\rho\cos(\theta)\left(\frac{v_{rel}}{2} - \frac{\epsilon_f - \epsilon_i}{v_{rel}}\right)\right]\right\} \tag{5}$$

where ρ is the internuclear separation, θ is the alignment angle of the molecular axis with respect to the projectile beam direction, v_{rel} is the relative velocity between target and projectile, and $\epsilon_{i,f}$ are the initial and final state energies. $A(\vec{b})$ is the atomic scattering amplitude with impact parameters $\vec{b}$. The impact parameters $\vec{b}_A$ and $\vec{b}_B$ are measured relative to the two atomic centres in the molecular calculation. The LCAO wavefunction (equation (4)) with atomic hydrogen wavefunctions does not reproduce the H_2^+ ground-state potential very well for small internuclear separations. In particular the united atom limit, He^+, is not represented correctly. As a remedy to that, one can use hydrogenic wavefunctions, allowing the effective charge to vary with ρ [18]. The effective charge is then determined by applying the variational principle to the ground-state energy at each ρ . At the equilibrium separation, $\rho_0 = 2$ au, the resulting effective charge is $q_{eff} = 1.25$, which is what we used to model the H_2^+ target. The electronic ground-state energy is -1.1 au, which is the amount of energy needed to ionize $H_2^+ \rightarrow H^+ + H^+ + e^-$ with the protons frozen at a separation of $\rho = 2$ au. The atomic scattering amplitudes $A(\vec{b})$ were obtained through a close coupling calculation with atomic basis functions [19]. For both reactions (1) and (2), we used a hydrogenic atomic target with $q_{eff} = 1.25$, in its 1s ground state. In reaction (1), the He^{2+} projectile was described by a Coulomb potential with charge $Z = 2$. States up to $n = 3$ were included. The calculation shows that the electron is predominantly captured into He^+ ($n = 2$). In reaction (2), a model potential was used to describe the Ar^{2+} projectile [3] and only capture into Ar^+(3p) was assumed. These atomic-capture amplitudes were then added coherently, according to equation (5), for two scattering

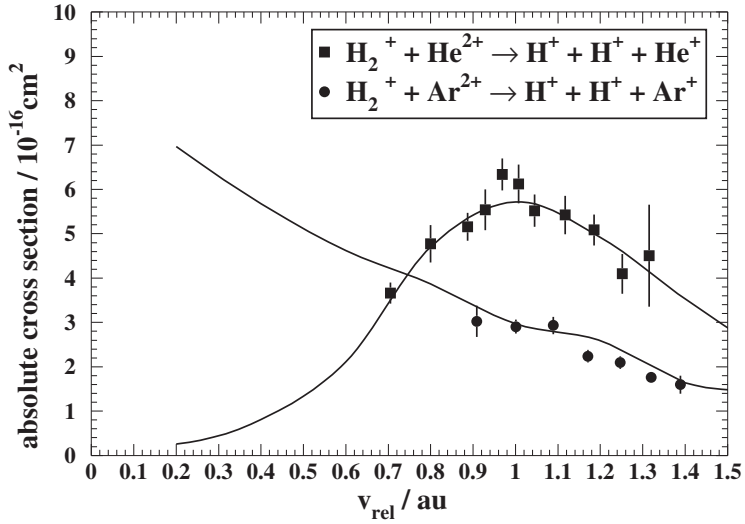

Figure 2. Absolute cross sections for the charge transfer reaction $H_2^+ + He^{2+} \rightarrow H^+ + H^+ + He^+$ (full squares) and $H_2^+ + Ar^{2+} \rightarrow H^+ + H^+ + Ar^+$ (full circles) versus relative collision velocity v_{rel}. The symbols show the experimental data with the error bars indicating the statistical error only. The full curves give the result of the theoretical calculations.

centres at a distance of $\rho = 2$ au. To compare with the experimental data, the resulting cross sections were averaged over all molecular orientations.

Figure 2 shows the measured and the theoretical cross sections for the collision system $H_2^+ + He^{2+}$ as a function of the relative velocity. The error bars represent the statistical error only. The systematic uncertainty includes the uncertainty in the scaling factor (12%), the uncertainty in the kinematic factor $v_1 v_2 \sin\beta / v_{rel}$ (8%) and in the MCP efficiency of about 15%. The systematic uncertainties of the form factor and beam current measurements can be neglected. The resulting overall uncertainty in absolute scale is 21%.

The cross section shows a distinct maximum around $v_{rel} = 1$ au and drops significantly towards higher and lower velocities. The velocity range accessible to the experiment is limited at the lower end by the energy released in the Coulomb breakup of the molecule. For the point with the lowest relative velocity shown, the fragments almost fill the complete detector area. The dependence of the cross section on v_{rel} as well as the absolute value is very well reproduced by the theory.

Also shown in figure 2 are the measured and theoretical cross sections for the collision system $H_2^+ + Ar^{2+}$. Again only the statistical errors are shown. In contrast to the $H_2^+ + He^{2+}$ system, no maximum can be seen in the experimental data. As for the collision with He^{2+} the theory agrees very well with the experiment. The difference in dependence on v_{rel} can be readily explained by the different Q values. In both cases, the H_2^+ ionization potential E_{ion} is 29.9 eV (see above). In reaction (1), the main capture channel is He^+ ($n = 2$) with an ionization potential of 13.6 eV, resulting in a rather large Q value of -16.3 eV. In reaction (2), with the Ar^+(3p) ionization potential of 27.6 eV, the Q value is only -2.3 eV. The latter system is thus closer to a resonant charge transfer. This results in a shift of the maximum of the cross section towards smaller relative velocities.

To conclude, we have presented absolute cross sections for charge transfer in collisions of H_2^+ molecules with He^{2+} and Ar^{2+} ions. The experimental data can be described very well theoretically by using a coherent superposition of two single-electron-capture amplitudes in ion–atom collisions. The theoretical calculations can also predict differential cross sections with respect to the alignment of the molecular ion. Future measurements of such differential cross sections will provide a much more stringent test for theory.

The authors would like to thank Chii-Dong Lin for helpful discussions. This work was supported by Deutsche Forschungsgemeinschaft (DFG) and the Chemical Sciences, Geosciences and Biosciences Division, Office of Basic Energy Sciences, Office of Science, US Department of Energy. HB gratefully acknowledges support from the Alexander von Humbold foundation.

References

[1] Rinn K, Melchert F and Salzborn E 1985 *J. Phys. B: At. Mol. Opt. Phys.* **18** 3783
[2] Krüdener S, Melchert F, von Diemar K, Pfeiffer A, Huber K, Salzborn E, Uskov D and Presnyakov L 1997 *Phys. Rev. Lett.* **79** 1002
[3] Chen C Y, Cocke C L, Giese J P, Melchert F, Reiser I, Stöckli M, Sidky E and Lin C D 2001 *J. Phys. B: At. Mol. Opt. Phys.* **34** 469
[4] Skiera D, Trassl R, Huber K, Bräuning H, Salzborn E, Keim M, Achenbach A, Kircher T, Lüdde H J and Dreizler R M 2001 *Physica Scripta* in print
[5] Melchert F, Pfeiffer A, von Diemar K, Bajajova K, Wohlfahrt C and Salzborn E 1998 *Nucl. Instrum. Methods* A **415** 566
[6] Naji A, Olamba K, Chenu J, Szücs S and Brouillard F 1998 *J. Phys. B: At. Mol. Opt. Phys.* **31** 4887
[7] Padgett R and Peart B 1998 *J. Phys. B: At. Mol. Opt. Phys.* **31** L995
[8] McLaughlin T, McCullough R and Gilbody H 1992 *J. Phys. B: At. Mol. Opt. Phys.* **25** 1257
[9] Hoekstra R, Folkerts H, Beijers J, Morgenstern R and de Heer F 1994 *J. Phys. B: At. Mol. Opt. Phys.* **27** 2021
[10] Fremont F, Bedouet C, Tarisien M, Adoui L, Cassimi A, Dubois A, Chesnel J-Y and Husson X 2000 *J. Phys. B: At. Mol. Opt. Phys.* **33** L249
[11] Errea L, Gorfinkiel J, Macias A, Mendez L and Riera A 1999 *J. Phys. B: At. Mol. Opt. Phys.* **32** 1705
[12] Melchert F and Salzborn E 2000 *The Physics of Electronic and Atomic Collisions* (*Sendai, Japan 1999*) ed Y Itikawa (New York: AIP) pp 478–94
[13] Meuser S, Melchert F, Krüdener S, Pfeiffer A, von Diemar K and Salzborn E 1996 *Rev. Sci. Instrum.* **67** 2752
[14] von Diemar K 1998 Untersuchungen des Elektroneneinfangs in Stößen zwischen mehrfach geladenen Ionen *PhD thesis* Univ. Giessen, Germany
[15] Krüdener S 1992 Winkeldifferentielle Messungen in Cs^+–Cs^+ Stößen *PhD thesis* Univ. Giessen, Germany
[16] Melchert F, Krüdener S, Schulze R, Petri S, Pfaff S and Salzborn E 1995 *J. Phys. B: At. Mol. Opt. Phys.* **28** L355
[17] Shingal R and Lin C 1989 *Phys. Rev.* A **40** 1302
[18] Lowe J P 1993 *Quantum Chemistry* (New York: Academic)
[19] Fritsch W and Lin C 1991 *Phys. Rep.* **202** 1

Appendix B

Two Dimensional Linear Least Squares Fitting

The two dimensional least square fitting is a generalization of the method described in [44] to two dimensions. Instead of sets of data points (x_i, x'_i), sets of two-dimensional vectors $(\vec{x}_i, \vec{x}'_i)$ with $\vec{x} = (x, y)$ and $\vec{x}' = (x', y')$ are fit to a model which is represented through the basis functions $\Phi_j(\vec{x})$, $j = 1 \ldots M$. M is the number of basis functions.

The new data $\vec{x}'$ is expanded in terms of basis functions:

$$\vec{x}'(\vec{x}) = \sum_{k=1}^{M} \vec{a}_k \Phi_k(\vec{x}) \tag{B.1}$$

The vector $\vec{a}_k$ is the coefficient vector, $\vec{a} = (a, b)$. The problem is now to find this coefficient vector. In order to do this, one defines a "design matrix" A as

$$A = \begin{pmatrix} \Phi_1(x_1, y_1) & \Phi_2(x_1, y_1) & \ldots & \Phi_M(x_1, y_1) \\ \Phi_1(x_2, y_2) & \Phi_2(x_2, y_2) & \ldots & \Phi_M(x_2, y_2) \\ \vdots & \vdots & & \vdots \\ \Phi_1(x_N, y_N) & \Phi_2(x_N, y_N) & \ldots & \Phi_M(x_N, y_N) \end{pmatrix} \tag{B.2}$$

This is a $N \times M$ rectangular matrix where N is the number of data sets to be included in the fit, and M is the number of basis functions. A necessary condition is that N≥M. With this, equation B.1 can then be written as a matrix equation

$$\vec{x}' = A \cdot \vec{a} \ . \tag{B.3}$$

Transforming the right hand side into a square matrix,

$$A^T \cdot \vec{x}' = \underbrace{A^T A}_{\text{square matrix}} \vec{a} \tag{B.4}$$

allows to solve for the coefficient vector $\vec{a}$ through

$$\vec{a} = [A^T A]^{-1} A^T \cdot \vec{x}' \quad . \tag{B.5}$$

In our problem, we choose 10 basis functions, which are polynomials up to third order,

$$\begin{aligned}
\Phi_0 &= 1 \\
\Phi_1 &= x \\
\Phi_2 &= x^2 \\
\Phi_3 &= x^3 \\
\Phi_4 &= y \\
\Phi_5 &= y^2 \\
\Phi_6 &= y^3 \\
\Phi_7 &= xy \\
\Phi_8 &= x^2 y \\
\Phi_9 &= xy^2
\end{aligned}$$

and at least N=51 datasets are used the evaluation of the coefficients.

Appendix C

Position maps

The following figures show detector images of voltage grids which were used to transform detector position into deflector voltage. From those, the tables on pages 125 through 127 were derived. The data in the columns was used for the two-dimensional least squares fitting derived in appendix B. u_x and u_y are the "new data $\vec{x}'$. x^{map} and y^{map} are the data $\vec{x}$ used to create the design matrix A. The coefficients derived from the fit, which are used to calibrate the detector positions, are listed in table C.4. Note that the detector is rotated by 27° with respect to the laboratory vertical and horizontal, which appears in the raw voltage grid images.

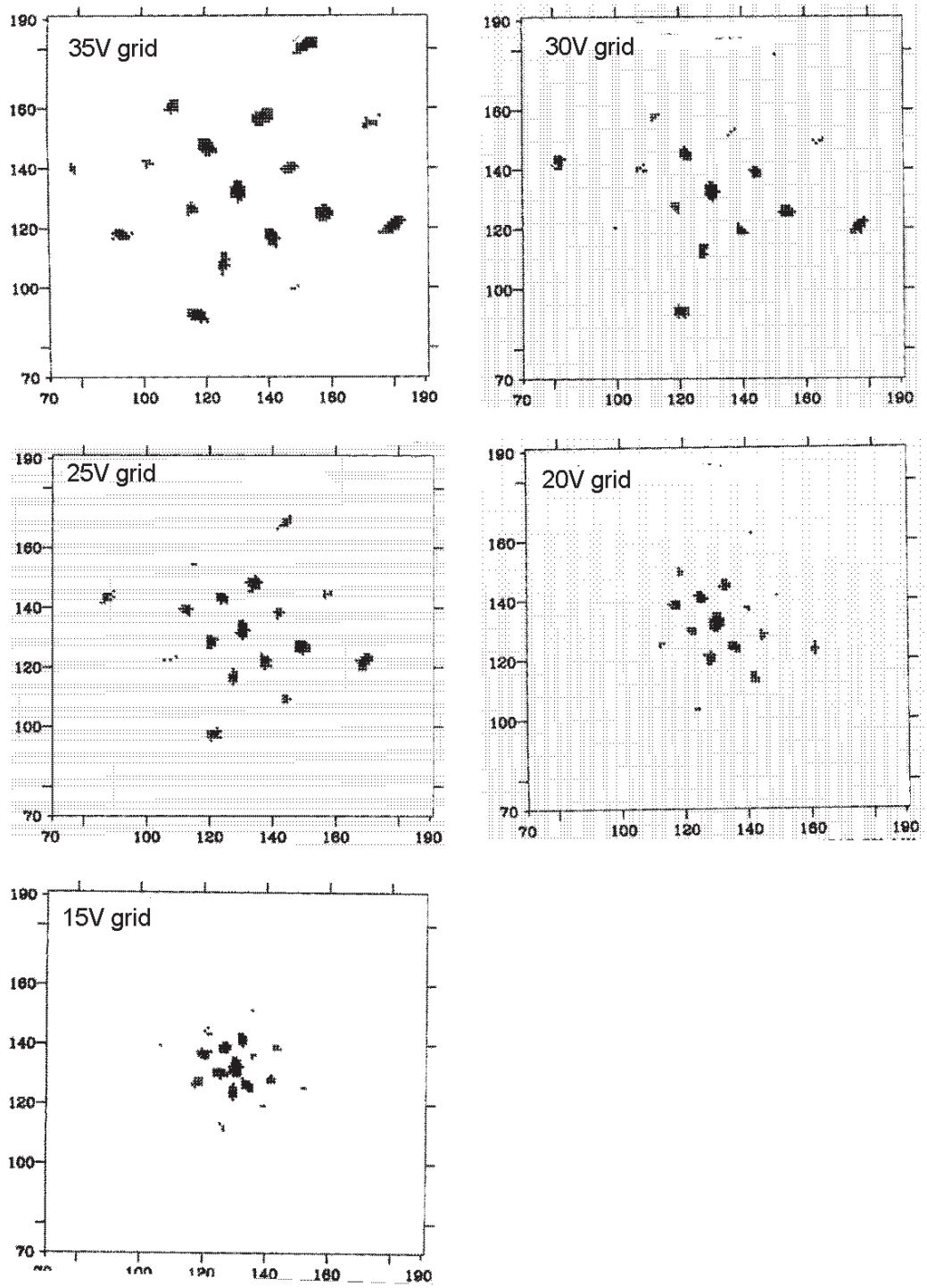

Figure C.1: *Detector image of the voltage grids used to calibrate the Ar^{2+} runs.*

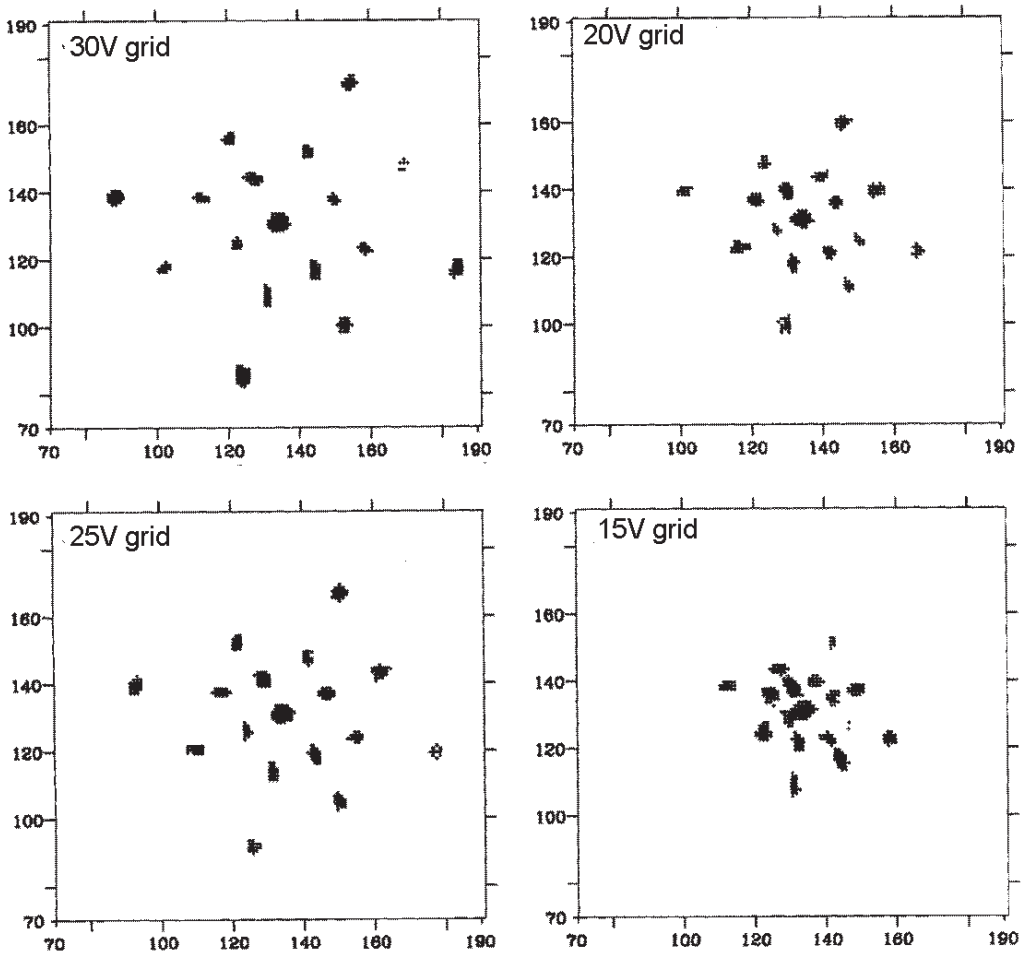

Figure C.2: *Detector image of the voltage grids used to calibrate the N^{2+} runs.*

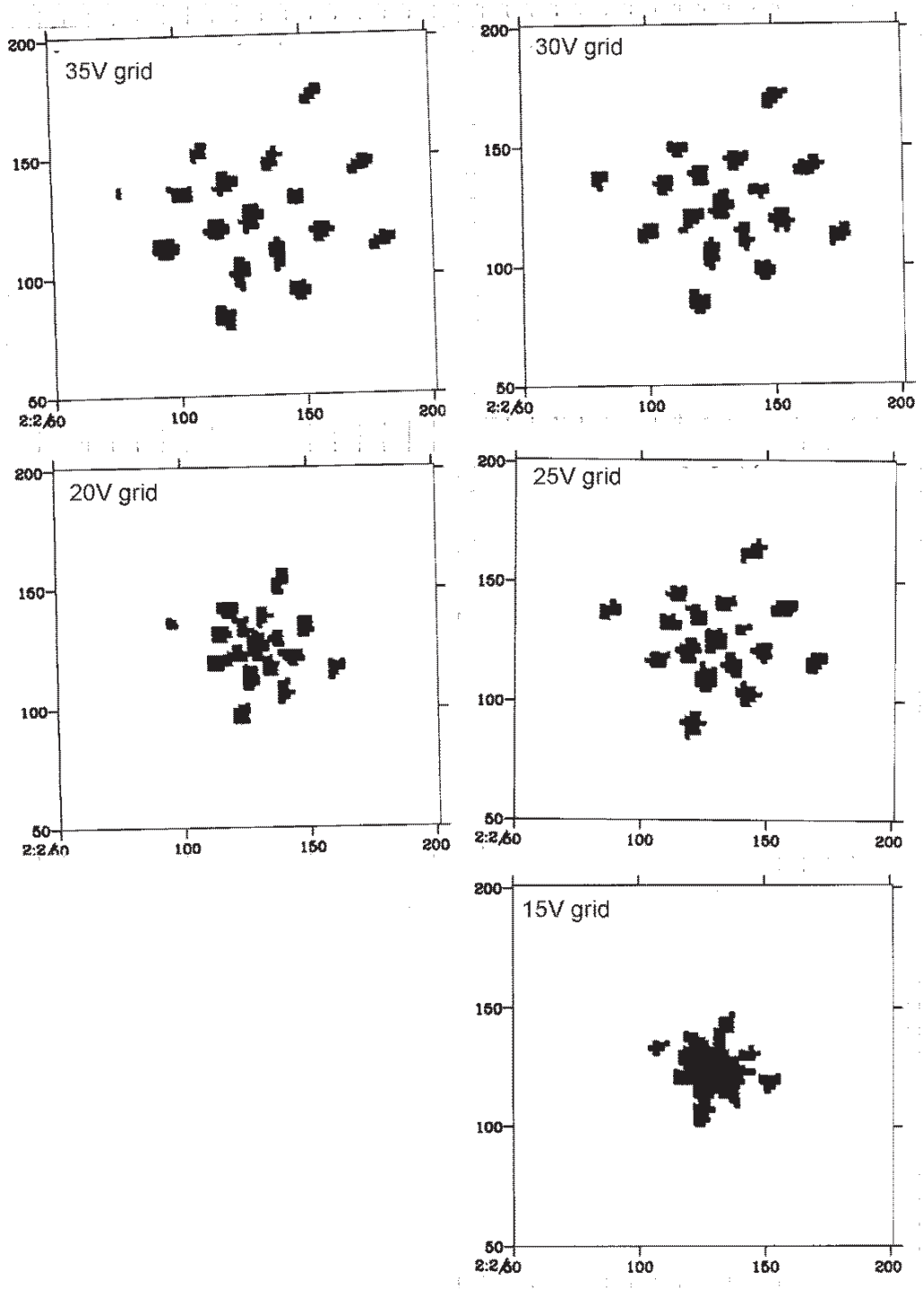

Figure C.3: *Detector image of the voltage grids used to calibrate the He^{2+} runs.*

u_x	u_y	x^{map}	y^{map}	u_x	u_y	x^{map}	y^{map}
-35	-35	-52	10	12.5	0	11	8
0	-35	-20	31	25	0	26	14
35	-35	22	51	-12.5	12.5	-3	-14
-17.5	-17.5	-25	11	0	12.5	7	-8
0	-17.5	-10	17	12.5	12.5	19	-3
17.5	-17.5	8	27	-25	25	-9	-33
-35	0	-37	-13	0	25	14	-21
-17.5	0	-14	-4	25	25	39	-8
0	0	0	2	-20	-20	-33	12
17.5	0	17	10	0	-20	-12	19
35	0	41	24	20	-20	11	31
-17.5	17.5	-5	-22	-10	-10	-13	8
0	17.5	11	-13	0	-10	-5	10
17.5	17.5	28	-6	10	-10	3	14
-35	35	-13	-40	-20	0	-18	-5
0	35	18	-31	-10	0	-8	-1
35	35	49	-10	10	0	10	7
-30	-30	-50	12	20	0	19	11
0	-30	-18	27	-10	10	-2	-10
30	-30	20	47	0	10	5	-6
-15	-15	-23	10	10	10	15	-2
0	-15	-8	14	-20	20	-6	-27
15	-15	6	22	0	20	12	-16
-30	0	-31	-10	20	20	31	-7
-15	0	-12	-3	-15	-15	-24	9
15	0	14	9	0	-15	-9	14
30	0	34	19	15	-15	5	21
-15	15	-3	-18	-7.5	-7.5	-10	7
0	15	9	-11	0	-7.5	-4	8
15	15	24	-5	7.5	-7.5	2	11
-30	30	-11	-38	-15	0	-12	-3
0	30	16	-27	-7.5	0	-5	0
30	30	46	-9	7.5	0	6	6
-25	-25	-43	13	15	0	13	8
0	-25	-15	24	-7.5	7.5	-1	-7
25	-25	13	38	0	7.5	4	-4
-12.5	-12.5	-18	9	7.5	7.5	11	-2
0	-12.5	-7	13	-15	15	-4	-18
12.5	-12.5	4	18	0	15	8	-11
-25	0	-23	-8	15	15	22	-5
-12.5	0	-10	-2				

Table C.1: *Ar detector calibration*

u_x	u_y	x^{map}	y^{map}	u_x	u_y	x^{map}	y^{map}
30	-30	-46	7	-12.5	0	12	6
0	-30	-14	24	-25	0	28	12
-30	-30	20	41	12.5	12.5	-3	-18
15	-15	-22	7	0	12.5	9	-12
0	-15	-7	12	-12.5	12.5	20	-7
-15	-15	8	20	25	25	-9	-40
30	0	-32	-14	0	25	15	-26
15	0	-12	-7	-25	25	43	-12
0	0	0	0	20	-20	-33	8
-15	0	15	6	0	-20	-10	16
-30	0	35	16	-20	-20	12	28
15	15	-4	-22	10	-10	-13	5
0	15	10	-14	0	-10	-4	8
-15	15	24	-8	-10	-10	6	13
30	30	-11	-46	20	0	-18	-9
0	30	18	-32	10	0	-7	-4
-30	30	50	-14	0	0	0	0
25	-25	-41	8	-10	0	10	5
0	-25	-13	21	-20	0	21	8
-25	-25	16	36	10	10	-3	-13
12.5	-12.5	-17	6	0	10	7	-10
0	-12.5	-5	10	-10	10	16	-7
-12.5	-12.5	7	16	20	20	-5	-32
25	0	-24	-11	0	20	13	-21
12.5	0	-10	-5	-20	20	32	-10

Table C.2: *N detector calibration*

u_x	u_y	x^{map}	y^{map}	u_x	u_y	x^{map}	y^{map}
0	-35	-21	22	12.5	0	10	-1
35	-35	24	46	25	0	26	9
-17.5	-17.5	-29	6	-12.5	12.5	-4	-20
0	-17.5	-11	9	0	12.5	6	-15
17.5	-17.5	7	18	12.5	12.5	18	-9
-35	0	-36	-18	-25	25	-10	-40
-17.5	0	-15	-10	0	25	13	-28
0	0	0	-5	25	25	40	-14
17.5	0	17	3	-20	-20	-34	5
35	0	42	16	0	-20	-12	11
-17.5	17.5	-6	-28	20	-20	9	23
0	17.5	9	-20	-10	-10	-15	1
17.5	17.5	27	-12	0	-10	-7	5
-35	35	-12	-48	10	-10	2	8
0	35	17	-36	-20	0	-17	-11
35	35	50	-16	-10	0	-8	-8
-30	-30	-49	7	10	0	8	-1
0	-30	-19	19	20	0	18	4
30	-30	20	40	-10	10	-3	-16
-15	-15	-23	4	0	10	5	-12
0	-15	-9	8	10	10	14	-9
15	-15	5	14	-20	20	-7	-33
-30	0	-31	-16	0	20	10	-22
-15	0	-13	-9	20	20	30	-13
15	0	14	1	-15	-15	-23	3
30	0	33	11	0	-15	-9	8
-15	15	-4	-24	15	-15	5	13
0	15	8	-17	-7.5	-7.5	-11	0
15	15	22	-11	0	-7.5	-5	1
-30	30	-10	-46	7.5	-7.5	1	5
0	30	16	-32	-15	0	-13	-9
30	30	46	-16	-7.5	0	-7	-7
-25	-25	-43	7	7.5	0	6	-2
0	-25	-15	15	15	0	14	1
25	-25	15	33	-7.5	7.5	-2	-13
-12.5	-12.5	-18	2	0	7.5	3	-10
0	-12.5	-8	6	7.5	7.5	9	-8
12.5	-12.5	3	11	-15	15	-6	-25
-25	0	-24	-13	0	15	8	-17
-12.5	0	-11	-8	15	15	22	-10

Table C.3: *He detector calibration*

	Ar		N		He	
i	a_i	b_i	a_i	b_i	a_i	b_i
0	-1.83	1.79	0.854	-0.524	2.71	-3.7
1	0.853	0.362	-0.836	0.373	0.836	0.379
2	4.08E-4	6.65E-4	-2.61E-4	-4.07E-4	-8.467E-4	9.43E-4
3	-5.76E-5	3.54E-5	7.66E-5	1.45E-5	-5.83E-5	3.39E-6
4	0.568	-0.846	-0.508	-0.836	0.565	-0.892
5	4.23E-4	-4.65E-4	-1.06E-4	-0.00295	-1.4E-4	-0.00153
6	-3.68E-5	-1.55E-5	3.03E-5	-8.76E-6	-2.33E-5	-1.47E-5
7	-0.00333	0.00161	0.00197	0.00312	-0.00504	0.0022
8	-1.2E-4	-3.52E-5	1E-4	-4.95E-5	-9.13E-5	-4.91E-5
9	-3.53E-5	1.76E-5	5.97E-5	5.87E-5	-7.71E-5	9.15E-5

Table C.4: *Coefficients from the 2d linear least squares fit.*

Appendix D

Distortions of a Coulomb-sphere by Magnetic and Electric Fields

This section investigates the general features of a Coulomb-sphere that has traveled through a magnetic or an electrostatic field. The goal of this study is to qualitatively understand the features introduced by the fields, rather than to quantitatively reproduce the effects observed in the experiment. In the data reduction (see section 5.3), all ion optical elements in the apparatus are simulated in a more rigorous way, which allows to reproduce the experimentally observed distortions of the measured Coulomb-sphere. On the other hand, the somewhat more complex setup does not allow to investigate the cause of the distortions, which is done in this present section.

In the following, a Coulomb-sphere with molecular axes ($\vec{v}_{cs,x}$, $\vec{v}_{cs,y}$, $\vec{v}_{cs,z}$), travels along with the beam in the $\hat{z}$-direction. In the first section, the Coulomb-sphere travels through a magnetic field. The orientations of the molecular axes after exiting the field are determined. In the second section, the Coulomb-sphere passes an electric field. In both cases, the field lines point along the $\hat{y}$-direction.

D.1 Magnetic Analyzer

In this section, a Coulomb-sphere that travels through a magnetic field is studied. A beam traveling through a magnet is deflected by an angle away from the initial beam direction and perpendicular to both magnetic field and velocity direction. But how is the whole Coulomb-sphere affected by the magnetic field?

To answer this question, we calculated and simulated ion trajectories corresponding to a Coulomb-sphere whose center-of-mass is moving along with the beam. The beam velocity $\vec{v}_{beam}$ is initially along the $\hat{z}^{lab}$ direction (unit vector!), and the magnetic field lines are pointing in the $\hat{y}^{lab}$ direction. Initially, the Coulomb-sphere axes directions are such that $\vec{v}_{cs,z}$ is parallel to $\vec{v}_{beam}$ and $\vec{v}_{cs,x}$ is perpendicular to the magnetic field direction as well as to the beam direction. The velocity component parallel to the magnetic field lines is not affected by the field and is therefore left out of this analysis.

Fig. D.1 shows a SIMION simulation of a Coulomb-sphere traveling through a homogeneous magnetic field. The field lines are perpendicular to the plane shown. After the sphere exits the magnetic field, $\vec{v}_{cs,z}$ is no longer parallel to the beam direction, and is no longer perpendicular to $\vec{v}_{cs,x}$. Furthermore, those angles are not constant, they evolve as the Coulomb-sphere moves along.

In the following, the time evolution of the axes directions is obtained through an analytic calculation and compared to the results of the SIMION simulation.

Trajectory calculation

Charged particles in a magnetic field are subject to the Lorentz force $\mathbf{F} = q\mathbf{v} \times \mathbf{B}$. Written in components, this equation reads, for a magnetic field $\mathbf{B}$ pointing along the

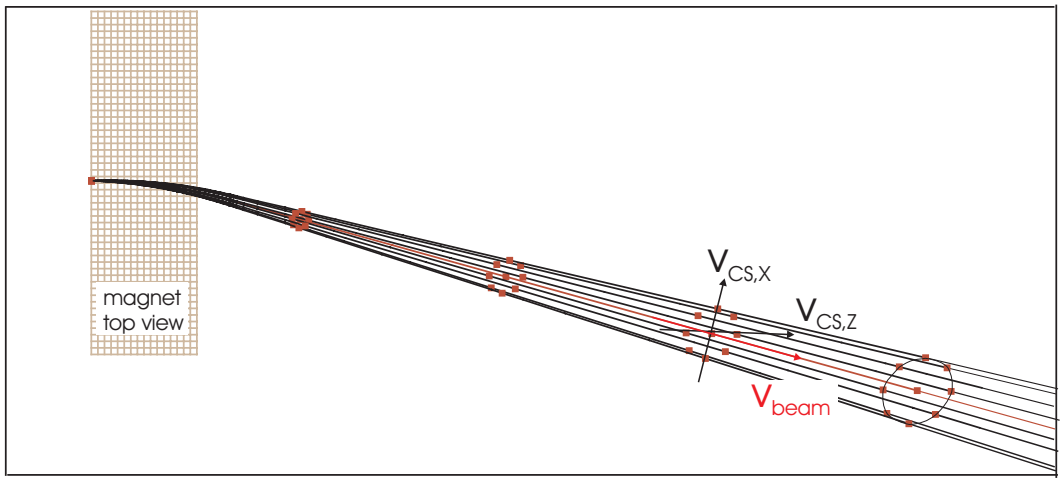

Figure D.1: *Ion trajectories from a SIMION simulation of a magnetic sector field. The magnetic field lines point out of the page.*

positive y-direction (the dots stands for d/dt)

$$\dot{v}_x = \frac{qB}{m} v_z; \qquad \dot{v}_z = -\frac{qB}{m} v_x \ . \tag{D.1}$$

The first order differential coupled equations in D.1 can be combined to give uncoupled 2nd order differential equations:

$$\ddot{v}_x = -\left(\frac{qB}{m}\right)^2 v_x; \quad \ddot{v}_z = -\left(\frac{qB}{m}\right)^2 v_z \ . \tag{D.2}$$

The particles enters the magnetic field region at $t = 0$. With the initial conditions $v_x(0) = v_{||}$ and $v_z(0) = v_\perp$ the solutions of the differential equations are

$$v_x = v_\perp \sin(\omega t) + v_{||} \cos(\omega t) \tag{D.3}$$

$$v_z = -v_{||} \sin(\omega t) + v_\perp \cos(\omega t) \tag{D.4}$$

$$\text{with} \quad \omega = \frac{qB}{m} \tag{D.5}$$

Integrating the velocities, one obtains the particle's position in the magnetic field as a function of time:

$$r_x(t) = (-v_\perp/\omega)\cos(\omega t) + (v_\parallel/\omega)\sin(\omega t) + v_\perp/\omega \tag{D.6}$$

$$r_z(t) = (v_\parallel/\omega)\cos(\omega t) + (v_\perp/\omega)\sin(\omega t) - v_\parallel/\omega \tag{D.7}$$

The coordinate system is chosen such that the origin is located at the particle's entrance into the magnetic field with x(0)=z(0)=0.

Since here $v_\perp \ll v_\parallel$, the time t_e at which the particle exits a magnetic field which extends from $x = 0$ to x=x_e is

$$t_e = \frac{x_e}{\sqrt{v_\parallel^2 + v_\perp^2}} \tag{D.8}$$

After exiting the magnetic field region, the particle continues on its trajectory at a constant velocity $\mathbf{v} = \mathbf{v}(t_e)$. The particle's position at a later time, $t > t_e$, is then given by

$$\mathbf{r}(t) = \mathbf{r}(t_e) + \mathbf{v}(t_e)(t - t_e) \tag{D.9}$$

So now we have the particle's position as a function of magnitude and spatial extension of the magnetic field, particle's initial parallel and perpendicular velocities, particle's mass and charge and, of course, as a function of time. The only potential problem may be that we chose the particle to enter the magnetic field at the coordinate origin.

In our apparatus, the analyzing magnet deflects the ion trajectories by 15° on a path with a radius of 24.12 inches = 0.61 m. For 4 keV deuterium ions this requires a magnetic field of 210 gauss and the pole length is 6.24 inches = 0.158 m. For this field, $\omega = 10^6$ Hz. This results in the following parameters to be used in the calculation: $v_\parallel = 6 \cdot 10^6$ m/s, $v_\perp = 2.4 \cdot 10^4$ m/s, $\omega = 10^6$ Hz, $x_e = 0.16$ m.

Results

As shown in Fig. D.1, the magnetic field deflects the mean ion beam direction by 15°. The Coulomb-sphere's velocity vectors, initially at $\alpha = 0°$ and $\alpha = 90°$ to the beam direction, are skewed. The time-evolution of the angles between the beam direction, $\vec{v}_{beam}$ and $\vec{v}_{cs,z}$ respective $\vec{v}_{cs,x}$, are shown in fig. D.2. The asymptotic values of the angles are tabulated in table D.1.

Asymptotically, the $\vec{v}_{cs,x}$ axis is again perpendicular to the beam direction, as prior to the magnetic field. In contrast, the $\vec{v}_{cs,z}$ axis, which was initially parallel to the beam direction, is at an angle, to the beam direction. This angle amounts to be close to the deflection angle, which means that the $\vec{v}_{cs,z}$ axis direction has not been affected by the field. Those results do not depend on the magnitude of the Coulomb velocity.

Conclusion

The magnetic field affects the Coulomb-sphere velocity axes, depending on the orientation of the axes with respect to the ion beam direction and the magnetic field direction.

- $\vec{v}_{cs,x}$ is perpendicular to both beam and magnetic field directions initially, and remains approximately so after exiting the field region.
- $\vec{v}_{cs,y}$ lies parallel to the magnetic field direction and thus is not affected by the magnetic field.
- $\vec{v}_{cs,z}$ is parallel to the ion beam direction when entering the field, but it is skewed after exiting the field region.

In our apparatus, the fragments impact onto the detector at about $t = 4 \times t_0$ after exiting the magnetic field.

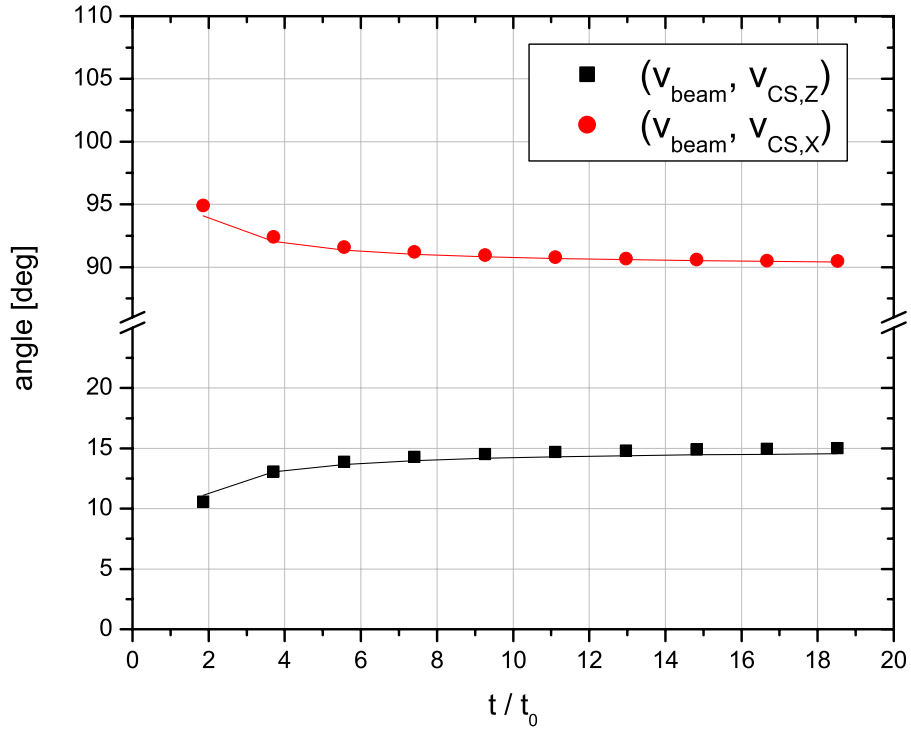

Figure D.2: *Time-evolution of the angles between beam direction and the internal velocities ($v_{cs,x}$, $v_{cs,z}$) of a Coulomb-sphere traveling through a magnetic field. The symbols are results from the SIMION simulation, the lines are the results of the analytical calculation. The sphere enters the magnetic field at t = 0 and exits at t=0.27 μs.*

angle between	t = 1 μs	t = 10 μ s	no field
$(\vec{v}_{beam}, \vec{v}_{cs,x})$	92.04	90.2	90.0
$(\vec{v}_{beam}, \vec{v}_{cs,z})$	13.04	14.74	0.0
$(\vec{v}_{cs,x}, \vec{v}_{cs,z})$	79.0	75.42	90.0

Table D.1: *Angles (in degrees) between beam- and internal velocities of a Coulomb-Sphere traveling through a magnetic field, at 1μs and 10μs after entering a magnetic field (it takes 0.27μs to traverse the field region). The last column shows the angles if the Coulomb sphere had not traveled through a field region.*

D.2 Electrostatic Analyzer

A Coulomb-sphere that traveled through an electrostatic field exhibits qualitatively similar features as when traveling through a magnetic field (section D.1): the velocity axes of the Coulomb-sphere are skewed upon exiting the field region.

Trajectory Simulation Results

Fig. D.3 shows the SIMION trajectory simulation of a Coulomb-sphere traveling through a 20° cylindric electrostatic analyzer at a field of 2 V/cm. The beam energy is $E_{beam} = 1500$ eV, the Coulomb-explosion energy is E_{Coul}=6 eV. The angles between the beam direction and the molecular velocity axes are plotted in fig. D.4 as a function of ion flight time. t_0 is the time it takes the fragments to traverse the analyzer. In our apparatus, the fragments reach the detector at about $t = 2 \times t_0$.

Conclusion

For the electrostatic analyzer, the main conclusion is that the initial Coulomb-sphere's axes orientations are conserved over a short range after exiting the analyzer. In our experimental setup, the ions arrive at the detector at about $t = 2t_0$, where t_0 is the time it takes to traverse the analyzer. Since the mean ion beam direction is deflected after traversing the electrostatic deflector, both internal axes of the Coulomb-sphere are rotated with respect to the beam direction v_{beam}.

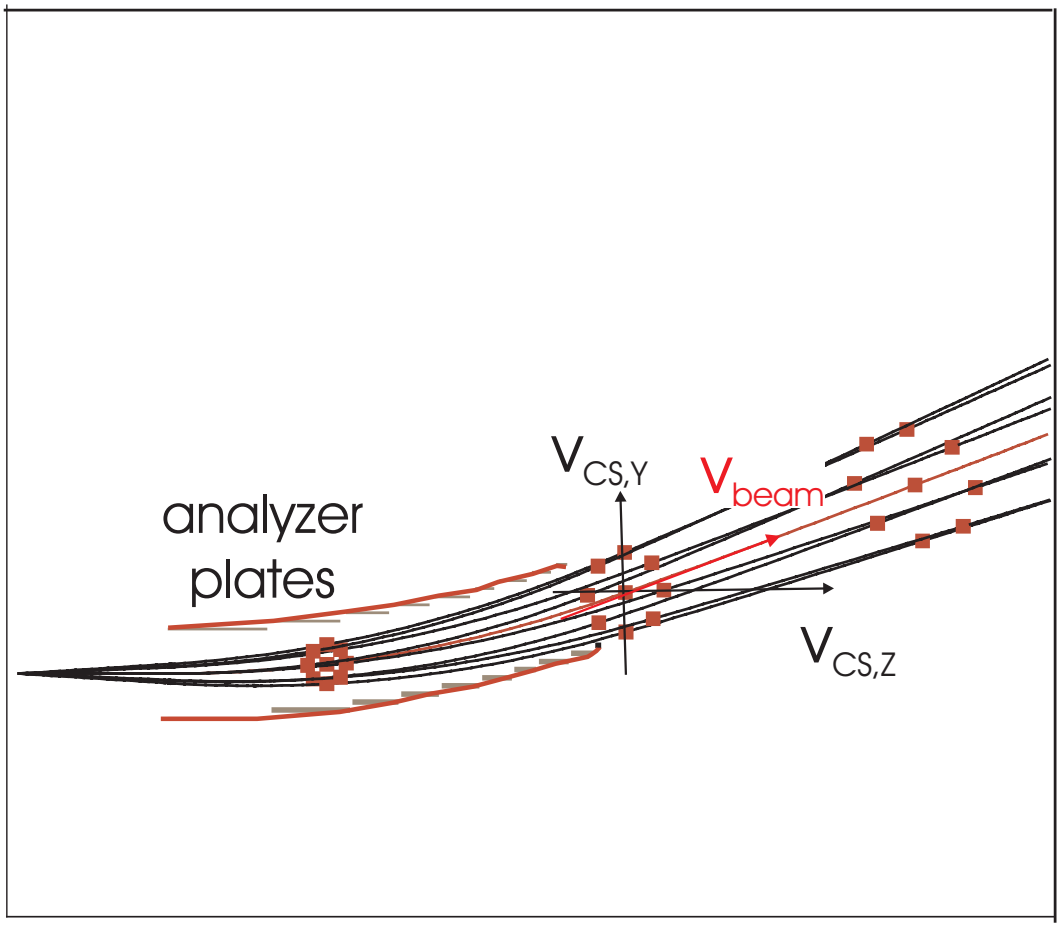

Figure D.3: *Ion trajectories from a SIMION simulation of 20° cylindrical electrostatic analyzer*

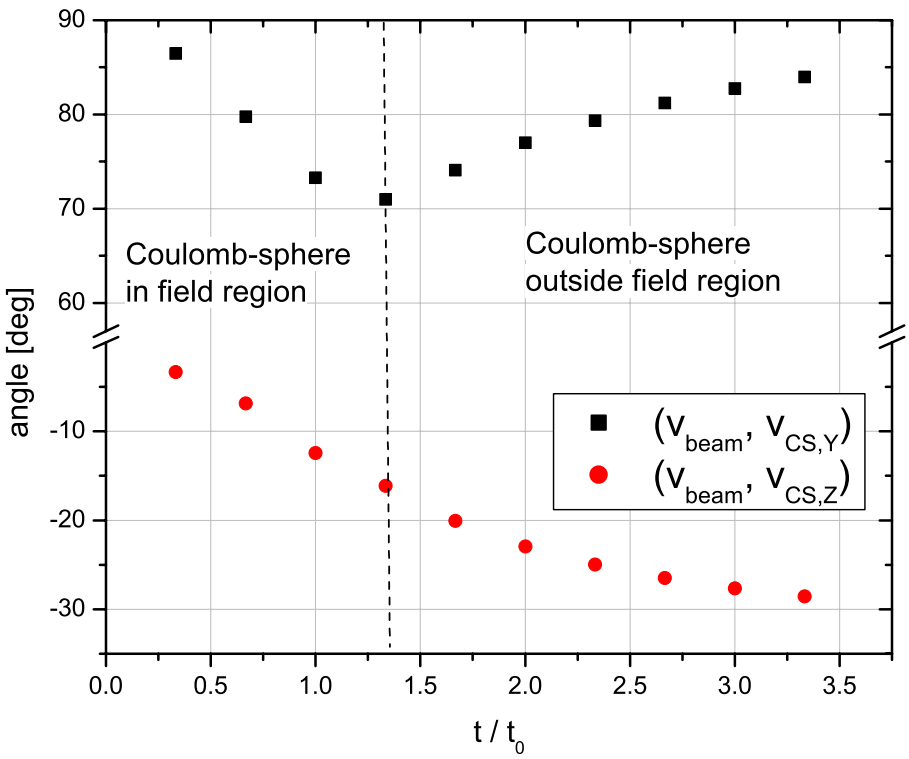

Figure D.4: *Time-evolution of the molecular axes directions of a Coulomb-Sphere after passing a cylindrical electrostatic analyzer.*

Appendix E

Data Analysis Software

Following are listings of the ionion.com, ionion.evl and routines.for files used in the data analysis.

```
$!  *************          IONION.COM          ****************************
$!  **      COM FILE FOR ION-MOLECULAR-ION COLLISION EXPERIMENTS      *****
$!  **           WITH BOTH BACKGAMMON AND DELAY LINE ANODE            *****
$!  **                          ingrid reiser                         *****
$!  **                  last modified 23.  MAERZ 2000                 *****
$!  *****                                                           ********
$!-------------------------------------------------------------------
$dmem all global file
$amem new 30000 pages*
$!--------------- ECR 2D-BACKGAMMON POSITION SENSITIVE DETECTOR --
$amem 1 ECRSX R*4 2048
$amem 2 ECRSY R*4 2048
$amem 3 ECRSR R*4 2048
$amem 4 ECRSUM R*4 2048
$amem 5 ECRXY I*4 256 256
$!--------------- EBS 2D DELAY LINE DETECTOR ----------
$!  ** FIRST HIT **
$AMEM 10 H1X1 8192
$AMEM 11 H1X2 8192
$AMEM 12 H1Y1 8192
$AMEM 13 H1Y2 8192
$AMEM 14 H1XSUM 8192
$AMEM 15 H1YSUM 8192
$AMEM 16 H1XPOS R*4 8192
$AMEM 17 H1YPOS R*4 8192
$AMEM 18 H1XYPOS R*4 256 256
$!  ** SECOND HIT **
$AMEM 20 H2X1 8192
$AMEM 21 H2X2 8192
$AMEM 22 H2Y1 8192
$AMEM 23 H2Y2 8192
$AMEM 24 H2XSUM 8192
$AMEM 25 H2YSUM 8192
$AMEM 26 H2XPOS R*4 8192
$AMEM 27 H2YPOS R*4 8192
$AMEM 28 H2XYPOS R*4 256 256
$!--------------- gated events ---------------------------
$AMEM 181 H1XYBG R*4 256 256
$AMEM 182 H1XYPEAK R*4 256 256
$AMEM 183 H1XYTRUE R*4 256 256
$AMEM 281 H2XYBG R*4 256 256
$AMEM 282 H2XYPEAK R*4 256 256
$AMEM 283 H2XYTRUE R*4 256 256
$AMEM 301 FRXYBG R*4 256 256
$AMEM 302 FRXYPEAK R*4 256 256
$AMEM 303 FRXYTRUE R*4 256 256
$AMEM 311 FRXTBG R*4 256 256
$AMEM 312 FRXTPEAK R*4 256 256
$AMEM 313 FRXTTRUE R*4 256 256
$AMEM 321 FRYTBG R*4 256 256
$AMEM 322 FRYTPEAK R*4 256 256
```

```
$AMEM 323 FRYTTRUE R*4 256 256
$!------------ SLICES --------------
$AMEM 33 THETA R*4 256
$AMEM 34 FRY R*4 256
$AMEM 331 XYSLBG R*4 256 256
$AMEM 332 XYSLPEAK R*4 256 256
$AMEM 333 XYSLTRUE R*4 256 256
$AMEM 341 XTSLBG R*4 256 256
$AMEM 342 XTSLPEAK R*4 256 256
$AMEM 343 XTSLTRUE R*4 256 256
$AMEM 351 YTSLBG R*4 256 256
$AMEM 352 YTSLPEAK R*4 256 256
$AMEM 353 YTSLTRUE R*4 256 256
$!------------ RHOPHI --------------
$AMEM 361 XYRPBG R*4 256 256
$AMEM 362 XYRPPEAK R*4 256 256
$AMEM 363 XYRPTRUE R*4 256 256
$AMEM 371 XTRPBG R*4 256 256
$AMEM 372 XTRPPEAK R*4 256 256
$AMEM 373 XTRPTRUE R*4 256 256
$AMEM 381 YTRPBG R*4 256 256
$AMEM 382 YTRPPEAK R*4 256 256
$AMEM 383 YTRPTRUE R*4 256 256
$!---------- CM ---------------------
$AMEM 401 CMXYBG R*4 256 256
$AMEM 402 CMXYPEAK R*4 256 256
$AMEM 403 CMXYTRUE R*4 256 256
$AMEM 411 CMBGXPROJ R*4 256
$AMEM 412 CMBGYPROJ R*4 256
$AMEM 421 CMTRXPROJ R*4 256
$AMEM 422 CMTRYPROJ R*4 256
$!------------ system CM --------------
$AMEM 431 KXYBG R*4 256 256
$AMEM 432 KXYPEAK R*4 256 256
$AMEM 433 KXYTRUE R*4 256 256
$AMEM 441 KXZBG R*4 256 256
$AMEM 442 KXZPEAK R*4 256 256
$AMEM 443 KXZTRUE R*4 256 256
$AMEM 451 KYZBG R*4 256 256
$AMEM 452 KYZPEAK R*4 256 256
$AMEM 453 KYZTRUE R*4 256 256
$AMEM 461 PHIBG R*4 256
$AMEM 462 PHIPEAK R*4 256
$AMEM 463 PHITRUE R*4 256
$AMEM 471 COSTBG R*4 256
$AMEM 472 COSTPEAK R*4 256
$AMEM 473 COSTTRUE R*4 256
$AMEM 481 FREBG R*4 256
$AMEM 482 FREPEAK R*4 256
$AMEM 483 FRETRUE R*4 256
$!-------------------ecr---------------------
```

```
$AMEM 501 ECRXYBG R*4 256 256
$AMEM 502 ECRXYPEAK R*4 256 256
$AMEM 503 ECRXYTRUE R*4 256 256
$!--------------- TAC -----------------------------------
$amem 50 TOFD1 8192 !  He-p1 - TAC
$amem 51 TOFD1G 8192 !  He-p1 - TAC
$amem 60 TOFD2 8192 !  He-p2 - TAC
$amem 70 TOFDD 8192 !  p1-p2 - TAC
$amem 71 TOFDDG 8192
$AMEM 80 TOFCM 8192 !  HE-CM - TAC
$AMEM 81 TOFCMG 8192
$!--------------- Raw Data -------------------------------
$AMEM 120 TDC1 16384
$AMEM 121 TDC2 16384
$AMEM 122 TDC3 16384
$AMEM 123 TDC4 16384
$AMEM 124 TDC5 16384
$AMEM 125 TDC6 16384
$AMEM 126 TDC12 16384
$AMEM 127 TDC22 16384
$AMEM 128 TDC13 16384
$AMEM 129 TDC23 16384
$AMEM 130 HIT1 17
$AMEM 131 HIT2 17
$AMEM 132 HIT3 17
$AMEM 133 HIT4 17
$AMEM 134 HIT5 17
$AMEM 135 HIT6 17
$amem 136 tdcraw 32
$amem 137 xcorr 256
$amem 138 ycorr 256
$clear flags
$gate new
$TDG ALLOC 2 ECRG SPEC 5
$TDG ALLOC 1 EBSG SPEC 18
$gate 16 3
$gate 17 3
$gate 80 3
$GATE 81 3
$GATE 34 1
$clear all
```

```
!  ********                                                  ***************
!  ***                              D2HE.EVL                              ***
!  ***       EVL FILE FOR ION-MOLECULAR ION COLLISION EXPERIMENTS         ***
!  ***             WITH BOTH BACKGAMMON AND DELAYLINE ANODE               ***
!  ***                            ingrid reiser                           ***
!  ***                     last modified 4.  Mai 2001                     ***
!  ***                                hbr                                 ***
!  ***                      last modified 2000-08-25                      ***
!  ***                                                                    ***
!  ***                                                                    ***
!  -------- PARAMETER SETTINGS ----------------------------------------
!OPTION KEEP
INTEGER BUFFOFF=3
INTEGER IND
!----------------- DELAY LINE CONSTANTS ----------
INTEGER IERR
INTEGER SUMCONST = 2000
INTEGER POSCONST = 100
INTEGER CENTER = 0
INTEGER MINSX = 2034
INTEGER MAXSX = 2044
INTEGER MINSY = 2034
INTEGER MAXSY = 2044
!******************** EFFICIENCY ****************
REAL LOSS = 0.75
REAL SCEFF = 1.0
INTEGER XHOLE = 10
INTEGER YHOLE = 6
INTEGER HOLEXW = 16
INTEGER HOLEYW = 16
!************* CORRECTION PARAMETERS *****************
real detan = 0
real TCAL = 1
real PSCAL = 1
real ytshift = 0 !shift per (t1-t2)[ns] (ch/ns)
real xtshift = 0 !  shift per (t1-t2)[ns] (ch/ns)
real scfactor = 1
real ytangle = 0
real cal = 0.5 !  shortens the time axis if no real calibration is
!used, set <0 if calibration routine is to be used
integer xcenter = 7
integer ycenter = -5
REAL CMANGLE = 1.22
!--------------- POSITION GATES ---------------
INTEGER EBS2D
INTEGER ECR2D
```

```
!  -------- FORTRAN ROUTINE VARIABLES
!******** rawdata *********
INTEGER X1
INTEGER X2
INTEGER Y1
INTEGER Y2
INTEGER ECRTOF
INTEGER PIGTOF
!******** hits *********
INTEGER CNT1
INTEGER CNT2
INTEGER CNT3
INTEGER CNT4
INTEGER CNT5
INTEGER CNT6
!************** sums **************
INTEGER SUMX1
INTEGER SUMX2
INTEGER SUMY1
INTEGER SUMY2
!**************** basic ***********
INTEGER X11
INTEGER X12
INTEGER Y11
INTEGER Y12
INTEGER X21
INTEGER X22
INTEGER Y21
INTEGER Y22
!*************** DLPOSITION **************
INTEGER POSX1
INTEGER POSY1
INTEGER POSX2
INTEGER POSY2
INTEGER XR1
INTEGER YR1
INTEGER XR2
INTEGER YR2
INTEGER TOF1
INTEGER TOF2
INTEGER TOF3
INTEGER TOF4
!******** ecrposition *********
INTEGER ECRX
INTEGER ECRY
```

```
INTEGER ECRR
INTEGER ECRNS
INTEGER ECRS
INTEGER ECRXP
INTEGER ECRYP
!************************ INTFRAME ***********
INTEGER XFR
INTEGER YFR
INTEGER TFR
INTEGER XFRMIR
INTEGER YFRMIR
INTEGER TFRMIR
INTEGER XCM
INTEGER YCM
INTEGER TCM
!****************** RHOPHI PLOTS ************
INTEGER XYRHO
INTEGER XYPHI
INTEGER XTRHO
INTEGER XTPHI
INTEGER YTRHO
INTEGER YTPHI
INTEGER XYRHOMIR
INTEGER XYPHIMIR
INTEGER XTRHOMIR
INTEGER XTPHIMIR
INTEGER YTRHOMIR
INTEGER YTPHIMIR
!****************** CMFRAME ***********************
INTEGER KX
INTEGER KY
INTEGER KZ
INTEGER KXMIR
INTEGER KYMIR
INTEGER KZMIR
INTEGER PHI
INTEGER PHIMIR
INTEGER COST
INTEGER COSTMIR
INTEGER FRE
!************************** RESORT ************
INTEGER COMPARE
INTEGER CHECK
INTEGER DEPTH = 5
!*********************** RAWDATA TEMP **********
```

```
INTEGER XR12
INTEGER XR13
INTEGER XR23
INTEGER XR22
!-------- SORTING ----------------------------
IMAGE ROUTINES ! Fortran unpacking and manipulation routines
OPTION ALLSPEC
OPTION TAPE
EVENT 2
!  TAPE
CALL CONVERT(IERR,BUFFOFF,$EVENT,$USERBUF,$TOUTPUT,COMPARE)
CALL RAWDATA($USERBUF,X1,X2,Y1,Y2,ECRTOF,PIGTOF,XR12,XR22,XR13,XR23)
CALL HITS(CNT1,CNT2,CNT3,CNT4,CNT5,CNT6)
CALL SUMS($USERBUF,SUMX1,SUMY1,SUMX2,SUMY2,SUMCONST)
CALL BASIC($USERBUF,X11,X12,Y11,Y12,X21,X22,Y21,Y22,CENTER)
!---------------- CREATE RAW DATA SPECTRA ------------------------
TINC X1 TDC1
TINC X2 TDC2
TINC Y1 TDC3
TINC Y2 TDC4
TINC ECRTOF TDC5
TINC PIGTOF TDC6
TINC XR12 TDC12
TINC XR22 TDC22
TINC XR13 TDC13
TINC XR23 TDC23
!
TINC CNT1 HIT1
TINC CNT2 HIT2
TINC CNT3 HIT3
TINC CNT4 HIT4
TINC CNT5 HIT5
TINC CNT6 HIT6
!  ----------------- RAW TDC ERROR COUNTER -------------
TINC COMPARE TDCRAW
!------------------ gates ----------------------------
gate peak 80 1
gate LBG 80 2
gate RBG 80 3
gate Gpeak 81 1
gate GLBG 81 2
gate GRBG 81 3
GATE YSLICE 34 1
!-------- CREATE INDIVIDUAL DELAY LINE SPECTRA --------
TINC X11 H1X1
```

```
TINC X12 H1X2
TINC Y11 H1Y1
TINC Y12 H1Y2
TINC X21 H2X1
TINC X22 H2X2
TINC Y21 H2Y1
TINC Y22 H2Y2
!---------- condition on timesum of first hit --------
TINC SUMX1 H1XSUM ! SUM SPECTRA
TINC SUMY1 H1YSUM
TINC SUMX2 H2XSUM
TINC SUMY2 H2YSUM
!
IF SUMX1 LE MINSX EXIT
IF SUMX1 GT MAXSX EXIT
IF SUMY1 LE MINSY EXIT
IF SUMY1 GT MAXSY EXIT
!
IF SUMX2 LE MINSX THEN
    CALL RESORT($USERBUF, MINSX, MAXSX, SUMCONST, CHECK, 1, DEPTH)
    IF CHECK LT 0 EXIT
    TINC CHECK XCORR
ENDIF
IF SUMX2 GT MAXSX THEN
    CALL RESORT($USERBUF, MINSX, MAXSX, SUMCONST, CHECK, 1, DEPTH)
    IF CHECK LT 0 EXIT
    TINC CHECK XCORR
ENDIF
IF SUMY2 LE MINSY THEN
    CALL RESORT($USERBUF, MINSY, MAXSY, SUMCONST, CHECK, 3, DEPTH)
    IF CHECK LT 0 EXIT
    TINC CHECK YCORR
ENDIF
IF SUMY2 GT MAXSY THEN
    CALL RESORT($USERBUF, MINSY, MAXSY, SUMCONST, CHECK, 3, DEPTH)
    IF CHECK LT 0 EXIT
    TINC CHECK YCORR
ENDIF
!-------- CALCULATION OF THE CM OF TWO FRAGMENTS------
CALL DIFF($USERBUF,TOF1,TOF2,TOF3,TOF4,CENTER)
CALL EFFICIENCY(LOSS, SCEFF,XHOLE,YHOLE,HOLEXW,HOLEYW)
CALL anacorr(YTshift,XTshift,ytangle,detan)
CALL ECRPOSITION($USERBUF,ECRX,ECRY,ECRR,ECRNS,ECRXP,ECRYP)
IF CAL LT 0 THEN
    CALL CALIBRATION(TCAL,PSCAL,SCFACTOR,XCENTER,YCENTER)
```

```
ENDIF
CALL DLPOSITION(POSX1,POSY1,POSX2,POSY2,POSCONST)
CALL INTFRAME(XFR,YFR,TFR,XFRMIR,YFRMIR,TFRMIR,XCM,YCM,TCM,
    POSCONST,cal)
CALL POLARCOORD(xyrho,xyphi,xyrhomir,xyphimir,xtrho,xtphi,
    xtrhomir,xtphimir, ytrho,ytphi,ytrhomir,ytphimir)
CALL CMFRAME(kx,ky,kz,kxmir,kymir,kzmir,phi,phimir,cost,
    costmir, cmangle,posconst,FRE)
!
!uncomment these to produce a short .evt file
!IF TOF4 GE 3100 EXIT
!IF TOF4 LT 1900 EXIT
!IF TOF3 GT 600 EXIT
!TAPE
!------- TAC INCREMENTS ----------------------------
TINC TOF1 TOFD1
TINC TOF2 TOFD2
TINC TOF3 TOFDD
TINC TOF4 TOFCM
!---------------- EBS POSITION SPECTRA --------------
TINC POSX1 H1XPOS sceff
TINC POSY1 H1YPOS sceff
TINC POSX2 H2XPOS sceff
TINC POSY2 H2YPOS SCEFF
TINC POSX1 POSY1 H1XYPOS
STA EBS2D
TINC POSX2 POSY2 H2XYPOS
TINC YFR FRY sceff
!
!  ------- ECR SPECTRA INCREMENTS ------------------
TINC ECRX ECRSX
TINC ECRY ECRSY
TINC ECRR ECRSR
TINC ECRNS ECRSUM
TINC ECRXP ECRYP ECRXY
STA ECR2D
IF ECR2D ECRG
    TAPE
    TINC TOF4 TOFCMG
ENDIF
!---------------- GATE CONDITIONS --------------------
IF TOF4 PEAK
    TINC ECRXP ECRYP ECRXYPEA
ENDIF
IF TOF4 LBG
```

```
    TINC ECRXP ECRYP ECRXYBG
ENDIF
IF TOF4 RBG
    TINC ECRXP ECRYP ECRXYBG
ENDIF
!-----------------------------------------------------
IF TOF4 GPEAK
    TINC XFR YFR FRXYPEAK sceff
    TINC XFRMIR YFRMIR FRXYPEAK sceff
    TINC XFR TFR FRXTPEAK sceff
    TINC XFRMIR TFRMIR FRXTPEAK sceff
    TINC YFR TFR FRYTPEAK sceff
    TINC YFRMIR TFRMIR FRYTPEAK sceff
!
    TINC KX KY KXYPEAK sceff
    TINC KXMIR KYMIR KXYPEAK sceff
    TINC KX KZ KXZPEAK sceff
    TINC KXMIR KZMIR KXZPEAK sceff
    TINC KY KZ KYZPEAK sceff
    TINC KYMIR KZMIR KYZPEAK sceff
!
    TINC PHI PHIPEAK sceff
    TINC PHIMIR PHIPEAK sceff
    TINC COST COSTPEAK sceff
    TINC COSTMIR COSTPEAK sceff
    TINC FRE FREPEAK sceff
!
    TINC POSX1 POSY1 H1XYPEAK SCEFF
    TINC POSX2 POSY2 H2XYPEAK SCEFF
    TINC XCM YCM CMXYPEAK sceff
    IF YFR YSLICE
        TINC XTPHI XTRHO XTRPPEAK sceff
        TINC XTPHIMIR XTRHOMIR XTRPPEAK sceff
        TINC XFR YFR XYSLPEAK
        TINC XFRMIR YFRMIR XYSLPEAK
        TINC XFR TFR XTSLPEAK
        TINC XFRMIR TFRMIR XTSLPEAK
        TINC YFR TFR YTSLPEAK
        TINC YFRMIR TFRMIR YTSLPEAK
    ENDIF
ENDIF
IF TOF4 GLBG
    TINC XFR YFR FRXYBG sceff
    TINC XFRMIR YFRMIR FRXYBG sceff
    TINC XFR TFR FRXTBG sceff
```

```
    TINC XFRMIR TFRMIR FRXTBG sceff
    TINC YFRMIR TFRMIR FRYTBG sceff
    TINC YFR TFR FRYTBG sceff
!
    TINC KX KY KXYBG sceff
    TINC KXMIR KYMIR KXYBG sceff
    TINC KX KZ KXZBG sceff
    TINC KXMIR KZMIR KXZBG sceff
    TINC KY KZ KYZBG sceff
    TINC KYMIR KZMIR KYZBG sceff
!
    TINC PHI PHIBG sceff
    TINC PHIMIR PHIBG sceff
    TINC COST COSTBG sceff
    TINC COSTMIR COSTBG sceff
    TINC FRE FREBG sceff
!
    TINC XCM YCM CMXYBG sceff
    TINC POSX1 POSY1 H1XYBG SCEFF
    TINC POSX2 POSY2 H2XYBG SCEFF
    IF YFR YSLICE
        TINC XTPHI XTRHO XTRPBG sceff
        TINC XFR YFR XYSLBG
        TINC XFRMIR YFRMIR XYSLBG
        TINC XFR TFR XTSLBG
        TINC XFRMIR TFRMIR XTSLBG
        TINC YFR TFR YTSLBG
        TINC YFRMIR TFRMIR YTSLBG
        TINC XTPHIMIR XTRHOMIR XTRPBG sceff
    ENDIF
ENDIF
IF TOF4 GRBG
    TINC XFR YFR FRXYBG sceff
    TINC XFRMIR YFRMIR FRXYBG sceff
    TINC XFR TFR FRXTBG sceff
    TINC XFRMIR TFRMIR FRXTBG sceff
    TINC YFR TFR FRYTBG sceff
    TINC YFRMIR TFRMIR FRYTBG sceff
!
    TINC KX KY KXYBG sceff
    TINC KXMIR KYMIR KXYBG sceff
    TINC KX KZ KXZBG sceff
    TINC KXMIR KZMIR KXZBG sceff
    TINC KY KZ KYZBG sceff
    TINC KYMIR KZMIR KYZBG sceff
```

```
!
    TINC PHI PHIBG sceff
    TINC PHIMIR PHIBG sceff
    TINC COST COSTBG sceff
    TINC COSTMIR COSTBG sceff
    TINC FRE FREBG sceff
!
    TINC XCM YCM CMXYBG sceff
    TINC POSX1 POSY1 H1XYBG SCEFF
    TINC POSX2 POSY2 H2XYBG SCEFF
    IF YFR YSLICE
        TINC XTPHI XTRHO XTRPBG sceff
        TINC XTPHIMIR XTRHOMIR XTRPBG sceff
        TINC XFR YFR XYSLBG
        TINC XFRMIR YFRMIR XYSLBG
        TINC XFR TFR XTSLBG
        TINC XFRMIR TFRMIR XTSLBG
        TINC YFR TFR YTSLBG
        TINC YFRMIR TFRMIR YTSLBG
    ENDIF
ENDIF
END
```

```
c     ROUTINES.FOR:
c     CONVERT()Unpacks data words from the LeCroy 3377 multi-hit TDC
c     Allows for an offset of initial ADC words in the event buffer
c     Kevin Carnes October, 1997, March 2000
c     Timur Osipov Dec 1999
c     ingrid reiser dec 2001
c     Must be compiled as a shareable library with the XSYS command
c     USHAREBLD.
      subroutine convert(ierr,buffoff,evbuf,userbuf,toutput,compare)
      integer compare
      external toutput
      character*80 message
      integer*2 evbuf(-1:*)   !event buffer sent from evl file
      integer*2 userbuf(-1:*) !temp buffer sent to evl file
      integer*2 ndword,idata,msb,lsb !need to be i*2 to
                avoid int.  overflow
c
      integer buffoff,ierr !number of ADC words to offset
      parameter (nchan = 5) !last channel number
      integer icnt(0:nchan) !multi-hit counters
      integer*2 tdcraw(0:nchan,0:8) !two-dimensional array to store up to
              !8 tdc hits for each channel
      common /usercom/ icnt,tdcraw
      nchoff = 4 !multi-hit channel offset for userbuf
      nmh = 5 !total number of double hit channels
      ierr=0
c
      do i=0,nchan
        icnt(i)=0
      end do
      do i=1,nchan+1+nmh
        userbuf(i)=0
      end do
      do i=0, 5
        do j=0,8
          tdcraw(i,j)=0
        end do
      end do
      userbuf(-1)=2*(nchan+nmh+1+2) !For troubleshooting, put #bytes here
      userbuf(0)=4095 !For troubleshooting, put Hex FFF here
      ndword=(evbuf(-1)/2)-3 !Total number of words -2 event
      !header words and 1 TDC header word
10    format(' i=',i2,' ierr=',i2,' ndword=',i2,' header=',z4,
     1' msb word=',z4,' lsb word=',z4)
```

```
      do j=1+buffoff,ndword+1
        if (bitest(evbuf(j),15)) then
c test to make sure this is header word
          ioff=j+1
          go to 20
        end if
      end do
20    continue
      do i=ndword,ioff,-2 !Count backwards, since multiple hits
              !are LIFO
        if (.not.(bitest(evbuf(i),8))) then
          ierr=1
          !write(message,10) i,ierr,ndword,evbuf(1),evbuf(i),evbuf(i+1)
          !call toutput(message)
          return
        end if
        ichan=iand(evbuf(i),"76000) !extract bits 10-14
        ichan=ishft(ichan,-10) !shift right 10 bits to give channel #
        msb=iand(evbuf(i),"377) !extract bits 0-7
        idata=ishft(msb,8) !shift msb left 8 bits
        ichan2=iand(evbuf(i+1),"76000)
        ichan2=ishft(ichan2,-10)
        if(ichan2.ne.ichan) then
          ierr=2
          write(message,10) i,ierr,ndword,evbuf(1),evbuf(i),evbuf(i+1)
          call toutput(message)
          return
        end if
        if(bitest(evbuf(i+1),8)) then
          ierr=3
          write(message,10) i,ierr,ndword,evbuf(1),evbuf(i),evbuf(i+1)
          call toutput(message)
          return
        end if
        lsb=iand(evbuf(i+1),"377) !extract bits 0-7
        idata=idata+lsb !add lsb and shifted msb
c
c ******** start filling userbuf and tdcraw ***********
c
        if (ichan .lt.  4) then !  Delay-line detector
          icnt(ichan)=icnt(ichan)+1
          tdcraw(ichan,icnt(ichan)) = idata
          if(icnt(ichan) .le.  2) then
            index=ichan+1+nchoff*(icnt(ichan)-1)
          userbuf(index)=idata
```

```
        end if
        else if (ichan .eq.  4) then !  ECR tof
          icnt(ichan)=icnt(ichan)+1
          tdcraw(ichan,icnt(ichan)) = idata
          if(icnt(ichan) .eq.  1) userbuf(9)=idata
          else if (ichan .eq.  5) then !  EBIS tof
            icnt(ichan)=icnt(ichan)+1
          tdcraw(ichan,icnt(ichan)) = idata
          if(icnt(ichan) .eq.  1) userbuf(10)=idata
          if(icnt(ichan) .eq.  2) userbuf(11)=idata
        end if
      end do
C
C ******** get ecr signals from eventbuffer **** ir 1/15/2001 *******
C
      do i=nchan+1+nmh+1, nchan+1+nmh+buffoff
        userbuf(i)=0
      end do
C
      do i=1, buffoff
        userbuf(nchan+1+nmh+i)=evbuf(i)
      end do
C
C ********************************************************************
C
      return
      end

      subroutine rawdata(userbuf,x1,x2,y1,y2,ecrt,pigt,x12,x22,x13,x23)
      implicit none
      integer*2 userbuf(-1:*)
      integer x1,x2,y1,y2,ecrt,pigt,x12,x13,x22,x23
      integer nchan
      parameter (nchan = 5) !last channel number
      integer icnt(0:nchan) !multi-hit counters
      integer*2 tdcraw(0:nchan,0:8) !two-dimensional array to store up to
c             !8 tdc hits for each channel
      common /usercom/ icnt,tdcraw
c
c     x1 = userbuf(1)
c     x2 = userbuf(2)
c     y1 = userbuf(3)
c     y2 = userbuf(4)
c     ecrt = userbuf(9)
c     pigt = userbuf(10)
```

```
      x1 = tdcraw(0,1)
      x2 = tdcraw(1,1)
      y1 = tdcraw(2,1)
      y2 = tdcraw(3,1)
      x12 = tdcraw(0,2)
      x13 = tdcraw(0,3)
      x22 = tdcraw(1,2)
      x23 = tdcraw(1,3)
      ecrt = tdcraw(4,1)
      pigt = tdcraw(5,1)
      end

      subroutine hits(cnt1,cnt2,cnt3,cnt4,cnt5,cnt6)
      implicit none
      integer cnt1,cnt2,cnt3,cnt4,cnt5,cnt6
      integer nchan
      parameter (nchan = 5) !last channel number
      integer icnt(0:nchan) !multi-hit counters
      integer*2 tdcraw(0:nchan,0:8) !two-dimensional array to store up to
              !8 tdc hits for each channel
      common /usercom/ icnt,tdcraw
c
      cnt1 = icnt(0)
      cnt2 = icnt(1)
      cnt3 = icnt(2)
      cnt4 = icnt(3)
      cnt5 = icnt(4)
      cnt6 = icnt(5)
      end

      subroutine resort(userbuf,min,max,sumconst, check,chan,depth)
      implicit none
      integer*2 userbuf(-1:*)
      integer min,max,sumconst,check,chan,depth,i,j
      integer*2 sum
      integer nchan
      parameter (nchan = 5) !last channel number
      integer icnt(0:nchan) !multi-hit counters
      integer*2 tdcraw(0:nchan,0:8) !two-dimensional array to store up to
          !8 tdc hits for each channel
      common /usercom/ icnt,tdcraw
c
      check = -1
      do i=2, depth
        do j=2,depth
```

```
          sum = tdcraw(5,2) - (tdcraw(chan-1,i) + tdcraw(chan,j))/2
     *      + sumconst
          if ((sum .ge.  min) .and.  (sum .le.  max)) then
            check = (i + 10 * j)
            userbuf(4+chan) = tdcraw(chan-1,i)
            userbuf(5+chan) = tdcraw(chan,j)
            return
          end if
        end do
      end do
      return
      end

      subroutine sums(userbuf,smr1x,smr1y,smr2x,smr2y,sumconst)
      implicit none
c
      integer*2 userbuf(-1:*)
      integer*2 smr1x,smr1y,smr2x,smr2y,sumconst
c
      smr1x=(2*userbuf(10)-userbuf(1)-userbuf(2))/2 + sumconst
      smr1y=(2*userbuf(10)-userbuf(3)-userbuf(4))/2 + sumconst
      smr2x=(2*userbuf(11)-userbuf(5)-userbuf(6))/2 + sumconst
      smr2y=(2*userbuf(11)-userbuf(7)-userbuf(8))/2 + sumconst
c
      return
      end

      subroutine basic(userbuf,x11,x12,y11,y12,x21,x22,y21,y22,tconst)
      implicit none
        integer*2 userbuf(-1:*)
        integer x11,x12,y11,y12,x21,x22,y21,y22,tconst
        x11 = userbuf(1) - userbuf(10) + tconst
        x12 = userbuf(2) - userbuf(10) + tconst
        y11 = userbuf(3) - userbuf(10) + tconst
        y12 = userbuf(4) - userbuf(10) + tconst
        x21 = userbuf(5) - userbuf(11) + tconst
        x22 = userbuf(6) - userbuf(11) + tconst
        y21 = userbuf(7) - userbuf(11) + tconst
        y22 = userbuf(8) - userbuf(11) + tconst
      return
      end

      subroutine diff(userbuf,tof1,tof2,tof3,tof4,center)
      implicit none
        integer*2 userbuf(-1:*)
```

```
        INTEGER tof1,tof2,tof3,tof4,center
        REAL x1raw,y1raw,x2raw,y2raw,t1raw,t2raw
        common /rawpositions/ x1raw,y1raw,x2raw,y2raw,t1raw,t2raw
c
        x1raw = userbuf(1)-userbuf(2)
        y1raw = userbuf(3)-userbuf(4)
        x2raw = userbuf(5)-userbuf(6)
        y2raw = userbuf(7)-userbuf(8)
        t1raw = userbuf(9)-userbuf(10)
        t2raw = userbuf(9)-userbuf(11)
        tof1 = t1raw + center
        tof2 = t2raw + center
        tof3 = userbuf(10)-userbuf(11)
        tof4 = (t1raw+t2raw)/2 + center
      return
      end

      subroutine anacorr(ytsh,xtsh,yta,a)
      implicit none
        real ytsh,xtsh,yta,a,y1rot,y2rot,yfr,yfrmir,tfr,tfrmir
        REAL x1raw,y1raw,x2raw,y2raw,t1raw,t2raw
        common /rawpositions/ x1raw,y1raw,x2raw,y2raw,t1raw,t2raw
c
c TEMPORARY ROTATION
        x1raw = cos(a)* x1raw - sin(a)* y1raw
        x2raw = cos(a)* x2raw - sin(a)* y2raw
        y1raw = cos(a)* y1raw + sin(a)* x1raw
        y2raw = cos(a)* y2raw + sin(a)* x2raw
c ANALYZER CORRECTION: 4=2*2 (0.5ns->ns, t1-t0=(t1-t2)/2 )
        x1raw = x1raw + xtsh*(t1raw - t2raw)/4
        x2raw = x2raw + xtsh*(t2raw - t1raw)/4
        y1raw = y1raw + ytsh*(t1raw - t2raw)/4
        y2raw = y2raw + ytsh*(t2raw - t1raw)/4
c z-axis correction
        y1rot = 0.89 * y1raw - 0.45 * x1raw
        y2rot = 0.89 * y2raw - 0.45 * x2raw
        tfr = (t1raw - t2raw)/2
        tfrmir = -(t1raw - t2raw)/2
        yfr = (y1rot - y2rot)/2
        yfrmir = -(y1rot - y2rot)/2
        tfr = tfr - tan(yta) * yfr
        tfrmir = tfrmir - tan(yta) * yfrmir
        t1raw = tfr
        t2raw = tfrmir
      return
```

```
      end

      subroutine dlposition(xr1,yr1,xr2,yr2,posconst)
      implicit none
        INTEGER xr1,yr1,xr2,yr2,posconst
        REAL x1raw,y1raw,x2raw,y2raw,t1raw,t2raw
        common /rawpositions/ x1raw,y1raw,x2raw,y2raw,t1raw,t2raw
c
        xr1 = x1raw + posconst
        yr1 = y1raw + posconst
        xr2 = x2raw + posconst
        yr2 = y2raw + posconst
      return
      end

      subroutine efficiency(loss, eff, xcenter, ycenter, xwidth, ywidth)
        REAL loss, eff, temp
        INTEGER xcenter, ycenter, xwidth, ywidth
        REAL x1raw,y1raw,x2raw,y2raw,t1raw,t2raw
        common /rawpositions/ x1raw,y1raw,x2raw,y2raw,t1raw,t2raw
c
        temp = 1 - loss * exp(-2*(x1raw - xcenter)*(x1raw - xcenter)/
     *  (xwidth*xwidth))
     *  * exp(-2*(y1raw - ycenter)*(y1raw - ycenter)/
     *  (ywidth*ywidth))
        eff = 1 / temp
      return
      end

      subroutine ecrposition(userbuf,ecrx,ecry,ecrr,ecrns,ecrxp,ecryp)
      implicit none
        integer*2 userbuf(-1:*)
        integer ecrx,ecry,ecrr,ecrs,ecrns,ecrxp,ecryp
        real rfactor
        integer chan
        rfactor = 1.5
        chan = 256
        ecrx = userbuf(12)
        ecry = userbuf(13)
        ecrr = userbuf(14)
        ecrns = (ecrx + ecry + ecrr)/3
        ecrs = ecrr * rfactor + ecrx + ecry
        if (ecrs .gt.  0.0) then
          ecrxp = ecrx * chan / ecrs + 0.5
          ecryp = ecry * chan / ecrs + 0.5
```

```
        endif
      return
      end

      subroutine calibration(tcal,pscal,scfactor,xcenter,ycenter)
      implicit none
        real tcal,pscal,scfactor
        INTEGER xcenter,ycenter
        real x1temp,y1temp,x2temp,y2temp
        real x0,x1,x2,x3,x4,x5,x6,x7,x8,x9
        real y0,y1,y2,y3,y4,y5,y6,y7,y8,y9
        REAL x1raw,y1raw,x2raw,y2raw,t1raw,t2raw
        common /rawpositions/ x1raw,y1raw,x2raw,y2raw,t1raw,t2raw
c
        x0 = 2.707
        x1 = 0.836
        x2 = -8.47E-4
        x3 = -5.83E-5
        x4 = 0.565
        x5 = -1.4E-4
        x6 = -2.33E-5
        x7 = -5.04E-3
        x8 = -9.13E-5
        x9 = -7.71E-5
        y0 = -3.7
        y1 = 0.379
        y2 = 9.43E-4
        y3 = 3.39E-6
        y4 = -0.892
        y5 = -1.53E-3
        y6 = -1.47E-5
        y7 = 2.2E-3
        y8 = -4.91E-5
        y9 = 9.15E-5
        x1raw = x1raw - xcenter
        y1raw = y1raw - ycenter
        x2raw = x2raw - xcenter
        y2raw = y2raw - ycenter
c ************ position adjustment ******************************
        x1temp = x0 + x1 * x1raw + x2 * x1raw*x1raw
     *    + x3 * x1raw*x1raw*x1raw + x4 * y1raw
     *    + x5 * y1raw*y1raw + x6 * y1raw*y1raw*y1raw
     *    + x7 * x1raw*y1raw + x8 * x1raw*x1raw*y1raw
     *    + x9 * x1raw*y1raw*y1raw
        y1temp = y0 + y1 * x1raw + y2 * x1raw*x1raw
```

```
     *    + y3 * x1raw*x1raw*x1raw + y4 * y1raw
     *    + y5 * y1raw*y1raw + y6 * y1raw*y1raw*y1raw
     *    + y7 * x1raw*y1raw + y8 * x1raw*x1raw*y1raw
     *    + y9 * x1raw*y1raw*y1raw
        x2temp = x0 + x1 * x2raw + x2 * x2raw*x2raw
     *    + x3 * x2raw*x2raw*x2raw + x4 * y2raw
     *    + x5 * y2raw*y2raw + x6 * y2raw*y2raw*y2raw
     *    + x7 * x2raw*y2raw + x8 * x2raw*x2raw*y2raw
     *    + x9 * x2raw*y2raw*y2raw
        y2temp = y0 + y1 * x2raw + y2 * x2raw*x2raw
     *    + y3 * x2raw*x2raw*x2raw + y4 * y2raw
     *    + y5 * y2raw*y2raw + y6 * y2raw*y2raw*y2raw
     *    + y7 * x2raw*y2raw + y8 * x2raw*x2raw*y2raw
     *    + y9 * x2raw*y2raw*y2raw
c ************** end position adjustment *********************
c ****************** momentum calibration ******************
        t1raw = t1raw * tcal/2
        t2raw = t2raw * tcal/2
c additional factor of 2 because TDC gives 0.5ns/ch
        x1raw = -x1temp * pscal/scfactor
c minus because of sign mistake in the map voltages
        y1raw = y1temp * pscal*scfactor
        x2raw = -x2temp * pscal/scfactor
        y2raw = y2temp * pscal*scfactor
c ********************************************************
      return
      end


      subroutine intframe(ixfr,iyfr,itfr,ixfrmir,iyfrmir,itfrmir,
     *    ixcm,iycm,itcm,posconst,cal)
      implicit none
        integer ixfr,iyfr,ixfrmir,iyfrmir,itfr,itfrmir,
     *    ixcm,iycm,itcm,posconst
        real*4 cal,xfr, yfr, tfr, xfrmir, yfrmir, tfrmir
        REAL x1raw,y1raw,x2raw,y2raw,t1raw,t2raw
        common /rawpositions/ x1raw,y1raw,x2raw,y2raw,t1raw,t2raw
        common /fragments/ xfr,yfr,tfr,xfrmir,yfrmir,tfrmir
c
c*****************************************************************
c******* next two lines compress time axis ******
c******* if subroutine calibration is not used ******
c*****************************************************************
        if (cal .gt.  0) then
          t1raw = t1raw * cal
```

```
          t2raw = t2raw * cal
        endif
c*********************************************************************
        xfr = (x1raw - x2raw)/2
        yfr = (y1raw - y2raw)/2
        tfr = t1raw
        xfrmir = -(x1raw - x2raw)/2
        yfrmir = -(y1raw - y2raw)/2
        tfrmir = t2raw
c*********************************
        ixfr = xfr + posconst
        iyfr = yfr + posconst
        itfr = tfr + posconst
        ixfrmir = xfrmir + posconst
        iyfrmir = yfrmir + posconst
        itfrmir = tfrmir + posconst
        ixcm = (x1raw + x2raw)/2 + posconst
        iycm = (y1raw + y2raw)/2 + posconst
        itcm = (t1raw + t2raw)/2 -2100
      return
      end

      subroutine polarcoord(xyr,xyp,xyrm,xypm,xtr,xtp,xtrm,xtpm,
     *    ytr,ytp,ytrm,ytpm)
      implicit none
        integer xyr,xyp,xyrm,xypm,xtr,xtp,xtrm,xtpm
        integer ytr,ytp,ytrm,ytpm
        real*4 xfr, yfr, tfr, xfrmir, yfrmir, tfrmir
        common /fragments/ xfr,yfr,tfr,xfrmir,yfrmir,tfrmir
c
        xyr = sqrt(xfr*xfr + yfr*yfr)
        if (xfr .ne.  0 .and.  yfr .ne.  0) then
          xyp = ( ATAN2D(yfr,xfr) + 180 ) / 2
        else
          xyp = -1
        endif
        xyrm = sqrt(xfrmir*xfrmir + yfrmir*yfrmir)
        if (xfrmir .ne.  0 .and.  yfrmir .ne.  0) then
          xypm = ( ATAN2D(yfrmir,xfrmir) + 180 ) / 2
        else
          xypm = -1
        endif
c
        xtr = sqrt(xfr*xfr + tfr*tfr)
        if (xfr .ne.  0 .and.  tfr .ne.  0) then
```

```
          xtp = ( ATAN2D(tfr,xfr) + 180 ) / 2
        else
          xtp = -1
        endif
        xtrm = sqrt(xfrmir*xfrmir + tfrmir*tfrmir)
        if (xfrmir .ne.  0 .and.  tfrmir .ne.  0) then
          xtpm = ( ATAN2D(tfrmir,xfrmir) + 180 ) / 2
        else
          xtpm = -1
        endif
c
        ytr = sqrt(yfr*yfr + tfr*tfr)
        if (yfr .ne.  0 .and.  tfr .ne.  0) then
          ytp = ( ATAN2D(tfr,yfr) + 180 ) / 2
        else
          ytp = -1
        endif
        ytrm = sqrt(yfrmir*yfrmir + tfrmir*tfrmir)
        if (yfrmir .ne.  0 .and.  tfrmir .ne.  0) then
          ytpm = ( ATAN2D(tfrmir,yfrmir) + 180 ) / 2
        else
          ytpm = -1
        endif
c
      return
      end

      subroutine cmframe(kx,ky,kz,kxmir,kymir,kzmir,phi,phimir,
     *  cost,costmir,angle,posconst,fre)
      implicit none
        real rkx,rky,rkz,rkxmir,rkymir,rkzmir
        integer kx,ky,kz,kxmir,kymir,kzmir,posconst,fre
        integer phi,phimir,cost,costmir
        real angle
        real rkr,rkrmir
        real*4 xfr, yfr, tfr, xfrmir, yfrmir, tfrmir
        common /fragments/ xfr,yfr,tfr,xfrmir,yfrmir,tfrmir
c
        rkx = xfr * cos(angle) - tfr * sin(angle)
        rky = yfr
        rkz = tfr * cos(angle) + xfr * sin(angle)
        rkxmir = xfrmir * cos(angle) - tfrmir * sin(angle)
        rkymir = yfrmir
        rkzmir = tfrmir * cos(angle) + xfrmir * sin(angle)
        rkr = sqrt( rkx*rkx + rky*rky + rkz*rkz )
```

```
  rkrmir = sqrt(rkxmir*rkxmir + rkymir*rkymir + rkzmir*rkzmir)
  if (rkr .ne.  0 ) then
    cost = (( rkz / rkr ) + 1 ) * 100
  else
    cost = -1
  end if
  if (rkrmir .ne.  0 ) then
    costmir = (( rkzmir / rkrmir )+1 )*100
  else
    costmir = -1
  end if
  if (rky .ne.  0 .and.  rkx .ne.  0) then
    phi = (atan2d(rky,rkx) + 180)/2
  else
    phi = -1
  end if
  if (rkymir .ne.  0 .and.  rkxmir .ne.  0) then
    phimir = (atan2d(rkymir,rkxmir) + 180)/2
  else
    phimir = -1
  end if
  kx = rkx + posconst
  ky = rky + posconst
  kz = rkz + posconst
  kxmir = rkxmir + posconst
  kymir = rkymir + posconst
  kzmir = rkzmir + posconst
  if (rkr .lt.  200) then
    fre = (rkr * rkr) * 0.0037
  end if
  if (rkr .ge.  200) fre = 225
return
end
```